Impact of agrivoltaics on ground convective heat exchange: a preliminary comparison between CFD simulations and wind tunnel experimental results

Supervisor

Prof. Andrea Carpignano

Candidate

Gabriele Tobia

Co-supervisor

Prof.ssa Raffaella Gerboni

Prof. Pietro Stefano Salizzoni

Master's Degree Programme
Energy and Nuclear Engineering – Renewable Energy Systems

Academic Year 2025/2026

...

ABSTRACT

Agrivoltaics is a technology that combines the production of photovoltaic energy with the underlying and surrounding agricultural production, maximizing the Land Equivalent Ratio (LER), that is the land-use efficiency. Its integration in the European landscape, with a growing scarcity of available land, is fundamental to mitigate the conflict between the agri-food sector and the energy sector. This work aims to study the convective heat transfer between the ground and the panels of an agrivoltaic system, which involves the fluid comprised between the two. In agrivoltaic systems the convective heat transfer represents a key phenomenon, as it influences the fundamental microclimatic parameters of the system: the air temperature directly affects the conversion efficiency of the photovoltaic panels, which deteriorates with the increase in the temperature of the panels, and the evapotranspiration, which is the phenomenon that regulates the exchange of water vapor between the atmosphere and the underlying plants and ground. Evapotranspiration phenomenon is proportionally linked to the heat transfer coefficient through the Chilton-Colburn analogy, and is crucial in quantifying soil moisture and estimating the consequent water saving derived from the reduction of irrigation. In the work, the convective heat transfer of an agrivoltaic system exposed to a wind coming from the North, that is behind the panels, is studied, analysing three different configurations in which the tilt angle is kept constant at 20°, but varying the distance between the rows and the ground clearance (the height of the lower edge of the tilted panel relative to the ground). The forced convection analysis was conducted with a dual approach: experimentally, with tests in a wind tunnel on a heated plate, with miniature panels on top hit by an air flow of 5 meters per second, and numerically through CFD simulations in 1:75 scale relative to the experimental tests, simplified in a 2D domain to isolate the effect of the modules and avoid the fluid-dynamic interferences of the support structures, which would otherwise act as barriers to the air passage, which has the same inlet velocity as the experiments. The results examine the trend of the normalized convective heat transfer coefficient respect to a reference case (free plate without panels), to quantify the impact of the panels' presence and

geometry. The values are studied along the x coordinate normalized relative to the minimum row spacing, allowing a direct reading of the panels' position along the domain. The comparison highlights a discrepancy between CFD results and experimental ones: the numerical simulations tend to underestimate the heat transfer and the turbulence generated under the modules, and furthermore, while the experimental data reach a constant value along x, in the CFD case with an increased height of the modules, the domain is not extended enough to reach convergence. Such divergences are studied taking into analysis the values of longitudinal velocity, turbulent kinetic energy and vorticity. By studying these parameters, it emerges that the increase in height reduces the heat transfer, favouring the presence of moisture at the ground and limiting evapotranspiration, while the increase in the distance between the rows intensifies the convective heat transfer, increasing the cooling of the ground and of the modules. It concludes highlighting the utility of CFD simulations to validate the experimental data, putting in evidence the intrinsic limits linked to the 2D simplification.

SUMMARY

Figures List

Tables List

Acronyms List

- ***APV / AV**: Agrivoltaic Systems*
- ***AY**: Agricultural Yield*
- ***CAPEX**: Capital Expenditures*
- ***CFD**: Computational Fluid Dynamics*
- ***DNS**: Direct Numerical Simulation*
- ***EU**: European Union*
- ***GCR**: Ground Coverage Ratio*
- ***GHI**: Global Horizontal Irradiance*
- ***GMPV**: Ground-Mounted PV*
- ***LAOR**: Maximum surface covered by photovoltaic modules (Italian MASE Guidelines)*
- ***LDA**: Laser Doppler Anemometry*
- ***LER**: Land Equivalent Ratio*
- ***LMFA**: Laboratoire de Mécanique des Fluides et d'Acoustique*
- ***MASE**: Ministero dell'Ambiente e della Sicurezza Energetica*

- ***OPV**: Organic Photovoltaic*
- ***P/E (index)**: Precipitation and Evaporation index*
- ***PAR**: Photosynthetically Active Radiation*
- ***PIV**: Particle Image Velocimetry*
- ***PNRR**: Piano Nazionale di Ripresa e Resilienza*
- ***PV**: Photovoltaic*
- ***RANS**: Reynolds-Averaged Navier-Stokes*
- ***SST**: Shear Stress Transport (Turbulence model)*
- ***UAA**: Utilized Agricultural Area*
- ***WUE**: Water Use Efficiency*

Dimensionless Numbers:

- ***Gr**: Grashof Number*
- ***M**: Mach Number*
- ***Nu**: Nusselt Number*
- ***Pr**: Prandtl Number*
- ***Ra**: Rayleigh Number*
- ***Re**: Reynolds Number*
- ***Sc**: Schmidt Number*
- ***Sh**: Sherwood Number*

Roman Symbols:

- *a: Speed of sound*
- c_p*: Specific heat at constant pressure*
- $C_{f,x}$*: Local friction coefficient*
- *: Mass diffusion coefficient*
- *d: Ground clearance*
- h_m*: Mass transfer coefficient*
- h_t*: Convective heat transfer coefficient*
- *k: Turbulent kinetic energy*
- *l: Row spacing*
- *L: Characteristic length*
- *p: Pressure*
- *P: Electrical power*
- *q: Dynamic pressure*
- *R: Electrical resistance*
- *S: Strain rate tensor*
- *T: Temperature*
- *u, v: Velocity components in the longitudinal and vertical directions*
- u^**: Friction velocity*

- *V: Applied voltage*
- *x, y: Spatial coordinates*

Greek Symbols:

- α*: Angle between the inclined solar panel and the direction of the airflow (Tilt angle)*
- β*: Thermal expansion coefficient*
- ε*: Rate of dissipation of the turbulence kinetic energy*
- λ*: Thermal conductivity of the fluid*
- μ*: Dynamic viscosity*
- ν*: Kinematic viscosity*
- ρ*: Fluid density*
- σ*: Standard deviation*
- ϖ*: Turbulence frequency / specific dissipation rate*
- ϖ_z*: Vorticity*

INTRODUCTION

Greenhouse gas emissions

Climate change represents one of the most critical challenges of the XXI century, environmentally impacting and increasingly severe and widespread, as the escalation of extreme weather events across Europe, the accelerating sea-level rise, and the uncontrolled melting rates of polar ice caps and glaciers are profoundly compromising global ecosystems and threatening the stability of human lives. The international response to these events consists in the mitigation of greenhouse gas emissions and in reversing the trend of increasing global average temperature. Starting from the latter, as mandated by the Paris Agreement (2015), the objective is to keep the increase below 2°C compared to the pre-industrial period, aiming for 1.5°C. On the other hand, emission limits are set based on the 1990 emission levels, when the first IPCC Assessment Report was published, providing the first scientific evidence linking anthropogenic activities to global warming and drawing the attention of international politics, which moved first with the Kyoto Protocol, encouraging emission reductions in industrialized countries, up to the creation of the European Green Deal, to legally impose climate neutrality on European countries by 2050. Globally, the sector with the highest environmental impact is electricity and heat production (Figure 1), responsible for over 15 billion tonnes of CO_2 equivalent $[tCO_2e]$ and, along with the transport sector, it represents the area most dependent on fossil fuels and, consequently, the primary focus for the energy transition. Furthermore, the nations with the highest emission impact (Figure 2) are China and India, where electricity production is still predominantly dependent on coal, and the United States, which has the highest per capita emission rate in the world. The situation in the European Union is more virtuous, although its energy scenario remains internally fragmented, as resource dependency varies significantly among member states, such as Italy which relies heavily on natural gas, while others are accelerating the decarbonization of their electricity mix through different pathways, such as Spain, which

is heavily focused on the growth of renewable energy, and France, which bases its electricity production mainly on nuclear plants.

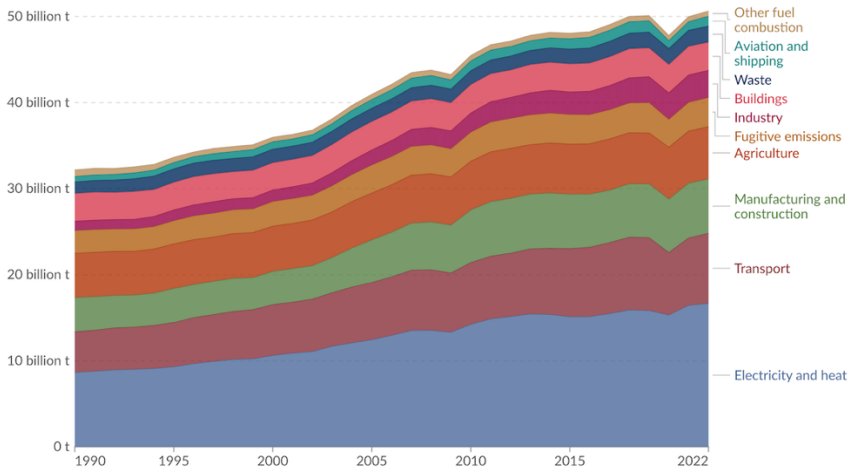

Figure 1: Global greenhouse gas emissions by sector from 1990 to 2022 [tCO_2e] [1]

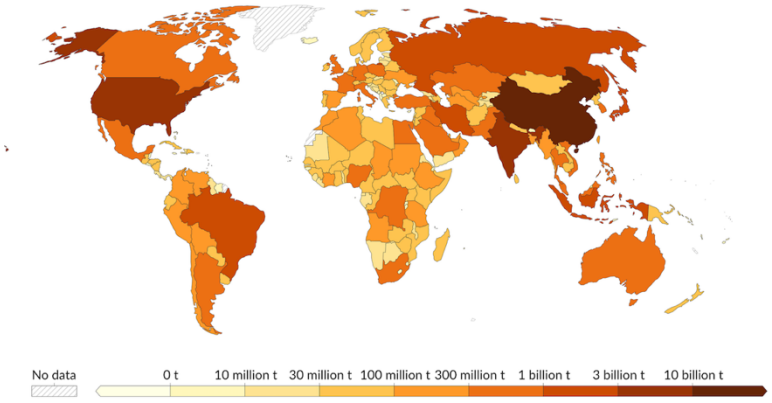

Figure 2: Global CO_2 emissions by country in 2024 [tCO_2e] [2]

Renewables, Solar PV technology and agrivoltaics

To reduce the environmental impact of the electricity and heat sector, the most effective solution lies in renewable energy systems, which are characterized by low emission intensities throughout their lifecycle. In fact, their carbon footprint is concentrated in the construction and decommissioning phases, as they generate zero

operational emissions, thus representing the primary pathway toward the deep decarbonization of these sectors. Specifically, regarding electricity generation, a consistent global trend has emerged over the last two decades, where regardless of national political orientations, there has been a significant increase in the adoption of green technologies and, as result, renewables currently account for approximately 31.8% of the total global electricity generation share (Figure 3).

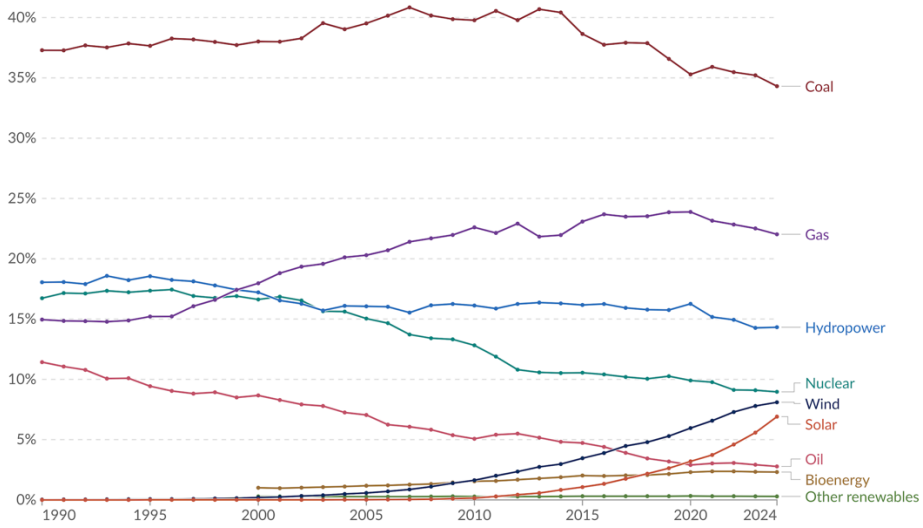

Figure 3: Global evolution of share of electricity production by source (1990-2024)[3]

A striking example is China, which over the past twenty years has dramatically expanded both its renewable energy capacity and actual electricity generation from renewable sources to meet its growing electricity demand, with major investments in hydroelectric, wind, and solar power (Figure 4). Similarly, in the United States, despite a conservative shift that seemed to endanger the continuity of green policies, investments in renewable energy, particularly in solar power, have continued to rise and, in fact, ongoing projects are expected to increase the USA's total photovoltaic capacity by approximately 3% by 2030 [6][10]. This trend is clearly reflected in the evolution of the U.S. energy mix and the steady growth of renewable electricity generation (Figure 5), highlighting that the motivation behind such developments is not solely the pursuit of climate objectives, but also the economic advantages and profitability associated with the energy market. Furthermore, focusing on the European Union, there is a significant expansion of the

renewable energy share in electricity generation and the phased replacement of fossil fuels with sustainable alternatives, such as wind, solar, and advanced biofuels. In fact, Europe has experienced a steady increase in renewable electricity production since 2000 (Figure 6), with solar photovoltaic technology showing a particularly accelerated growth rate in the last decade, transitioning from a niche technology to a central component of the European energy mix.

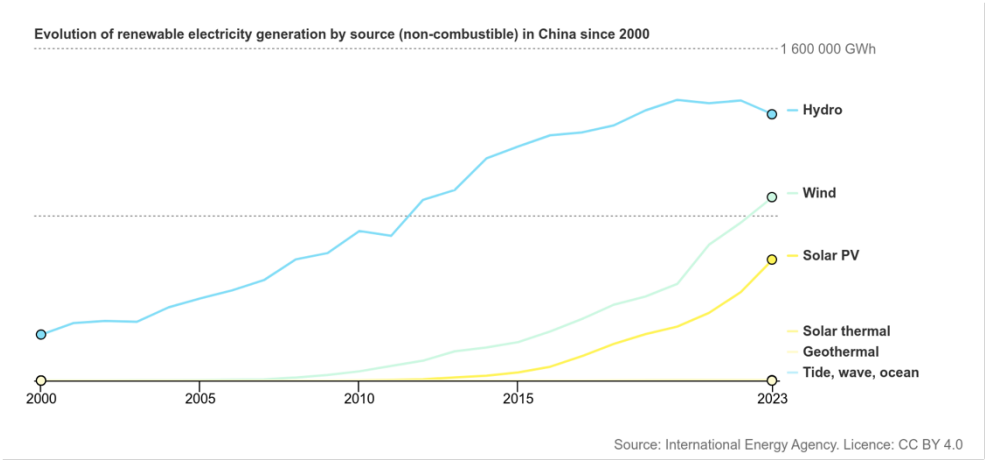

Figure 4: renewable energies share in China over the last years [4]

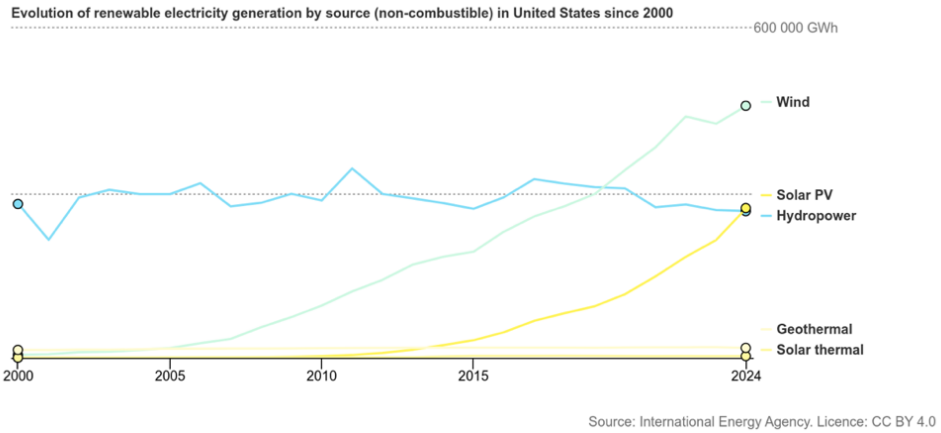

Figure 5: renewable energies share in USA over the last years [11]

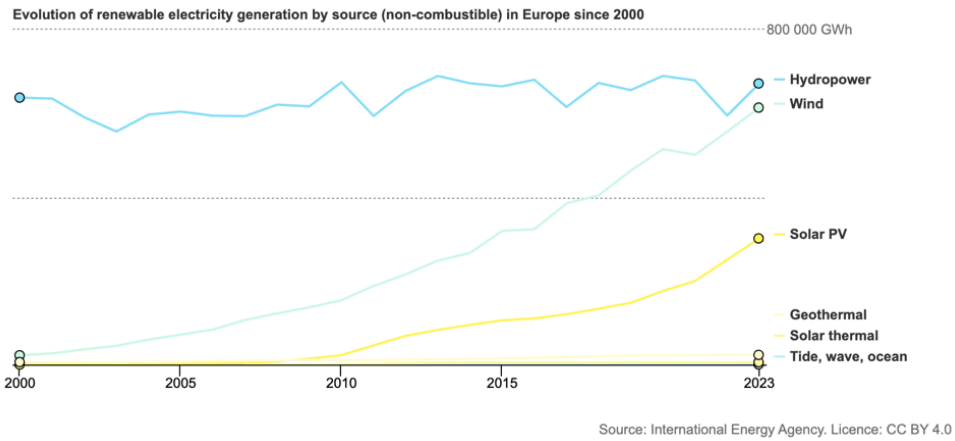

Figure 6: share of renewables in UE over the last years [5]

Among renewable energy sources, solar photovoltaic technology stands out for its rapid spread over the last years and, in fact, according to the International Energy Agency [12], solar power is projected to become the world's largest renewable energy source by 2029. This growth is driven by its remarkable versatility and continuous innovation in both the materials employed to fabricate solar photovoltaic cells and the design of systems layouts and compositions, encompassing a broad spectrum of configurations that comprehend conventional rooftop systems, mostly installed in domestic contexts, emerging floating installations on water surfaces and utility-scale ground mounted systems, which are highly employed in industrial contexts for large amount of energy production (Figure 7).

Figure 7: A 42 MW_p utility-scale ground mounted PV system located near Udine, Italy [9]

The rapid expansion of ground-mounted PV systems, along with other renewables characterized by low power density and that require large amount of land for their systems, such as wind farms or energy crops for biomass, has introduced a critical challenge: the competition for land use between the energy market and the agricultural industry. This conflict arises because these renewable installations require vast land areas, leading to the displacement of agricultural activities and food production. A strategy to solve this conflict involves integrated and synergic solutions that combine photovoltaic infrastructure for electricity generation with agricultural production and green spaces within the same area: the *agrivoltaics*, which has seen a rapid expansion in recent years as shown in the following figure (Figure 8).

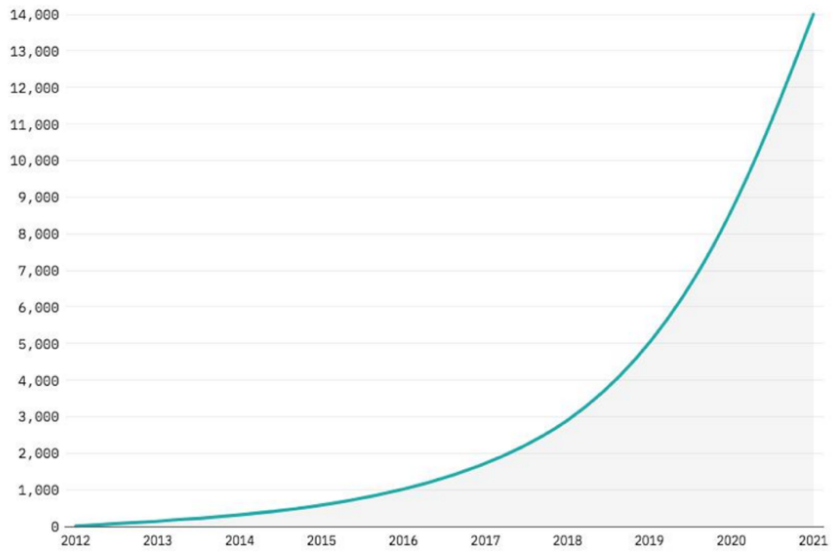

Figure 8: agrivoltaic capacity [MW] installed worldwide during the period 2012-2021 [12]

This expansion of agrivoltaic installations is paralleled by a consolidated international interest in the technology. The most known global event in this sector is the *Agrivoltaics World Conference*, an annual meeting established in 2020, which serves as a global platform for showcasing the scientific advancements and developments in the field of agrivoltaics [13]. The primary advantage of agrivoltaic systems is the simultaneous use of land for both energy and food production, which significantly increases the land equivalent ratio (*LER*, the parameter to represent the land use efficiency) as the same portion of field can be shared between two activities (electricity production and

agriculture production) instead of just one, thereby mitigating the conflict over land. From a technical perspective, agrivoltaics can provide specific agronomic services, such as protecting crops from extreme weather, providing animal welfare through shade and enhancing Water Use Efficiency (*WUE*) by reducing evapotranspiration and, furthermore, these systems can promote biodiversity by creating protected habitats between or around solar panels. However, there are some weak points like a higher CAPEX compared to other renewables, that in Germany was studied to be at least 20% higher compared to traditional ground-mounted PV systems. In fact, while the costs of the electrical system components remain virtually unchanged, there is a difference in the costs that lies on the mounting structure and the site preparation (Figure 9). Furthermore, there is a lack of a harmonized EU definition and dedicated standards, which can lead to legal insecurity regarding land characterization. [7][8]

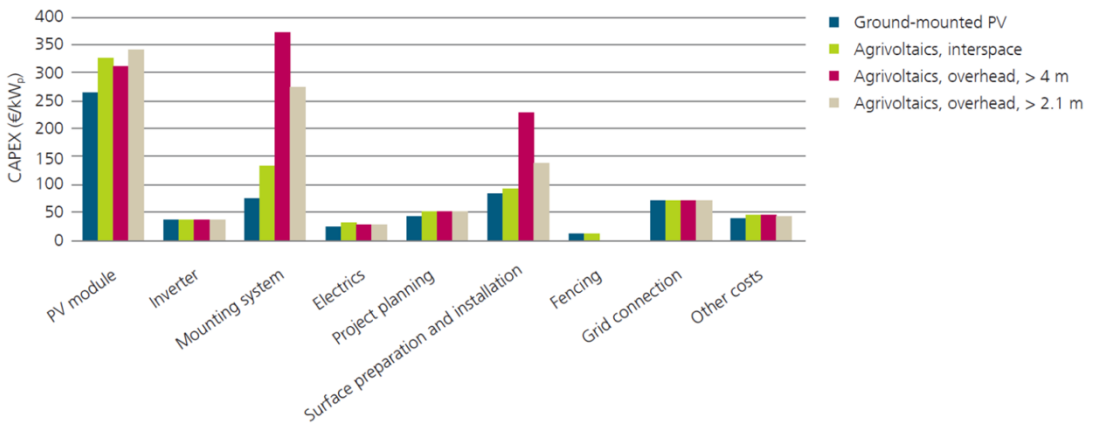

Figure 9: Comparison of estimated Capital Expenditures (CAPEX) for standard ground-mounted PV (GMPV) and three different agrivoltaic configurations: interspace, overhead (> 2.1 m), and high-clearance overhead (> 4 m) [7]

Thesis objective

The objective of this thesis is to investigate the convective heat transfer between the ground and the panels of an agrivoltaic system through a comparative analysis of experimental and numerical data. The study aims to evaluate how different geometrical configurations, specifically varying ground clearance and row spacing, influence the convective heat transfer coefficient, a key parameter for determining both photovoltaic

efficiency and soil evapotranspiration. The research is conducted using a dual approach, using experimental data from wind tunnel tests of the LMFA (*Laboratoire de Mécanique des Fluides et d'Acoustique*) of the École Centrale de Lyon on a 1:75 scale model, and numerical data from 2D CFD simulations, provided by of the École Centrale de Lyon, extracted using the software ANSYS Fluent. By analysing longitudinal velocity profiles and turbulent kinetic energy, the work specifically seeks to identify and quantify the discrepancies between the numerical results and the experimental ones.

Thesis structure

This thesis is structured into several sections, it begins with an overview of the history and current state of the art of agrivoltaic technology, examining various system configurations and the fundamental microclimatic parameters, such as the Land Equivalent Ratio (LER) and Water Use Efficiency (WUE), that define the efficiency of dual land use. This leads into a dedicated analysis of the physical interaction between wind and the agrivoltaic array, establishing the theoretical basis for how forced convection influences the thermal exchange between the PV modules and the ground. After that there is the explanation of the methodology adopted for the analysis of the datasets provided by the École Centrale de Lyon, describing the experimental setup at the LMFA wind tunnel and the characteristics of the 2D CFD numerical simulations, from which the relevant data were extracted using ANSYS Fluent software. The core of the work is the analysis highlighting the discrepancies between the numerical simulations and the experimental data regarding the convective heat transfer coefficient, supported by a study of longitudinal velocity profiles and turbulent kinetic energy to identify the fluid dynamic causes of the observed numerical underestimations. Finally, the work concludes with a summary of the findings, evaluating the reliability of simplified 2D modelling and suggesting future improvements.

1 Agrivoltaics and microclimate

The definition of agrivoltaic system varies among nations and organizations. According to the Fraunhofer Institute in Germany the agrivoltaics is a technology that allows land to be used simultaneously for farming and generating electricity with photovoltaics, integrating land for crop farming with ground mounted PV systems, and can also be extended to livestock combined with solar electricity production. In this first chapter the state of art of the technologies, along with a historical explanation, will be analysed. It will also be observed the legislation level among EU countries, explaining the different types of configurations and technology existing.

1.1 Agrivoltaics technology state of art

Agrivoltaics traces its scientific roots back to 1981, when Fraunhofer ISE researchers, Adolf Goetzberger and Armin Zastrow, proposed in their article "*Kartoffeln unter dem Kollektor"* the concept in Germany of installing raised solar panels for the dual function of energy and agriculture. Practical development was later led by Japan, where in 2004 engineer Akira Nagashima promoted the concept of "solar sharing" to optimize sunlight between crops and PV modules: [14]

"Solar Sharing refers to sharing the surplus solar power, which is not contributing to crop production, between agriculture and power generation. It secures the sunlight needed for crop production and maintains farming"[1].

Today, the agrivoltaics sector is rapidly expanding worldwide. China holds the leadership in terms of installed capacity, which is estimated at $12\ GW_p$ in 2021, and hosts the world's largest plant in the Gobi Desert, with a capacity of $700\ MW_p$. In the United States, total solar capacity is expected to reach around $300\ GW_p$ by 2030, with approximately $200\ GW_p$ projected to come from agrivoltaic systems, according to

[1] Akira Nagashima, *Solar Sharing: Changing the World and Life* (2015)

Department of Energy (*DOE*) projections. In Europe, the strategy to decarbonize and meet the Green Deal objectives also relies on agrivoltaics, which is included within the EU Solar Energy Strategy, a program that aims to instal 730 GW of solar photovoltaic energy by 2030. The potential of agrivoltaics in Europe is high, with the Joint Research Centre of the European Commission which has estimated that by covering only 1% of the Utilised Agricultural Area (UAA) with agrivoltaic systems, a capacity of approximately 944 GW could be generated (as shown in Table 1) and, in fact, the technology attracts investments, such as the European research program Horizon Europe, which has allocated about ten million euros to fund dedicated projects. This interest is reflected in the strategies of individual member states, which in recent years have accelerated investments. France, where the term agrivoltaic (*agrivoltaïsme*) was created in 2011 by the engineer Dupraz, has hosted utility-scale plants since that same year and since 2017 has had a dedicated government funding program only for agrivoltaics, in addition to being the site of European projects such as the Agrivoltaic Canopy Project, characterized by 5-meter-high structures with dynamic modules designed to protect crops and study the reduction of thermal and water stress, aiming to avoid 6,982 tonnes of CO_2 equivalent of greenhouse gas emissions during the first ten years of operation by the renewable electricity production [16]. In Italy, the technology is growing thanks to funds derived from the PNRR (*Piano Nazionale di Resistenza e Resilienza*) equal to 1.1 billion euros, with state contributions covering up to 40% of investment costs of agrivoltaics projects, alongside with the "Parco Agrisolare" fund of 1.5 billion euros for the installation of modules on the roofs of agricultural structures , with an estimated potential agrivoltaic capacity up to $30\ GW_p$. Germany also largely invests on agrivoltaics, and the number of utility-scale installations is constantly increasing, with plants exceeding $5\ MW$ of capacity. [15][17]

Table 1: Technical potential for installed capacities of Agri-PV systems for the UAA and the different land area sub-categories and with different area coverage percentages for the EU. This is based on 0.6 MW/ha power to land area ratio. [15]

	10 % area coverage		5 % area coverage		1 % area coverage	
	Area (ha)	Potential (GW)	Area (ha)	Potential (GW)	Area (ha)	Potential (GW)
Utilised agricultural area	15 726 214	*9 436*	7 863 107	*4 718*	1 572 621	*944*
Arable land	9 793 456	*5 876*	4 896 728	*2 938*	979 346	*588*
Permanent grassland and meadow	4 877 482	*2 926*	2 438 741	*1 463*	487 748	*293*
Permanent crops	1 026 726	*616*	513 363	*308*	102 673	*62*
Market gardens	28 577	*17*	14 289	*9*	2 858	*2*

1.1 Agrivoltaic systems' technical regulations

Focusing on European Union, there is no universally accepted regulation for agrivoltaics, which is why individual Member States have adopted independent regulatory frameworks with specific and stringent numerical parameters. In Germany, the reference technical specification DIN SPEC 91434 classifies systems based on height and footprint, divided into elevated systems (Category I), which must have a minimum vertical clearance of 2.1 meters with a maximum agricultural land loss of 10%, and inter-row systems (Category II), which are placed at a height below 2.1 meters and tolerate a soil loss limit of up to 15%. The German standard also requires that the agricultural yield is guaranteed for at least 66% compared to a reference area without panels. In France, the law on the acceleration of renewable energies (APER) and its relative implementing decree mandate that the reduction in agricultural production caused by the plant must not, in any case, exceed 10%, and that the non-cultivable area due to infrastructure must be limited to a maximum of 10% of the plot. To respect this strict yield limit, sector studies highlight the need to maintain an extremely low Ground Coverage Ratio (GCR), equal to or less than 20. In Italy, the MASE Guidelines establish that, to fall within the basic definition of agrivoltaics, the surface area dedicated to agricultural activity must be at least 70% of the total area, and the maximum surface covered by photovoltaic modules (LAOR parameter) must not exceed the limit of 40%. To qualify as an 'advanced'

agrivoltaic plant and access state incentives, Italy imposes precise constraints on the minimum height of the modules, measured from the ground to the lower edge of the panel, which is 1.3 meters in the case of livestock activities, so to allow for the passage of animals, and 2.1 meters in the case of crop activities, to guarantee manoeuvring space for machinery. To this is added a further energy synergy constraint, whereby the electrical production of the advanced Italian system must never fall below 60% relative to the productivity of a standard ground-mounted photovoltaic plant. Outside of Europe, Japan also subordinates permits to primary agricultural activity, requiring the maintenance of at least 80% of original productivity, while the United States prioritizes the efficiency of agricultural productivity, allowing for only slight decreases [24][25][26][27][28][29][30]. The following table resume these fundamental requirements to illustrate the normative differences adopted among the cited countries:

Table 2: comparative regulatory frameworks for agrivoltaics

Country/Region	Regulatory Framework and Standard	Module Height	Maximum Ground Coverage Ratio (GCR) and Minimum Agricultural Yield (AY)	Key Requirement
Italy	Legislative Decree 199/2021 MASE Decree 2023	>2,1 m	GCR 40% AY 70% (of Utilized Agricultural Area)	Mandatory continuous monitoring (10 years) Reversible structures
France	Law N° 2023-175 Decree 2024-318	for elevated systems: 2 - 5 m for low elevation systems <2 m	GRC 40% AY 90% (Compared to uncovered plot)	Must directly contribute to maintaining/improving agricultural production Reversible structures
Germany	DIN SPEC 91434 EEG 2023	>2,1 m (Category I) <2,1 m (Category II)	GRC 10% (Category I) GRC 15% (Category II) AY 66% (Compared to uncovered yield)	Categorization based on height and loss of usable area
Japan	MAFF Directive 2013	>2-3 m	GRC must ensure light transmission rate of 30-50% AY 80% (Compared to original level)	Temporary permit (3 years) contingent on proving sustained agricultural productivity
United States	DOE/NREL Guidelines	2,1-3,6 m	GRC 30%-50% AY 80% (Compared to uncovered plot)	Guided by performance criteria State programs may impose fixed height minimums

1.2 Agrivoltaic system application fields

Agrivoltaics is gaining significant importance due to its ability to enhance the efficiency of a portion of land by integrating electricity generation with agricultural production, thereby increasing the Land Equivalent Ratio, with studies demonstrating that an agrivoltaic system can achieve a greater than 1.2, ensuring a soil productivity increase of over 20% compared to the separate management of the two sectors and, to achieve this objective, numerous configurations have emerged to adapt the technology to diverse environments and purposes. Agrivoltaic systems, in agriculture context, are not limited to share land with crops, but can be integrated into livestock grazing contexts, providing shelter for animals, or serve as structural alternatives for greenhouse roofing. Furthermore, unconventional systems are being deployed in urban settings,

harmoniously added in public parks, and in specialized sectors defined as aquavoltaics, such as microalgae cultivation, where the panels help stabilize water temperatures, essential parameters to enhance algae production. It is possible to distinguish into various alternatives of system, depending on the context. Firstly, there is the standard configuration where photovoltaic systems are integrated with crops, which includes different layouts such as elevated rows, inter-rows, or vertical structures, and so relying on the coexistence of modules and underlying plants. This solution not only optimizes land usage, but it has also a positive microclimatic effect, offering not only protection to hail and frost, but also shading, mitigating the thermal stress and preventing damages on plants in hot climates during warmer hours, significantly reducing evapotranspiration and preserving soil moisture ensuring irrigation water savings up to 30%, which is essential for arid regions. Parallelly, the solar grazing system integrates energy production with sheep or cattle farming, where livestock utilize the shade to reduce heat stress, and it was observed animals spending up to 70% of their time under the panels during peak irradiance, while grazing acts as a natural vegetation control, cutting maintenance costs. This approach, however, requires careful design of module heights and the protection of electrical cabling, that can be damaged by the livestock itself (to better understand the practical implementation of these systems, Figure 10 provides a comprehensive visual representation of the various technical and operational layers involved in an agrivoltaic project with agricultural machineries and livestock). The other variant analysed is represented by the integration of photovoltaic panels into greenhouses roofs, which is highly adopted in Asia and especially in China where solar greenhouses covered 1.96 million hectares in 2021, where these systems allow for humidity control and photosynthetically active radiation filtration, although they require meticulous ventilation. Finally, agrivoltaic systems find a role in urban context, where they are integrated into public parks, generating a cooling island effect capable of lowering air temperatures by up to 2°C. It also shows promise in experimental aquavoltaic contexts, such as the cited microalgae production, where partial coverage helps maintain a thermally stable environment and optimal dissolved oxygen levels, while the solar array autonomously powers water circulation machinery [19][20][22].

The table below (Table 3) summarizes the main advantages and disadvantages of the different agrivoltaic configurations examined, offering a concise overview for each field of application.

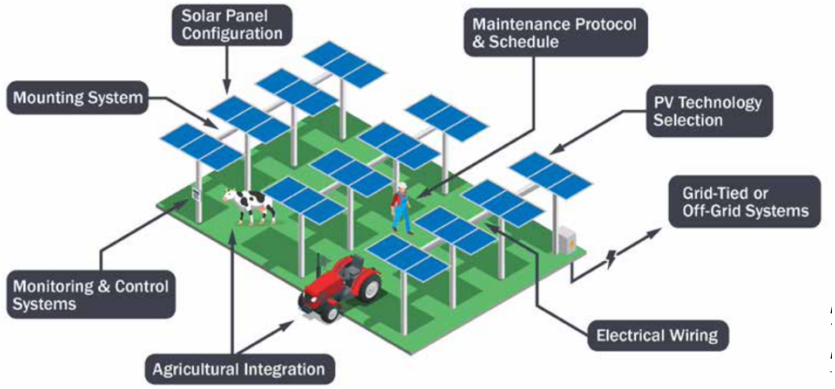

*Figure 10: Conceptual layout of an agrivoltaic system showing the integration of PV infrastructure with **livestock** and agricultural machinery [18]*

Table 3: comparison of agrivoltaics types based on advantages and disadvantages [19]

Agrivoltaics Type	Advantages	Disadvantages
Crops	• Water consumption management. • Shield from hail and natural circumstances. • Controllable microclimates help in crop yield.	• Shading on some crop types. • Soil erosion is due to water distribution. • Reduce the soil porosities.
Animals	• Provide cooler place in summer and warmer in winter. • Higher lamb production and welfare. • Increasing overall site revenue.	• Some types of goats might chew the cables. • Windy weather is challenging to the stability of the panels.
Greenhouses	• 85% of the optimal greenhouse design energy is working passively. • Reduce evapotranspiration and water loss. • Provide the needed controlled irrigation modifications.	• Plaque solar panels decrease the light on the crops. • Temperature increase in the greenhouse and ventilation is needed.
Different applications	• Provide shade in solar parks for people. • Provide charge stations in recreational parks. • Create cooler places for people in the parks.	• Obstacle for specific sports activities. • Possibility of damaging the grass of the garden.

1.3 Structural layouts and employed materials in agrivoltaic systems

The effectiveness of an agrivoltaic system depends on optimizing both energy generation and agricultural productivity, a balance strongly influenced by the local climate and the specific crop type. The supporting structures are designed to withstand environmental and operational loads and different materials are adopted, for example galvanized steel is commonly adopted for its rigidity, while aluminium offers lightness and corrosion resistance. Fiber-reinforced polymer (FRP) composites are also being tested to further reduce overall system weight. Focusing on the system geometry, key design parameters include the ground clearance, the row spacing, and the tilt angle. The system height is a crucial factor, elevated configurations accommodate agricultural machinery and protect crops from extreme weather events, whereas low mounted systems provide greater structural stability and lower capital costs, particularly in areas subject to strong wind loads that would otherwise require heavy concrete foundations. Furthermore, row spacing must be carefully designed not only to allow the passage of specific agricultural machinery but also to ensure a homogeneous distribution of solar radiation across the crops. Another relevant geometric aspect is the panel spacing, which consists of a small empty gap left between the individual modules on the same structure and which is used to limit extreme wind loads on the collectors and significantly influences the spatial distribution and heterogeneity of irradiance and rainwater amount falling on the soil and crops beneath, as visually represented in Figure 11. Finally, the tilt angle is a key parameter, which can be fixed or integrated with single-axis or dual-axis tracking systems. These dynamic systems, sometimes driven by advanced algorithms, allow for the real-time optimization of both electricity production and crop microclimate, managing aspects such as dynamic shading during peak heat or optimal rainwater distribution.

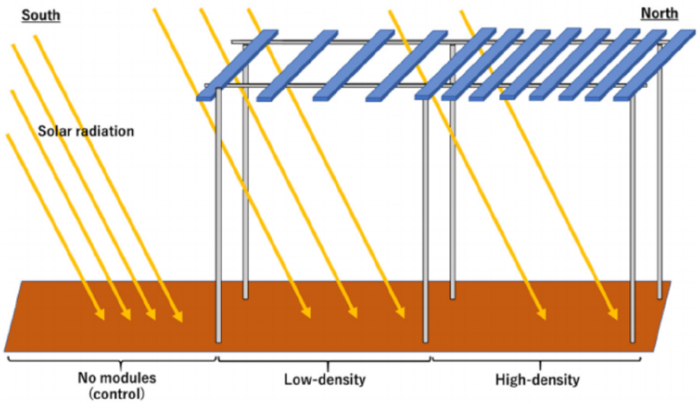

Figure 11: Scheme of solar radiation filtering through different panel spacings, assuming solar irradiation from the South [21]

The layout can range from simple parallel rows of modules to more complex solutions, such as staggered arrangements designed to modulate the light and shade distribution across the field. Modules may form a continuous canopy with a pronounced tilt angle, covering the crop and protecting it from high solar irradiation, or be installed as vertical systems positioned between cultivation rows. Light spectral management is closely tied to the chosen module technology. Crystalline silicon remains the most widely used material due to its high efficiency, but also thin-solar cells are employed (*CdTe*, *CIGS*, a-Si). In addition to traditional modules, it is spreading the use of bifacial modules, which are well suited for vertical configurations thanks to their ability to capture the reflected radiation from the ground, and the semi-transparent modules with filtering glass, commonly used in greenhouses as shown in Figure 12. Advanced technologies are also emerging, including spectrum-splitting films that convert infrared radiation into electricity while transmitting Photosynthetically Active Radiation (*PAR,* it corresponds to the region of solar irradiance spectrum comprised between 400 and $700\ \mathrm{nm}$), and Organic Photovoltaic (*OPV*) modules. The table below (Table 4) offers a comparative overview of agrivoltaic systems implemented in major countries, outlining the strategies adopted for specific crops and photovoltaic technologies, along with key performance indicators such as the Land Equivalent Ratio (*LER*) and Water Saving estimate.

Figure 12: semi-transparent modules implemented in a greenhouse [19]

Table 4: comparison of agrivoltaic systems by geographic location and key parameters [23]

Country	AVS Technology Used	Main Crops Cultivated	PV System Type	LER (%)	Water Saving
Japan	Elevated PV + Fixed Tilt	Leafy greens, rice	Monofacial	160 %	Moderate
India	Dynamic tracking + Irrigation	Tomato, wheat	Bifacial	145 %	High
Germany	Vertical PV + Smart Sensors	Potatoes, lettuce	Monofacial	186 %	Low
USA	Wide-spacing AVS	Alfalfa, berries	Bifacial	155 %	Moderate
China	Semi-transparent panels	Herbal plants	Transparent glass	130 %	High

1.4 Microclimate in agrivoltaic systems

The integration of photovoltaic arrays into an agricultural environment fundamentally alters the local microclimate and different key parameters for both photovoltaic panels and crops such as solar radiation, air temperature, and humidity. This interaction is not uniform but varies significantly depending on the system's geometry, ground clearance, distance between rows, and regional climate, directly influencing the final crop yield and the thermal behaviour of the modules themselves, as the physical presence of the array reshapes local aerodynamic patterns, modifying wind speed and turbulence intensity, and the convective heat exchange, which represents the core the focus of this work. A

visual representation of the parameters involved when taking into account the microclimate forming in an agrivoltaic system is schematised in Figure 13:

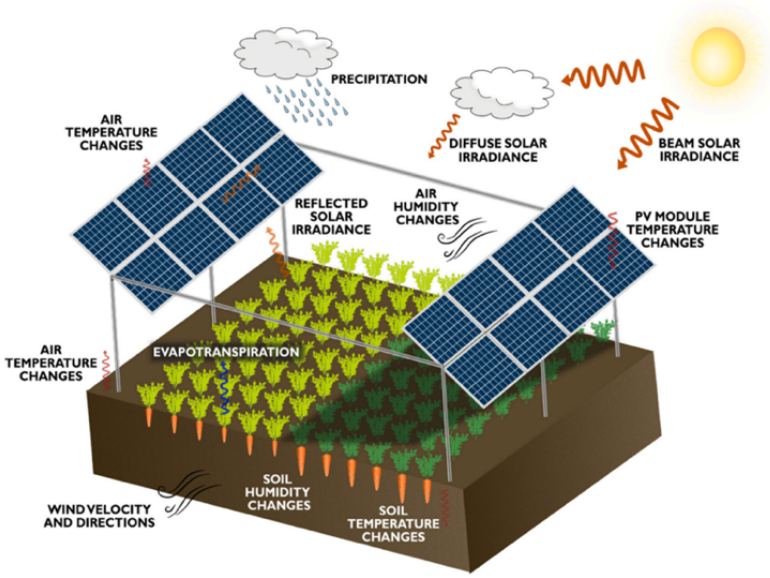

Figure 13: visual representation of the microclimate variations within an APV system [31]

1.4.1 Shading effect of agrivoltaic systems

APV systems, especially high mounted configurations, decrease the amount of Photosynthetically Active Radiation (*PAR*) reaching the crops by intercepting and blocking up to 42% of the Global Horizontal Irradiance (*GHI*) [32]. This reduction is dependent on the density and orientation of the PV modules, affecting both direct and diffuse irradiance. Consequently, focusing on how APV layouts influence the shading, and so the irradiance, on the targeted plant selection, is necessary to enhance LER and crop yields. In fact, C4 crops, such as corn, which have high light demand and consequently high light saturation point, tend to experience yield reduction, independent of the climate. Whereas C3 type, like soybean and rice, make more efficient use of reduced solar irradiance [31][33]. Furthermore, shading strongly affects the performance of agrivoltaic systems, particularly due to self-shading effect between rows. Moreover, the use of bifacial modules, especially in vertical configurations, complicates the shading analysis, making it harder to estimate the reflected irradiance reaching the rear side of the modules, as demonstrated in vertical agrivoltaic systems in

Norway [34]. To mitigate these issues, ray tracing has become a widely used technique that helps to better model the fraction of light reaching both the PV modules and the crops beneath the panels. A study showed that available *PAR* varies across different zones of a single-axis PV system, demonstrating that even in conditions of apparent full shade, a fraction of *PAR* is always present, as the rotational design prevents permanent shadows and micro-patches near the array could receive up to 91% of the PAR observed in unshaded areas. [31][35]

1.4.2 Moisture and temperature role in agrivoltaic systems

The layout of the APV structure and the dynamic shading patterns, directly affects energy and water balance at the interface between soil and air, with distinct dynamics varying across diurnal and seasonal scales. Regarding soil temperature, several studies report a decrease of up to approximately 5 °C on average compared with open-field conditions. This reduction is most pronounced during periods of peak solar irradiance and throughout the summer months, where shading limits soil heat absorption and consequently reduces heat transfer to the lower air layers. [31][32] Air temperature follows a more complex pattern. Over the diurnal cycle, shading generally lowers daily maximum temperatures. This cooling effect is particularly relevant when systems are designed to provide afternoon shade, thereby mitigating thermal stress during the hottest hours of the day. Conversely, two mechanisms can induce localized warming up to 0,7°C: convective heat released by operating modules, whose cell temperature is higher respect to adjacent panels, combined with reduced ventilation (several studies considered systems with ground clearance up to 2 m) can lead to an increase in the diurnal mean temperature within permanently shaded zones. During nighttime, the PV array acts as a thermal barrier, limiting radiative heat losses from the soil and resulting in higher minimum temperatures. [31][32][37] From a hydrological perspective, shading reduces evapotranspiration (ET, it is the loss of water from the soil both by evaporation from the soil surface and by transpiration from the leaves of the plants growing on it [38]), with reported decreases ranging from 31% to 44% depending on climate and season. This reduction, especially during dry periods, leads to substantial soil water

conservation. Several studies document volumetric soil moisture increases of up to 29% or more beneath the modules. Moreover, the presence of PV modules generates marked spatial heterogeneity in rainfall distribution at ground level. A portion of the precipitation is intercepted by the modules and channelled toward the edges of the panel rows, causing water to accumulate along the drip lines while decreasing beneath the central portions of the array, creating lateral soil-moisture gradients that further reinforce local microclimatic differentiation. [31][32]

1.4.3 Impact of wind flow on convective heat transfer and agrivoltaic systems' microclimate

The structural presence of the PV array significantly alters local wind speed and flow patterns acting as a shelter or channel to the wind. Wind speed is generally reduced underneath the arrays, with agrivoltaic systems, depending on geometry, creating a wind-sheltering effect that can cause wind velocity reductions up to 46% [35]. This reduced airflow restricts convective heat dispersion and minimizes the removal of water vapor, phenomena called evapotranspiration, directly reinforcing the APV system's microclimate effects of moisture retention and lowered evapotranspiration, and can be beneficial to prevent erosion effects [18]. However, the array's influence is complex as its layout and module inclination determine if it acts as a shield or a channel for the incoming wind. This understanding is crucial for preventing structural failures, such as torsional galloping, vortex shedding and flutter derivatives [19][35]. In fact, especially when varying the panel inclination, and depending on the wind flow direction, the effect could be an enhancement of convective heat exchange, as the panel geometry could cause a concentration of turbulence, as shown in **Errore. L'origine riferimento non è stata trovata.** [36]. The effect of the wind on the agrivoltaic system will be further analysed in the following chapter.

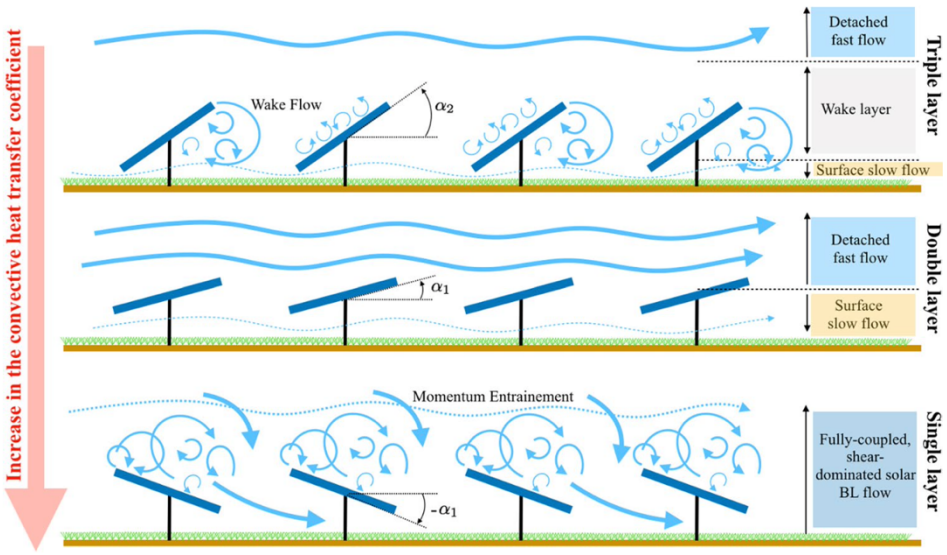

Figure 14: Impact of agrivoltaic system geometry on eddies formation and convective heat transfer

1.5 Case studies about convective and agricultural performance of agrivoltaic systems

As highlighted in the previous paragraphs, the integration of agrivoltaic systems has a profound impact on the local microclimate, altering radiation fluxes, temperature, and fluid dynamics beneath the modules. Recent scientific literature has focused extensively on two fundamental and interconnected aspects of this alteration, which are the impact on evapotranspiration, with the resulting water savings, and the variation in convective heat transfer. Regarding soil moisture, as seen, research demonstrates that the shading provided by photovoltaic panels reduces incident radiation, leading to faster stomatal closure in plants and a consequent decrease in leaf and soil evapotranspiration. This phenomenon translates into a remarkable increase in water use efficiency, and field studies have observed that shaded areas under PV panels can be significantly more water-efficient, reaching, in some scenarios, an efficiency 328% higher than in open fields, favouring soil moisture conservation especially in arid climates. Furthermore, shading mitigates thermal stress for the underlying crops, reducing irrigation needs. In parallel, fluid dynamics research has highlighted how the geometric configuration of the panels drastically influences convective heat transfer, a vital factor both for cooling the modules, which lose efficiency at high temperatures, and for the soil microclimate. Wind

tunnel studies have shown that increasing the panel height from the ground improves convective cooling, where higher configurations allow for greater entrainment of high-velocity flows under the array, increasing the Nusselt number and significantly improving heat transfer. Row spacing and ground clearance also alter wind loads and pressure distribution, modifying the aerodynamic wake structure and turbulent interactions. Changes in wind direction and panel tilt can increase the convective heat transfer coefficient by up to 45% due to variations in under-panel air velocity and wake turbulence. Moreover, the panel does not merely obstruct the airflow but redirects it, generating turbulent wakes, vortices, and alterations in the velocity profile. Depending on the configuration, the space between the module and the ground can act as an aerodynamic nozzle that accelerates the airflow directly against the soil, thinning the boundary layer and increasing convective cooling and, consequently, evapotranspiration. Conversely, other configurations can shift turbulent mixing to higher altitudes, creating a calm zone at ground level that favours moisture conservation. Studying geometric configurations, such as ground clearance and row spacing, is therefore an essential step, as it defines the delicate balance between two contrasting needs: maximizing heat exchange to cool the modules and minimizing evapotranspiration to ensure agricultural water savings. Compared to existing literature, which has often focused either only on agricultural yield or only on the cooling efficiency of PV panels, this work introduces a dual and targeted methodological approach. The innovative focus of this thesis lies in the study of convective heat transfer directly between the soil and the underlying air, formally linking it to the evapotranspiration rate through the Chilton-Colburn analogy. The main original contribution consists of the investigation method, where the problem is addressed by directly comparing experimental data obtained in a wind tunnel on a 1:75 scale model with a heated flat plate, with two-dimensional CFD numerical simulations. This hybrid approach allows not only for the evaluation of the agrivoltaic system's geometry impact on the heat transfer coefficient and soil moisture but also for testing and validating the very limits of 2D simulation tools. The work critically explores the reliability of 2D CFD simulations with the $k-\omega\ SST$ turbulence model in capturing macroscopic turbulent mixing,

highlighting the intrinsic limitations of simplified numerical models in reproducing the real fluid dynamics and thermal interactions occurring within the microclimate of an agrivoltaic system.

2 Wind interaction on agrivoltaic systems

In the study of agrivoltaic systems, the interaction between photovoltaic modules, the ground, and the underlying crops is intimately governed by the local microclimate. Within this delicate equilibrium, wind plays a primary role, acting as the main driver for the forced convective heat transfer between the surfaces, both panels and soil, and the surrounding air, as well as the fundamental vector for the mass transport of water vapor. Consequently, to fully comprehend how a specific array configuration affects the thermal regulation of the system and the water-saving potential of the soil, it is essential to first analyse the fluid dynamics of the airflow. Wind is airflow driven by the atmospheric pressure gradient and modified by the Coriolis effect and surface roughness. The atmospheric boundary layer is defined as the lowest portion of the troposphere that is directly influenced by the Earth's surface, responding to the surface forcings such as friction, sensible and latent heat exchange, and pollutant emissions within a short timescale, and its thickness is highly variable. Close to the ground, the wind profile is heavily shaped by friction against the Earth's surface, resulting in a complex velocity profile ruled by surface roughness. This behaviour is crucial for agrivoltaic systems' settings, as surface conditions, which are influenced by crops, forests or open fields, modulate the wind behaviour generating turbulence and altering the microclimate within the system. In particular, the presence of solar panels acts as an aerodynamic obstacle that deeply modifies the atmospheric boundary layer and, depending on the geometric layout, the system can either channel the airflow or shielding the wind. Understanding interactions is crucial as wind modulates fundamental mechanisms within the APV microclimate, such as the aerodynamic transport of water vapor, ruled by the evapotranspiration phenomenon, and the forced convective heat transfer, which governs the thermal regulation of both the crops and the photovoltaic modules. This chapter explores the fundamental physics of wind and details its specific implications on evapotranspiration and convection within an agrivoltaic system [39][39][41].

2.1 Wind physics

Wind is classified into three main categories called mean wind, turbulence and waves, which can coexist in the boundary layer (Figure 15) and, in fact, waves and turbulence are often super imposed on the mean wind in a reality scenario.

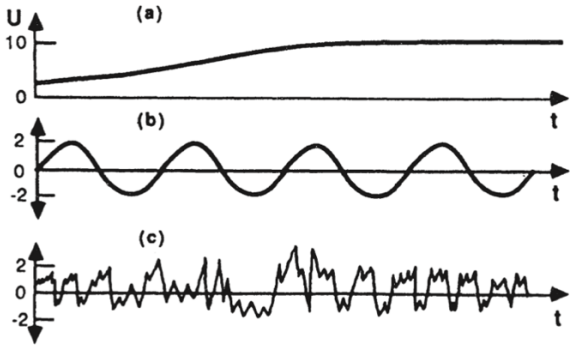

Figure 15: Idealization of mean wind (a), waves (b) and turbulence (c) alone. U is the wind velocity component in the x-direction [39]

Within the boundary layer, the transport of quantities such as moisture, pollutants, heat and momentum is dominated by mean wind in horizontal direction and by turbulence in the vertical direction. [39][41] The horizontal transport, physically defined as advection, is driven by mean winds, which are typically on the order of 2 $^{m}/_{s}$ to 10 $^{m}/_{s}$ in the boundary layer (Figure 15, case a) and, in agrivoltaic system, the advection mechanism is responsible for sweeping away the heat and water vapour accumulated beneath the photovoltaic panels, continuously bringing free stream air and replacing the stagnant air mass. Mean wind speed reach the smallest values near the ground, where the friction drag causes a slowdown of the horizontal wind, with a null value when mean wind is directly in touch with the ground. It results in a logarithmic velocity profile that increase with the height in the surface layer zone (Figure 16).

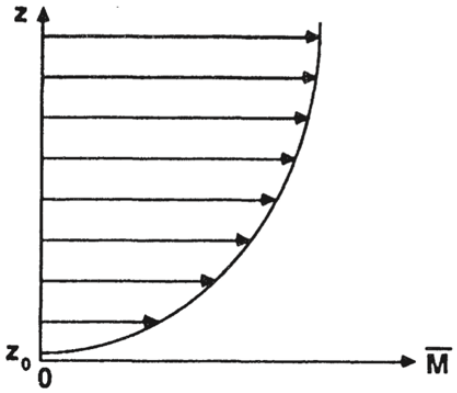

Figure 16: logarithmic variation of mean wind speed $\overline{M}$ with height, which is the z-coordinate [39]

In fact, the atmospheric boundary layer is divided into different areas that varies with height, and the first layer, directly in touch with the surface, is called the surface layer, characterized by the null velocity at ground level mentioned before. In a well-mixed boundary layer, schematized in Figure 17, which typically occurs during day time when the surface has been heated up by the solar energy, the mean wind speed near the ground assumes a logarithmic trend, that can be expressed as Equation 1 [39]:

Equation 1

$$\overline{U}(z) = \frac{u_*}{k} ln\left(\frac{z}{z_0}\right)$$

where $\overline{U}(z)$ represents the mean wind speed as a function of the vertical coordinate z, which is the height above the ground, u_* is the friction velocity representing the surface stress exerted by the wind, and k is the von Karmann constant, an empirically derived dimensionless value typically taken as ~ 0.4. Finally, z_0 is the aerodynamic roughness length, which characterize the surface roughness and depends on the specific ground or terrain profile.

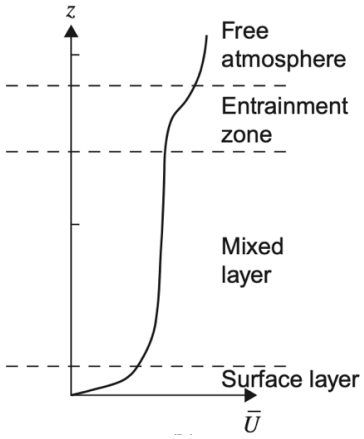

Figure 17: mean zonal wind speed [39]

Equation 1 is valid for stable conditions in the surface layer within the atmospheric boundary layer, but the actual airflow near the ground is unstable due to continuous interactions between the moving air mass and the surface roughness, which creates a strong vertical velocity gradient, physically defined as wind shear, that combined with thermal effects, triggers dynamic instabilities that cause the smooth mean flow to continuously break down into chaotic fluctuations, called turbulences. Turbulences are characterised by irregular and unpredictable swirls of motion called eddies, caused by forcings from the ground and are superimposed on the mean wind. These eddies are of different size and intensity and are defined within the turbulence spectrum, with large turbulences which are usually related to solar heating, as the ground heated up during sunny days causes the warmer air to rise, while colder air descend in lower areas. Smaller scale eddies, on the other hand, are caused by frictional drag on the air flowing above the ground or by the deflection of the wind flow caused by obstacles such as trees, buildings or structures such as the panels. Therefore, the highest number of turbulences is expected to be in the surface layer, due to the eddies dependence on the surface roughness and to quantify this effect the turbulence intensity I is defined, expressed as follow (Equation 2) [40]:

Equation 2

$$I = \frac{\sigma_U}{\overline{U}}$$

where $\overline{U}$ represents the mean wind speed and σ_U is the standard deviation of the wind speed, expressing the diffusion of wind speed respect to the mean value and is mathematically linked with velocity fluctuations and, higher the fluctuations of wind speed values, higher the turbulence intensity. Furthermore, when wind interacts with the agrivoltaic system, significant aerodynamical forces are generated, and the analysis of these loads is essential to improve the performance of the system and prevent possible failures. The forces involved are schematized in Figure 18 and their resultant can be expressed as the following equation (Equation 3) [42][43]:

Equation 3

$$\vec{F} = \iint_{\partial V} \vec{\tau} - p\vec{n}dS$$

where $\vec{F}$ is the total aerodynamical force acting on the photovoltaic panel, p is the pressure generated by the fluid flow, $\vec{n}$ is the normal vector respect to the panel surface, $\vec{\tau}$ is the tensor of shear stresses and ∂V is the surface containing the panel volume. This resultant force is typically decomposed into two primary components relative to the direction of the incoming mean wind, which are the drag force, that acts parallel to the free stream airflow and represents the physical resistance exerted by the structure against the wind and the lift force, that acts perpendicular to the airflow direction and is primarily driven by the pressure differential established between the upper and lower surfaces of the tilted panels. These components can be described as follow:

Equation 4

$$F_L = F\cos(\alpha)$$

Equation 5

$$F_D = F\sin(\alpha)$$

where α is angle between the inclined solar panel and the direction of the airflow buffeting the surface. In the structural and aerodynamic analysis, these forces are conventionally expressed in dimensionless by normalizing with the dynamic pressure of the undisturbed flow, defined in Equation 6, and the reference area of the panels.

Equation 6

$$q = \frac{1}{2}\rho\left|\overrightarrow{U_\infty}\right|^2$$

where $\overrightarrow{U_\infty}\ \left[\frac{m}{s}\right]$ is the wind speed vector in free flow and $\rho\ \left[\frac{kg}{m^3}\right]$ is the fluid density. By normalizing through this parameter, the results are two dimensionless forms, which are the drag and lift coefficients (Equation 7 and respectively Equation 8):

Equation 7

$$C_D = \frac{F_D}{q\ S_R}$$

Equation 8

$$C_L = \frac{F_L}{q\ S_R}$$

where $S_R\ [m^2]$ is the reference surface mentioned previously. Accurately quantifying these aerodynamic loads is of fundamental importance, as extreme drag and lift forces, combined with dynamic fluctuations frequently caused by vortex shedding, are the primary drivers of mechanical fatigue and structural failure in solar arrays.

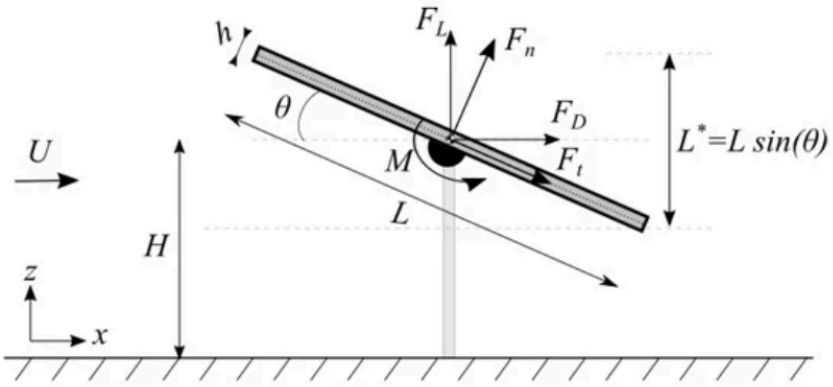

Figure 18: schematic of a solar panel and aerodynamical forces involved [42]

2.2 Wind and evapotranspiration

Evapotranspiration is a key parameter for comprehending the climate behaviour of a given region. Its significance was initially formalized in 1948 by C. W. Thornwaite through the Precipitation and Evaporation (*P/E*) index, defined in Equation 9 [47], which correlates the water inputs to a system, defined as monthly precipitation (*P),* with the system's water outputs, expressed as potential evapotranspiration (*E*).

Equation 9

$$P/E\ index = \frac{total\ monthly\ precipitation}{evapotranspiration}$$

By establishing this relationship, Thornthwaite defined five distinct humidity regions based on the resulting P/E Index value, which describe a progressive transition from environments where precipitation heavily outweighs potential evapotranspiration to those where evaporative demand is dominant. Specifically, a high index identifies a wet climate, typically associated with rainforests, and, as the available moisture decreases, the climate transitions to subhumid and subsequently to semiarid and arid regions, with different types of vegetation associated. This classification scheme is summarized in Table 5:

Table 5: Climate Regions defined by Thornwaite's P/E index [47]

Humidity province	Vegetation	P/E index
A (wet)	Rainforest	>127
B (humid)	Forest	64 -127
C (subhumid)	Grassland	32 - 63
D (semiarid)	Steppe	16 - 31
E (arid)	Desert	<16

Evapotranspiration is primarily influenced by net radiation and wind speed, and consequently by turbulence patterns, and its rates are strongly modulated by the air humidity. The amount of water evapotranspired (ET_0, $\left[\frac{mm}{day}\right]$) is mathematically defined by the FAO Penman-Monteith equation (Equation 10) [44][49]:

Equation 10

$$ET_0 = \frac{0.408\Delta_{sat}\left(R_n - Q_{ground}\right) + \gamma\frac{900}{T}u_2\delta_e}{\Delta_{sat} + \gamma(1 + 0.34u_2)}$$

where R_n is the net radiation on the crop surface, Q_{ground} is the soil heat flux density and Δ_{sat} represents the sensitivity of saturation pressure towards temperature, which is the equivalent of the slope of vapour pressure curve. Furthermore, γ is a psychometric constant and δ_e is the vapour pressure deficit, defined as the difference between the saturation and the actual vapour pressure. Finally, T is the mean daily air temperature at 2 meters height and u_2 is the corresponding wind speed at the same height. The aerodynamic term $\gamma\frac{900}{T}u_2\delta_e$ at the numerator is directly influenced by wind speed and correspond to the shrink of the boundary layer above crop surface, governing the turbulent transport of vapour from the plant's surface to the atmosphere. This transport is driven by the gradient in vapour pressure δ_e, which quantifies the degree of air saturation, and a higher deficit increases the air capacity to absorb moisture, thereby enhancing evapotranspiration. Consequently, the evapotranspiration demand reaches its maximum under hot and dry weather conditions, where the air possesses a high capacity for storing water vapor, and where wind may promote the transport of vapour

away from the surface, facilitating greater absorption. On the contrary, under humid weather conditions, the high air humidity and the presence of clouds cover, contribute to a lower evapotranspiration rate. In an agrivoltaic system, the presence of solar arrays exerts a sheltering effect, acting as an aerodynamic barrier that reduces the mean wind speed at the canopy level, and inducing this microclimatic alteration significantly restricts the continuous replacement of saturated air with drier ambient air. A visual representation of this dynamic is provided in Figure 19, which schematizes the effect of rising wind speed on the reference evapotranspiration rate under both hot and dry, and humid and warm weather conditions.

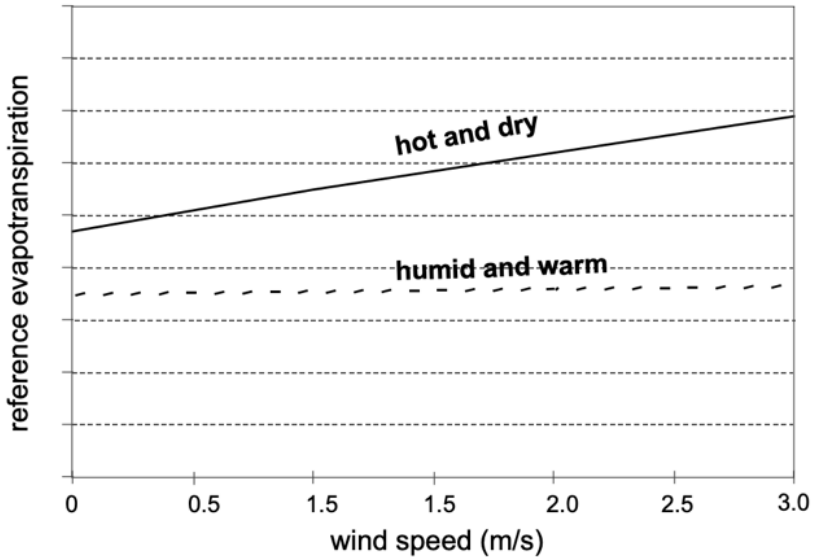

Figure 19: effect of wind speed on evapotranspiration in hot-dry and humid-warm weather conditions [49]

To model the evapotranspiration phenomenon, electrical analogy and energy balance models are frequently employed. An example is the "flux gradient model" by Kaimal and Finnigan (Equation 11) which expresses the vapour flux toward the atmosphere considering both a stomatal and an aerodynamic resistance [45]:

Equation 11

$$LE = \frac{s^* - s_{ref}}{r_{st} - r_a}$$

where LE $\left[\frac{kg}{m^2 s}\right]$ is the vapour flux, s^* $\left[\frac{kg}{m^3}\right]$ is the vapour concentration within the stoma, which are the pores of the leaves, and s_{ref} $\left[\frac{kg}{m^3}\right]$ is the concentration at a reference height. At the denominator, r_{st} $\left[\frac{s}{m}\right]$ is the stomatal resistance and r_a $\left[\frac{s}{m}\right]$ is the aerodynamic resistance, expressed in Equation 12 [43]:

Equation 12

$$r_a = \frac{u(z)}{u^{*2}}$$

where $u(z)$ $\left[\frac{m}{s}\right]$ is the wind speed at height z and u^* $\left[\frac{m}{s}\right]$ is the friction velocity. The shield effect of the agrivoltaic system enhance the effect of the aerodynamic resistance and, by limiting the efficient transport of water vapor, the crop's water demand is significantly decreased, promoting the conservation of soil moisture. This effect is particularly advantageous in arid climates and to cut the costs of irrigation.

2.3 Wind and convection

Convective heat transfer is a fundamental mechanism within an agrivoltaic system, ruling the thermal regulation of both the photovoltaic modules and the ground. Convection is classified into natural convection, which develops when temperature differences produce density variations within the fluid, generating buoyancy-driven flows that persist as long as thermal gradients are present, and forced convection, which occurs when an external flow, such as the wind, moves past a surface, establishing a velocity and thermal boundary layer where momentum and heat are exchanged. Convection is described by Newton's Law, defined as Equation 13, which correlates the fluid characteristics with the heat flux:

Equation 13

$$q = h(T_w - T_f)$$

where $q\ \left[\frac{W}{m^2}\right]$ is the heat flux, $T_w\ [K]$ is the wall temperature of the object buffered by the fluid, $T_f\ [K]$ is the fluid temperature and $h\ \left[\frac{W}{m^2 K}\right]$ is the convective heat transfer coefficient, which is a function of various parameters such as the geometry of the object and the density of the fluid. The convective heat transfer coefficient can be mathematically derived from the Nusselt number $Nu\ [-]$, which describes the entity of convective heat transfer compared to conduction. The Nusselt number definition varies depending on the forced convection or natural convection flow regime [46]. For forced convection, the Nusselt number is expressed as an empirical function by considering various parameters, as shown in
Equation 14:

Equation 14

$$Nu = a\ Re^b Pr^c$$

where a, b and c are constants, $Re\ [-]$ is the Reynolds number, which defines the fluid flow regime, establishing the threshold between laminar flow, where boundary conditions do not change in time, and turbulent flow, where fluid flow properties vary randomly and chaotically. And $Pr\ [-]$ is the Prandtl number, that highlights the thermophysical features of the fluid and defines the thickness of the velocity boundary layer respect to the thermal boundary layer. The Prandtl number is defined as:

Equation 15

$$Pr = \frac{\mu c_p}{\lambda}$$

where $\mu\ \left[\frac{kg}{m*s}\right]$ is the dynamic viscosity, $c_p\ \left[\frac{J}{kgK}\right]$ is the specific heat at constant pressure and $\lambda\ \left[\frac{W}{mK}\right]$ is the thermal conductivity of the fluid. While, for natural convection, it is possible to describe the convection correlation with
Equation 16:

Equation 16

$$Nu = a\ (Gr\ Pr)^b$$

where a and b are constants and Gr $[-]$ is the Grashof Number, correlating buoyancy and viscosity within a fluid. The product between Gr and Pr is also defined as Rayleigh Number Ra $[-]$, describing whether strong convection or conduction is the main heat exchange mechanism within the fluid flow. The convective heat transfer coefficient can be derived by the Nusselt number as follow (Equation 17):

Equation 17

$$h = \frac{Nu\ \lambda}{L}$$

where L $[m]$ is characteristic length of the surface. To model evapotranspiration, and thus water evaporation, the Chilton and Colburn analogy between heat and mass transfer, in the case of turbulent forced convection, is adopted, allowing the mass transfer of water vapour from a wet surface to be treated through the equivalent heat transfer problem of a heated surface under the same flow conditions. Under these assumptions, it is possible to calculate the water evaporation coefficient (which is the mass transportation coefficient h_m) correlating Nusselt number Nu from
Equation 14 with Sherwood number expressed in the following equation (Equation 18) under same conditions, which means using the same coefficients a, b and c:

Equation 18

$$Sh = a\ Re^b Sc^c$$

where the Sherwood number correlates viscosity with heat diffusion, while Sc is the Schmidt number describing the relation between viscosity and mass transfer. These two dimensionless numbers can be expressed as:

Equation 19

$$Sh = \frac{h_m L}{D}$$

Equation 20

$$Sc = \frac{\mu}{\rho D}$$

where $L\ [m]$ is a characteristic length, $\mu\ \left[\frac{kg}{m*s}\right]$ is the dynamic viscosity, $\rho\ \left[\frac{kg}{m^3}\right]$ is the fluid density, $D\ \left[\frac{m^2}{s}\right]$ is the mass diffusion coefficient and $h_m\ \left[\frac{m}{s}\right]$ is mass transfer coefficient. Through

Equation 14 and Equation 18, substituting Equation 15,

Equation 16, Equation 19 and Equation 20, it is possible to extrapolate the value of h_m as:

Equation 21

$$h_m = h_t \left(\frac{D^2}{\lambda^2 \rho c_p}\right)^n$$

This result is valid considering an exponent n equal to $\frac{1}{3}$, as originally proposed by Chilton and Colburn, establishing a direct proportion between convective heat transfer coefficient and mass transfer coefficient. In conclusion, wind strongly influences convective heat transfer and plays a key role in agrivoltaic systems, and higher wind speeds generally increase convective cooling by removing warm air near the surface and replacing it with cooler ambient air. Conversely, reduced wind speed weakens forced convection, which can lead to higher air and canopy temperatures, affecting the whole system as cooling effect is a crucial aspect in PV systems, as higher panels working temperature induces a reduction in conversion efficiency. Furthermore, it is correlated with evapotranspiration assuming Chilton and Colburn analogy and correlating mass transport coefficient with heat transfer coefficient [40].

2.4 The case of heated smooth plate to study the agrivoltaic system

To understand the fundamental mechanisms of convective heat transfer between the ground and the air within an agrivoltaic system, it is useful to compare the complex fluid dynamics of this setup with the theoretical benchmark of a smooth flat plate subjected to parallel airflow in a forced convection regime. In the absence of obstacles, when a fluid flows over a heated flat plate, the local convective heat transfer coefficient (h_x) is

not constant along the surface. At the leading edge of the plate, at longitudinal position $x = 0$, the thickness of both the velocity boundary layer (δ_v, Equation 22) and the thermal boundary layer δ_t, Equation 23) is theoretically zero. In this position, the resistance to heat transport is at its minimum and consequently, the convective heat transfer coefficient reaches its maximum value. As the flow proceeds along the longitudinal direction, viscous effects and thermal diffusion progressively propagate further into the fluid in the direction normal to the surface, resulting in the simultaneous growth of both thermal and velocity boundary layers (Figure 20 and Figure 21 respectively).

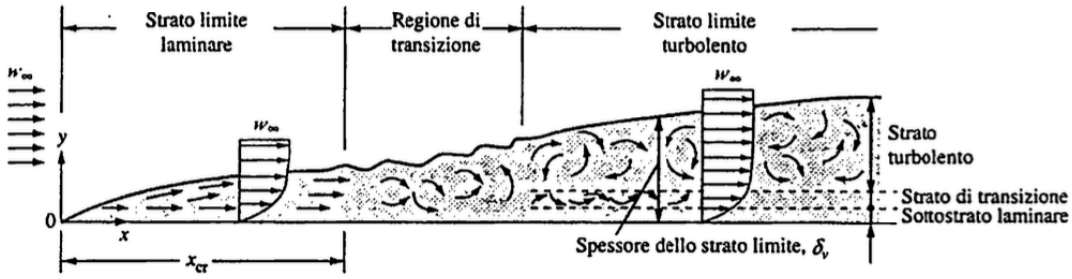

Figure 20: Boundary layer development and flow regimes over a heated flat plate [50]

Equation 22

$$u = 0.99\, u_\infty$$

where u_∞ is the velocity of the undisturbed free stream. The equation mathematically defines the velocity boundary layer as the distance from the surface where the local fluid velocity reaches 99% of the free stream velocity. The formula assumes this form due to the no-slip condition, which forces the fluid at the wall to a complete stop and, at the exact location of the leading edge, this thickness is zero because the free stream has just encountered the surface, leaving no physical space for viscous friction to propagate normal to the flow.

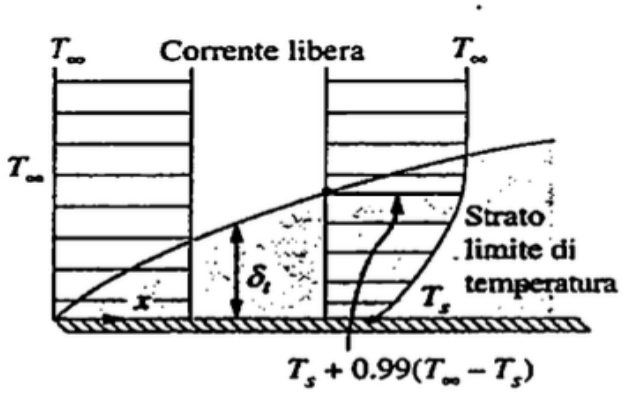

Figure 21: Thermal boundary layer over a flat plat [50]

Equation 23

$$\delta_t = T - T_s = 0.99(T_\infty - T_s)$$

where T_s is the surface temperature and T_∞ is the temperature of the undisturbed free stream, and it mathematically defines the thermal boundary layer as the distance from the surface where the temperature difference reaches 99% of the total thermal gradient. At the leading edge, this thickness is zero because the fluid has just encountered the heated surface, leaving no physical space for thermal diffusion to propagate normal to the flow but, as the fluid advances along the longitudinal direction, the heat transfer progressively penetrates deeper into the free stream, causing the thermal boundary layer to grow. In a turbulent regime, which for a flat plate occurs at a critical Reynolds number greater than $5 \cdot 10^5$, due to intense fluctuations and rapid macroscopic mixing, heat transmission is significantly higher than in a laminar flow but, as the flow proceeds along the longitudinal direction, the inevitable and continuous thickening of the boundary layers (as shown in Figure 20 and Figure 21) act as an insulating layer, increasing the thermal resistance between the surface and the undisturbed free stream fluid and, therefore, resulting in a natural asymptotic decay of the convection coefficient, which decreases proportionally to $x^{-\frac{1}{5}}$ along the flow direction. In fact, this behaviour can be mathematically described by the empirical correlation for the local friction coefficient ($C_{f,x}$, Equation 24) and local Nusselt number (Nu_x, Equation 25) for a turbulent flow over an isothermal flat plate:

Equation 24

$$C_{f,x} = 0.0592\, Re_x^{-\frac{1}{5}}$$

The relevance of this fluid dynamic parameter in a heat transfer analysis is governed by the Reynolds analogy. For gases such as air, the Prandtl number is approximately equal to 1, meaning that momentum and thermal energy diffuse through the fluid with almost identical intensity. In a turbulent boundary layer, the rapid fluctuations and intense macroscopic mixing of fluid particles simultaneously enhance both the momentum transport and the heat transmission. Consequently, a strict physical correlation exists between the viscous friction drag exerted on the surface and the convective heat transfer. Because the exact same turbulent eddies are responsible for forcing cooler air against the plate, enhancing convection, and for transferring momentum, causing friction, the local friction coefficient and the local heat transfer coefficient inevitably will share the same physical and mathematical trend.

Equation 25

$$Nu_x = 0.0296\, Re_x^{\frac{4}{5}}\, Pr^{\frac{1}{3}}$$

where Re_x represents the local Reynolds number while Pr is the Prandtl number. The local Reynolds number is directly proportional to the longitudinal coordinate x, as defined by the following relationship:

Equation 26

$$Re_x = \frac{u \cdot x}{\nu}$$

where u is the longitudinal free stream velocity, x is the longitudinal position from the leading edge of the flat plate and ν is the kinematic viscosity. Consequently, by substituting Equation 26 into Equation 25, it can be demonstrated that the local Nusselt number increases proportionally to $x^{\frac{4}{5}}$ and, by isolating the local convective heat transfer coefficient from Nusselt number, it yields:

Equation 27

$$h_x = \frac{Nu\,\lambda}{x}$$

Since this calculation requires dividing the Nusselt number, which grows as $x^{\frac{4}{5}}$, by x itself, the operation results in an exponent of $-\frac{1}{5}$, explaining why the convective heat transfer coefficient experiences the asymptotic decay as initially described, exactly as the local friction coefficient previously defined in Equation 24. This behaviour is visually summarized in Figure 22, which illustrates how both the local convective heat transfer coefficient and the local friction coefficient exhibit the demonstrated asymptotic decay in the turbulent region. This reduction is driven by the thickening of the boundary layer along the x-axis, which brings with it an increasing in viscous and thermal resistance.

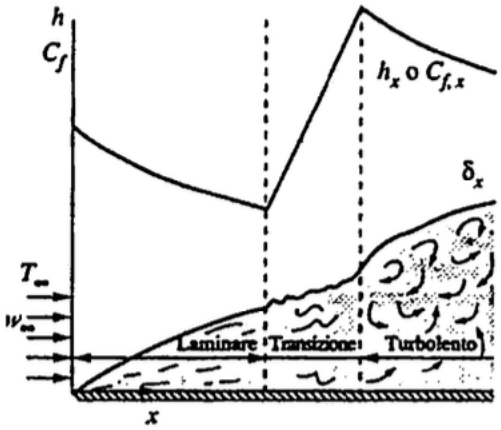

Figure 22: C_f and h longitudinal variation and boundary layer development along a flat plate [50]

The introduction of photovoltaic arrays completely disrupts this orderly progression because, in an agrivoltaic system, the modules act as geometric obstacles that oppose the airflow, preventing the continuous and undisturbed development of the boundary layer along the ground. In fact, each row of panels induces abrupt aerodynamic deviations, triggering phenomena such as flow separation, wake formation, and extensive recirculation zones beneath and downstream of the modules, which amplify the turbulent kinetic energy and forcibly remix the fluid. As known from convection theory, this turbulent motion involves intense macroscopic mixing where rapid

fluctuations and eddies bring fluid particles at different temperatures into close contact, drastically increasing momentum transport and the heat transfer. This phenomenon can be explained by analysing both the velocity field, where streamlines reveal the effective deflection of the flow and the separation of the wake, and the vorticity field, which is useful to highlight the turbulence activity and that can be defined as follow (Equation 28):

Equation 28

$$\omega_{z,norm} = \left(\frac{\partial v}{\partial x} - \frac{\partial u}{\partial y}\right)\frac{d_1}{u_\infty}$$

where *u* and *v* represent the longitudinal and vertical mean velocity components respectively and their variations along the *x*-axis and *y*-axis. Physically, this parameter provides a microscopic measure of the local rotation of a fluid element within the flow, which is strictly driven by the wind shear, meaning that the fluid spins on itself due to the differential sliding velocities between adjacent fluid layers. Following the mathematical convention, a positive value of vorticity indicates a counterclockwise rotation, whereas a negative value denotes a clockwise rotation. While the velocity streamlines in Figure 23 show the global deflection of the flow and the formation of the wake behind the panel representing the change in the longitudinal velocity module, the vorticity map in Figure 24 highlights the intense turbulent activity and the local rotation of fluid elements, where these high vorticity magnitudes, originated at the leading and trailing edges of the module, mark the origin of flow separation, as abrupt changes in velocity gradients trigger the development of the turbulent wake.

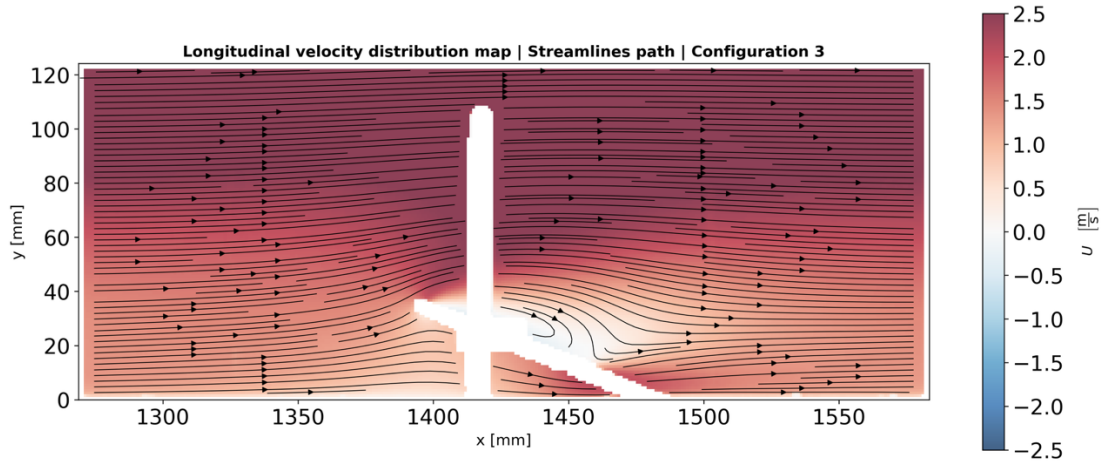

Figure 23: Velocity field and streamlines path of the airflow for one configuration. The colour scale represents the variation of the longitudinal velocity, illustrating the global deflection of the free stream and the low-velocity wake region developed downstream of the panel

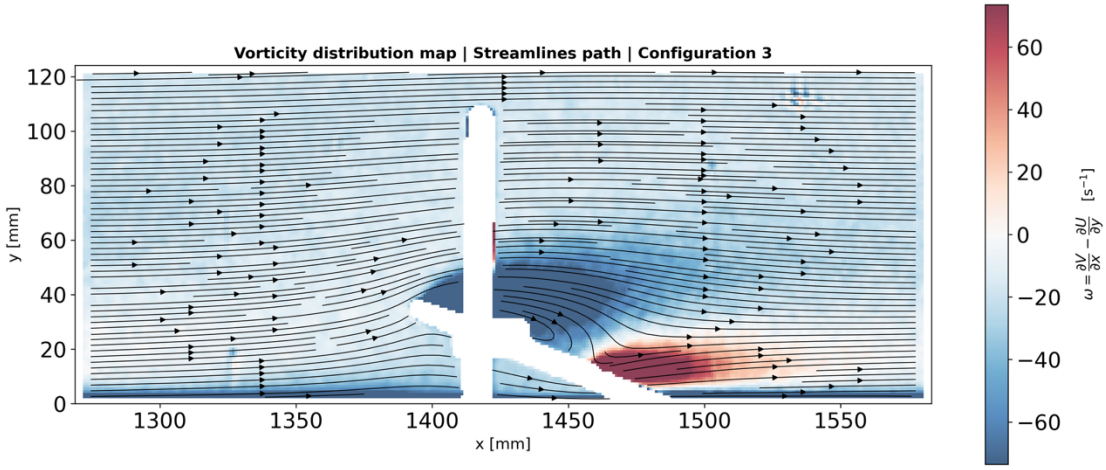

Figure 24: Vorticity map and streamlines path for one configuration. The colour scale visually translates the outcome of Equation 28, where deep blue regions represent strong negative values (clockwise rotation), while intense red regions denote positive values (counterclockwise rotation).

Due to these localized concentrations of turbulence, the flow impacting the ground beneath and downstream of each panel undergoes continuous mixing and, from a thermodynamic perspective, the flow recirculation and wake separation repeatedly shrink the thermal and velocity boundary layers. These intense mixing processes force the cooler air from the free stream into close contact with the heated surface, resulting in a local thinning of the boundary layer that drastically reduces thermal resistance, therefore bringing the convective heat transfer coefficient to higher values. This mechanism explains why the trend of the convection coefficient along the x-axis in an

agrivoltaic system does not follow the continuous decay of a free plate but is instead characterized by cyclic peaks and oscillations, as will be studied in the following chapters, where each oscillation in the convective heat transfer coefficient trend corresponds to the perturbation introduced by the module (visual example in Figure 25). This continuous thinning process counteracts the natural decay of heat transfer, allowing the agrivoltaic system to maintain a convective heat transfer coefficient that is, on average, higher and more dynamic across the entire domain compared to a simple flat plate.

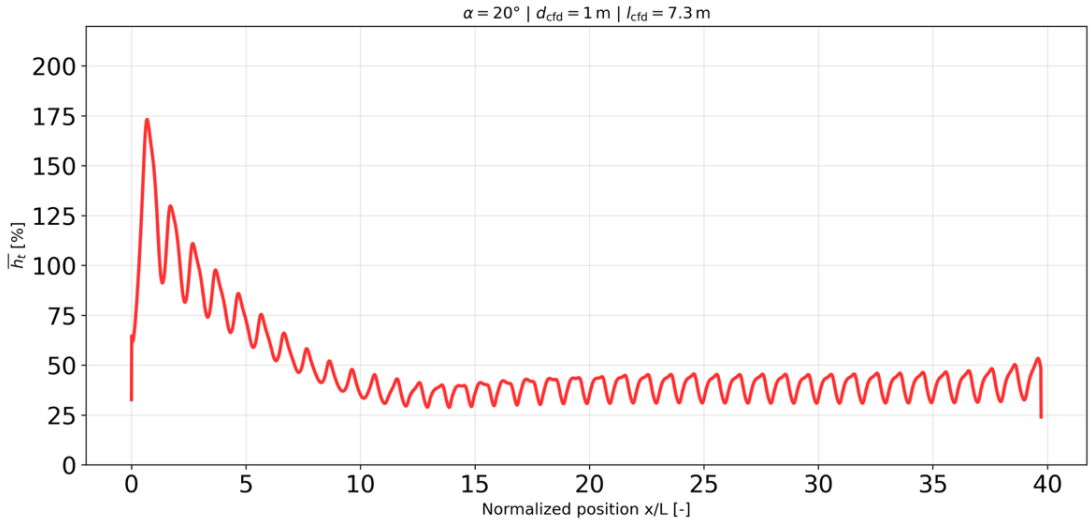

Figure 25:Variation of the convective heat transfer coefficient along the normalized flow direction. The values are expressed as a percentage relative to the empty-domain scenario, to visualize the effect of the presence of the panels

In conclusion, the analysis of the physical principles conducted so far demonstrates that the wind represents the actual promoter of the agrivoltaic microclimate. Through the Chilton-Colburn analogy, it has clearly emerged how the convective heat transfer and the evapotranspiration rate are phenomena inextricably linked to each other: modulating one inevitably means influencing the other. The theoretical comparison with the smooth flat plate has also highlighted that the photovoltaic modules do not merely shield the sun or the wind, but act as complex aerodynamic obstacles. By generating turbulent wakes, flow separations, and vortices, the panels interrupt the natural growth and decay of the boundary layer, causing its continuous mixing and thinning, which

translates into drastic localized peaks of the convective heat transfer coefficient. For the purposes of the general reasoning of this thesis, what has been understood in this chapter constitutes a fundamental premise. Since fluid dynamics so markedly alter the thermal and moisture exchanges at the ground, the evaluation of agrivoltaic performance cannot rely solely on theoretical estimates. It is precisely this physical complexity that makes the methodological investigation presented in the next chapters indispensable. Through the comparison between experimental wind tunnel tests and CFD numerical simulations, it will indeed become possible to quantify exactly how specific geometric configurations, such as ground clearance and row spacing, manage to govern this turbulence, empirically defining the delicate compromise between maximizing convective cooling and preserving water in the agricultural soil.

3 Methodology

This chapter details the methodological framework adopted to investigate the convective heat transfer within an agrivoltaic system. To achieve a comprehensive understanding of these complex phenomena, a dual approach is employed, combining scaled experiments with numerical simulations. After describing the focus of the analysis, the first section describes the experimental campaign conducted inside the wind tunnel, detailing the facility, the scaled models, and the measurement techniques used to acquire both thermal and aerodynamic data. The second section outlines the Computational Fluid Dynamics approach, introducing the governing equations and the turbulence model. Finally, the strategy of analysis of the convective heat transfer coefficient and the technique employed to extract the data are described.

3.1 Case studies

The convective heat transfer coefficient was studied across three different agrivoltaic configurations, which have been analysed, as depicted along the chapter, both through wind tunnel experiments and CFD simulations, whose data have been provided by École Centrale de Lyon. Specifically, the studied agrivoltaic systems aim to represent a typical system located in the Northern Hemisphere, where the photovoltaic modules are oriented towards the South to maximize solar irradiance. The wind is assumed to be blowing from the North, thus impacting the rear face of the tilted modules, flowing over the structure from the back to the front. The first setup is the baseline configuration, which in the CFD simulations is characterized by a ground clearance of *1 m* and a row spacing of *7.3 m* and, starting from this baseline case, two other geometries were studied to evaluate the impact of specific geometric changes. The first change was increasing the ground clearance, with the panel height tripled to *3 m*, while the last one involves row spacing, where the distance between the modules was tripled to *21.9 m*. All these experimental values refer to the 1:75 scale models tested in the wind tunnel at the École Centrale de Lyon, as summarized in in the table below (Table 6). Regarding the

CFD simulations, the numerical models were developed to be identical to the experimental ones, maintaining the same 1:75 scale and geometric parameters for all three cases. Similarly, the boundary conditions and the setup in Ansys Fluent were specifically chosen to replicate the wind tunnel environment, ensuring that the longitudinal velocity matches the experimental case of $5\ \frac{m}{s}$. This consistency is essential to allow for a precise comparison between the numerical results and the experimental data, focusing on how each geometric variation affects the flow field and the resulting convective heat exchange at the ground.

Table 6: experimental configurations data

	α [°]	**d [cm]**	**l [cm]**
configuration 1	*20*	*1.3*	*10*
configuration 2	*20*	*3.9*	*10*
configuration 3	*20*	*1.3*	*30*

3.2 Wind tunnel experiments' methodology

Wind tunnel experimentation offers the advantage of capturing the intrinsic three-dimensional complexity of turbulence, allowing for the quantification of the actual heat transfer at the ground. This approach makes it possible to include all turbulent contributions triggered when the airflow impacts the modules of the agrivoltaic system. This section describes the experimental methodology and the origin of the data. It outlines the overall setup of the wind tunnel experiments and details the procedures employed to acquire both aerodynamic and thermal data, thereby establishing the experimental baseline for evaluating the agrivoltaic system.

3.2.1 Experiments' data

The data elaborated in this work are extracted from previous experiments, whose data have been provided by the École Centrale de Lyon.

3.2.2 Experiments' set up in the wind tunnel

The experiments were conducted in the wind tunnel of the *Laboratoire de Mécanique des Fluides et d'Acoustique* (LMFA) at the École Centrale de Lyon. The structure is a close-loop wind tunnel that measures 7.2 meters in width, 24 meters in length, and 7.4 meters in height, with an actual test section, where the scaled model was positioned, which is 12 meters long, 3.6 meters wide, and 2 meters high. The airflow is generated by a large fan located in the upper part of the structure, capable of producing a wind speed of up to 5 m/s within the measurement section.

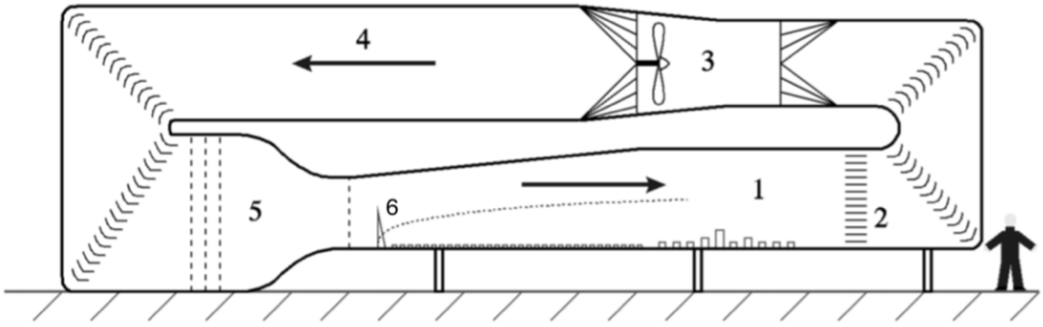

Figure 26: sketch of the Wind tunnel of the LMFA of the École Centrale de Lyon representing Test Section (1); Heat exchanger system (2); Fan (3); Diverging section (4); Converging section and turbulence grid (5); Irwin spires (6)

To ensure the development of a mature and fully developed atmospheric boundary layer along the test section, Irwin spires are positioned upstream, followed by roughness elements made of wood arranged on the floor. Inside the test section, the floor is equipped with a rotating panel, which can be heated to simulate different conditions. This engineering solution allows moving the scaled models of the photovoltaic panels and varying their orientation with respect to the main direction of the incident airflow.

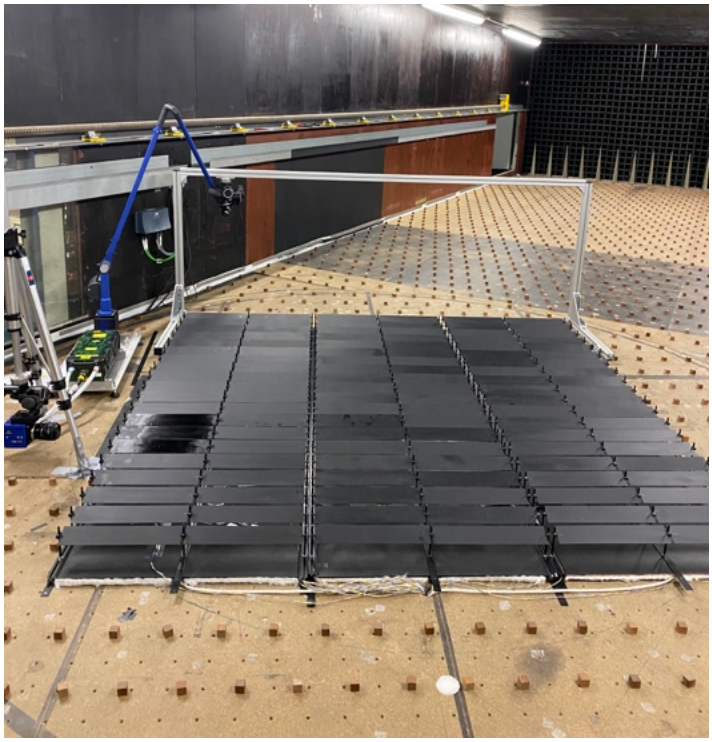

Figure 27: PV model on the rotating panel, with a LDA on the left. In the background the Irwin spires are visible.

In order to characterize the thermo-fluid dynamic interaction between the panels and the ground, the facility is equipped with several precision instruments. The mapping of the velocity field, considering the two-dimensional nature of the flow of interest, is performed by using the Particle Image Velocimetry (*PIV*) optical technique. The *PIV* requires the introduction of tracer particles, called seeding particles, into the gaseous flow, then by the usage of laser beams, it is possible to get the instantaneous extraction of the flow field around the obstacles. Concurrently, the reference wind velocity profile is constantly monitored using a Pitot tube connected to a digital micromanometer, which ensures the accuracy of the flow conditions imposed by the fan. The Pitot tube's purpose is to characterize the upper portion of the wind profile, so to measure the height of the boundary layer. It faces the air flow, measuring the total pressure, also called stagnation pressure, given by the sum of static pressure and dynamic pressure as described in Equation 29:

Equation 29

$$p_{tot} = p_{static} + \frac{1}{2}\rho u^2$$

Rearranging this formula, it is possible to obtain the module of the velocity (Equation 30):

Equation 30

$$u = \sqrt{\frac{2(p_{tot} - p_{static})}{\rho}}$$

Figure 28: The micromanometer that provides the pressure, and the thermometer of the wind tunnel chamber

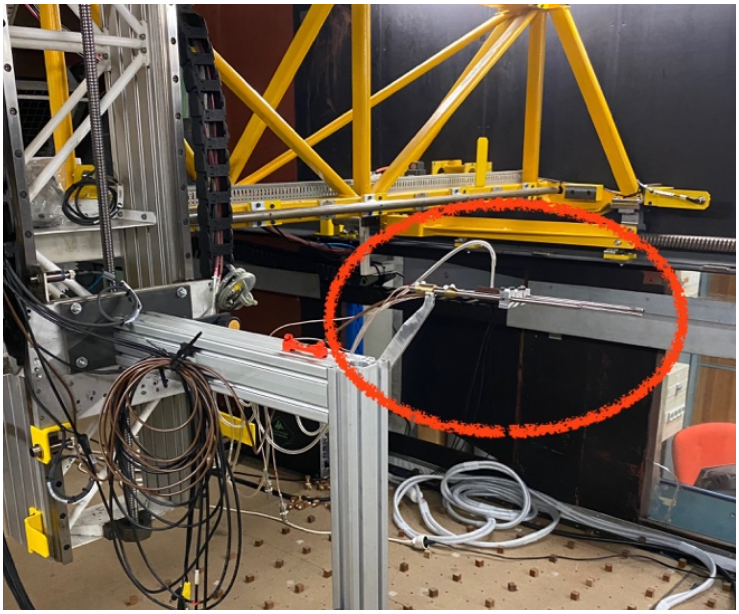

Figure 29: Pitot tube in the measurement section, rounded by a red line

To simulate the soil heating, the rotating floor panel is equipped with embedded electrical resistances, while a DC power supply is used to provide energy to these resistances, which produce heat by the Joule effect, a process governed by the following relationship:

Equation 31

$$P = \frac{V^2}{R}$$

where V represents the applied voltage and R the electrical resistance of the heating elements. The surface temperature distribution is then monitored and validated using a thermal camera, whose images are post-processed and spatially calibrated to correct optical distortions and ensure the homogeneity of the thermal field.

Figure 30: DC power supply (Sorensen SGA 100/50)

The measurement campaign was structured into four sequential phases. The first phase consists of collecting baseline data, where measurement is performed at room temperature, before the ground heating is activated, and in the absence of wind, in order to calibrate the instrumentation and define the reference initial conditions of the system. Subsequently, the ground heating process is gradually performed, increasing the voltage provided by the DC power supply in steps of approximately 15 V each, to avoid thermal shocks to the system. The goal is to reach a maximum target voltage of 92 V, which corresponds to an imposed heat flux on the rotating panel of approximately $300\ \frac{W}{m^2}$. Once this target voltage is reached, a mandatory waiting period of one and a half hour is imposed to allow the rotating plate to heat uniformly and reach thermal steady-state. At the end of this transient phase, a second measurement is performed to acquire data relating exclusively to the natural convection regime. The third phase involves the introduction of the fluid dynamic forcing, activating the wind tunnel fans and setting a regime of 1480 rpm, which translates to a wind speed inside the test chamber of $5\ \frac{m}{s}$, which is monitored using the laboratory micromanometer. Following the activation of the wind, the system is left to stabilize for an additional 40 minutes, allowing the boundary layer to fully develop over the heated models and for the thermal field to resettle into a forced convection condition. Finally, after the stabilization period has terminated, the ultimate and definitive fluid dynamic and thermal data collection

campaign proceeds. Each measurement consists of 100 successive samplings, which correspond more less to 12 minutes, and the entire temporal evolution of the collected data is monitored, recorded, and saved in real-time via the wind tunnel's laboratory computer for the subsequent post-processing phase. However, experimental modelling does not constitute a perfect replica of the open-field conditions. This discrepancy is attributable, firstly, to the scale effects intrinsic to the reduction ratio (1:75) and, secondly, to the unavoidable presence of auxiliary components within the physical model, such as support structures, cables, and sensors. These elements act as additional aerodynamic obstacles, triggering parasitic 3D turbulence and lateral mixing that partially alter the clarity of the phenomenon generated by the photovoltaic modules alone.

3.3 CFD simulations' methodology

The use of Computational Fluid Dynamics (CFD) serves as a predictive tool to rapidly evaluate the influence of geometric and climatic variations on wind distribution and temperature profiles. In particular, the adoption of a two-dimensional RANS approach allows for a drastic reduction in computational overhead and processing time, facilitating the extension of the investigation to full-scale operating conditions and thus overcoming the constraints imposed by experimental scaling. Consequently, CFD stands as a fundamental, fast, and cost-effective resource for guiding the macroscopic design of agrivoltaic plants and assessing preliminary aerodynamic loads, while leaving the task of validation to physical experimentation. On the other hand, CFD presents intrinsic limitations, especially in its two-dimensional formulation, as the 2D simplification implicitly assumes an infinite width of the panels, completely ignoring three-dimensional lateral mixing and flow edge effects. Furthermore, these numerical models may overestimate the aerodynamic shielding effect of the panels, failing to capture the actual dispersion of turbulent kinetic energy that occurs in three-dimensional space. This section describes the numerical methodological approach and the origin of the data. It outlines the overall setup of the Computational Fluid Dynamics simulations and describes the governing equations and turbulence models used to replicate the

aerodynamic and thermal fields, thereby establishing the computational framework for evaluating the agrivoltaic system.

3.3.1 CFD simulations' data

The CFD data used in this work, which have been post-processed both on ANSYS Fluent and Paraview, have been extracted from 2D CFD simulations provided by the École Centrale de Lyon.

3.3.2 Numerical Validation: Navier-stokes equations

Governing equations of fluid flow are derivations of fundamental principles of conservation. In particular, the conservation of the mass of the fluid, the conservation of momentum and the conservation of energy. These three equations, known as Navier-Stokes equations, are obtained regarding the fluid as a continuum and describing the fluid on terms of macroscopic properties: velocity u, pressure p, density ρ and temperature T by studying a fluid point, which is the smallest element of fluid where these macroscopic properties are not influenced by individual molecules and whose size allows to express accurately them on its faces by just considering the first two terms of Taylor series expansion. It must be considered also the hypothesis of having an incompressible fluid (which means considering the density ρ constant), which is possible for a Mach number below 0.3, and it is obtained as follow:

Equation 32

$$M = \frac{u}{a}$$

where u is the wind velocity, and a is the speed of sound, equal to $343\ \frac{m}{s}$ (for $T_{air} = 20\ °C$), and of having a turbulent flow, which is defined by proving the Reynolds number to be greater than $5 \cdot 10^5$ as explained previously for the case of the flat plate.

3.3.2.1 Conservation of mass

The mass conservation equation is derived by applying a mass balance to a fluid element, which means that the temporal change of mass inside the element is balanced by the net mass flux through its surface. This principle can be written in vector form and leads to the continuity equation:

Equation 33

$$\frac{\partial \rho}{\partial t} + \nabla \cdot (\rho \vec{u}) = 0$$

where $\vec{u}$ is the velocity vector and ρ is the density, and it describes a steady-state and three-dimensional case for a compressible fluid. Adding the hypothesis of compressible fluid, with constant ρ, it becomes:

Equation 34

$$\nabla \cdot (\vec{u}) = 0$$

In this form it ensures that the fluid mass is conserved, meaning that the volume of fluid entering and exiting the control volume has the same value.

3.3.2.2 Conservation of momentum

The momentum conservation equation is based on the Lagrangian approach, as it regards the change of properties of a moving fluid particle, describing its change of momentum as the sum of forces acting on it. These forces are categorized into surface forces (such as pressure and viscous forces) and body forces (such as centrifugal, Coriolis and electromagnetic force). In most fluid dynamics applications these body forces effects are represented as source terms.

For an incompressible fluid, the conservation of momentum is expressed as:

Equation 35

$$\rho \left(\frac{\partial \vec{u}}{\partial t} + \vec{u} \cdot \nabla \vec{u} \right) = -\nabla p + \mu \nabla^2 \vec{u} + \vec{f}$$

And under steady-state conditions it simplifies as:

Equation 36

$$\rho(\vec{u} \cdot \nabla\vec{u}) = -\nabla p + \mu\nabla^2\vec{u} + \vec{f}$$

where $\vec{u}$ is the velocity vector, p is the pressure, ρ is fluid density, μ is the dynamic viscosity and $\vec{f}$ represent the source term for any external body forces, specifically the gravitational force equal to $\rho\vec{g}$, where $\vec{g}$ is the gravitational acceleration.
Physically, in Equation 36, the term $\vec{u} \cdot \nabla\vec{u}$ represents the convective acceleration, linked to the fluid particle migrating through regions with different velocity. The term $\mu\nabla^2\vec{u}$ is the viscous diffusion term, dependant from the molecular collisions between adjacent fluid layers. Finally, the pressure gradient ∇p represent the pressure forces exerted by the surrounding fluid.

3.3.2.3 Conservation of energy

The conservation of energy for a fluid particle is governed by the First Law of Thermodynamics, which states that the rate of change of energy of a fluid particle is equal to the sum of the net rate of heat addition and the net rate of work done by external forces. When studying heat transfer for an incompressible fluid and assuming the absence of internal heat sources, the conservation of energy can be expressed as:

Equation 37

$$\rho c_p \frac{\partial T}{\partial t} + \rho c_p \vec{u} \cdot \nabla T = \lambda\nabla^2 T$$

under steady-state conditions it simplifies to:

Equation 38

$$\rho c_p \vec{u} \cdot \nabla T = \lambda\nabla^2 T$$

where T is the local temperature, λ is the thermal conductivity of the fluid and c_p is the specific heat at constant pressure. Within this formulation, it is possible to distinguish

between the term $\rho c_p \vec{u} \cdot \nabla T$, which describes convective heat transfer, and the $\lambda \nabla^2 T$ conductive term, that represents thermal diffusion through the fluid.

3.3.3 Boussinesq approximation

In fluid dynamics, the Boussinesq approximation is a widely used method for modelling buoyancy-driven flows, such as natural convection. The fundamental idea behind this approach is to neglect density variations within the governing equations, except for those buoyancy terms where density is multiplied by the gravitational acceleration, considering density as a function of temperature, varying linearly with it. This approximation is valid only for small temperature variations, allowing the fluid to be considered as incompressible and meaning that inertial differences are assumed to be negligible, thereby enabling the continuity equation to be written as shown in Equation 34. The linear correlation between temperature and density is expressed as follows:

Equation 39

$$\rho = \rho_0 \big(1 - \beta (T - T_0)\big)$$

where ρ_0 is the reference air density estimated at the reference temperature T_0 and $\beta \left[\frac{1}{K}\right]$ is the thermal expansion coefficient. Consequently, we can rewrite the source term in Equation 36 as:

Equation 40

$$\vec{f} = \rho_0 \beta (T - T_0) \vec{g}$$

representing the buoyancy term that governs the fluid motion due to density differences induced by temperature. The $\rho_0 \vec{g}$ term, called hydrostatic component, is neglected as it is balanced by the hydrostatic pressure gradient within the pressure term of Equation 36. Thus, the momentum conservation in Equation 36 evolves into:

Equation 41

$$\rho(\vec{u} \cdot \nabla \vec{u}) = -\nabla p + \mu \nabla^2 \vec{u} + \rho_0 \beta (T - T_0) \vec{g}$$

3.3.4 Numerical model – RANS

The aim of the computational fluid dynamic simulations is to solve the Navier-Stokes equations using various methods with different computational cost. The most accurate and detailed is the *Direct Numerical Simulation* (*DNS*), which solves the fluid dynamics equations directly but requires a large computational cost. For this reason, it is preferred the *Reynolds-Averaged Navier-Stokes* (*RANS*) approach, with a lower computational cost, making it more suitable for most engineering and industrial problems. The RANS method is based on decomposing the flow field quantities into a mean component and a time fluctuating component, in this way:

$$x = \bar{x} + x'$$

where x is the instant value of a fluid property, $\bar{x}$ is its mean value and x' is the time fluctuating term. This way is possible to decompose all the fluid quantities involved in Navier-Stokes equations as:

Equation 42

$$\vec{u} = \bar{\vec{u}} + \vec{u}'$$

Equation 43

$$p = \bar{p} + p'$$

Equation 44

$$T = \bar{T} + T'$$

where $\bar{\vec{u}}$ is the averaged velocity vector, $\bar{p}$ is the averaged pressure and $\bar{T}$ is the averaged temperature, while $\vec{u}'$ is the time fluctuating component of the velocity vector, p' is the time fluctuating component of pressure and T' is the time fluctuating component of the temperature. Substituting these decomposed variables within steady-state Navier-Stokes equations (Equation 34, Equation 38, Equation 41), the RANS equations are obtained:

Equation 45

$$\nabla \cdot \left(\bar{\vec{u}}\right) = 0$$

Equation 46

$$\rho\left(\bar{\vec{u}}\cdot\nabla\bar{\vec{u}}\right)=-\nabla\bar{p}+\mu\nabla^2\bar{\vec{u}}-\rho\nabla\cdot\overline{\vec{u}'\vec{u}'}+\rho_0\beta(\bar{T}-T_0)\vec{g}$$

Equation 47

$$\rho c_p\left(\nabla\cdot\left(\bar{\vec{u}}\bar{T}\right)\right)=\lambda\nabla^2\bar{T}-\rho c_p\left(\nabla\cdot\left(\overline{\vec{u}'T'}\right)\right)$$

All the mean values of isolated fluctuations are erased, like in Equation 45, but the additional terms where fluctuation are multiplicated between each other are not null mean turbulent effects. In particular, the additional term in Equation 46 $\overline{\vec{u}'\vec{u}'}$ is called Reynold stress tensor, while the additional term of Equation 47 $\overline{\vec{u}'T'}$ is the heat turbulent transport.

3.3.5 Turbulence models

These additional terms of Equation 46 and Equation 47, which appear due to interactions between various turbulence fluctuations, are predicted with various turbulence models. The most used are the $k-\varepsilon$ model (with ε being the rate of dissipation of the turbulence kinetic energy k) and the $k-\omega$ model (with ω being the turbulence frequency), both needing two additional transport equations to be solved along with the RANS flow equations. The simulations shown in this work are performed selecting the $SST\ k-\omega$ (Shear Stress Transport) turbulence model, which is a hybrid model that combines the precision of the $k-\omega$ model for the near-wall regions with the free-stream independence of the $k-\varepsilon$ model in the far field. It incorporates several improvements: first, the ε-dependent equations are reformulated by expressing ε as $k\omega$. Subsequently, to achieve a smooth transition between the transformed $k-\varepsilon$ model and the standard $k-\omega$ model, blending functions F_c are introduced. This approach allows the introduction of model constants C_1 for the $k-\omega$ model and C_2 for the transformed $k-\varepsilon$ model, according to the following function:

Equation 48

$$C=F_cC_1+(1-F_c)C_2$$

with F_c tending to zero at the wall and reaching unity in the far field, producing a smooth transition around a distance halfway. This ensures a combination between the good near-wall behaviour of the $k-\omega$ model and the robustness of the transformed $k-\varepsilon$ model in the far field. Furthermore, to compute the Reynold stress tensor term and the heat turbulent transport term, the Boussinesq relationship is used, leading to Equation 49 and Equation 51 respectively:

Equation 49

$$\overline{\vec{u}'\vec{u}'} = \nu_t \boldsymbol{S} - \frac{2}{3}k\boldsymbol{I}$$

where k is the turbulent kinetic energy, $\nu_t \left[\frac{m^2}{s}\right]$ is the turbulent kinematic viscosity and $\boldsymbol{I}$ is the identity matrix. $\boldsymbol{S}$ is the strain rate tensor, which is defined as:

Equation 50

$$\boldsymbol{S} = \nabla\bar{\vec{u}} + \left(\nabla\bar{\vec{u}}\right)^T$$

Equation 51

$$\overline{\vec{u}'T'} = -\frac{\nu_t}{Pr_t}\nabla\overline{\mathrm{T}}$$

where Pr_t is the turbulent energy Prandtl number, used to relate the eddy diffusivity of momentum to the eddy diffusivity of heat. To find the turbulent kinematic energy k and the kinematic turbulent viscosity ω, which are the unknows, calculations are made through the $SST\ k-\omega$ turbulence model equations:

Equation 52

$$\frac{\partial}{\partial t}(\rho k) + \frac{\partial}{\partial x_i}(\rho k u_i) = \frac{\partial}{\partial x_j}\left(\Gamma_k \frac{\partial k}{\partial x_j}\right) + \tilde{G}_k - Y_k + S_k$$

Equation 53

$$\frac{\partial}{\partial t}(\rho\omega) + \frac{\partial}{\partial x_i}(\rho\omega u_i) = \frac{\partial}{\partial x_j}\left(\Gamma_\omega \frac{\partial \omega}{\partial x_j}\right) + G_\omega - Y_\omega + D_\omega + S_\omega$$

where $\tilde{G}_k$ represents the turbulence kinetic energy generative term due to mean velocity gradient and G_ω the generation of kinematic turbulent viscosity. Γ_k and Γ_ω are the effective diffusivities of turbulent kinetic energy and kinematic turbulent viscosity respectively, and Y_k and Y_ω are their dissipation due to turbulence. Finally, S_k and S_ω

are the source terms and D_ω is the cross-diffusivity term. In steady-state conditions the equations turn into:

Equation 54

$$\vec{u} \cdot \nabla k = \nabla \cdot (\Gamma_k \nabla k) + G_k - Y_k + S_k$$

Equation 55

$$\vec{u} \cdot \nabla \omega = \nabla \cdot (\Gamma_\omega \nabla \omega) + G_\omega - Y_\omega + D_\omega + S_\omega$$

To summarize, the $SST\ k-\omega$ turbulence model is preferred as it is an hybrid model that integrates the accuracy of the $k-\omega$ model near the wall, and the robust $k-\varepsilon$ model equations in the free stream, and the blending functions allow to neglect the sensitivity of the $k-\omega$ model to arbitrary far-field values, making it more reliable to various inlet conditions.

3.4 Technique of comparison

This section aims to discuss the technique of comparison between the experiments' data and numerical simulations' data. In particular, the results are focused on the heat transfer coefficient h_t, to highlight the effect of the presence of photovoltaic panels, varying their main geometric parameters, which are row spacing l, and the height of the panel bottom angle respect to ground d. Specifically, it has been analysed, for both experimental cases and numerical simulations cases, the trend of the mean convective heat transfer coefficient between the photovoltaic panels and the ground $\overline{h_t}$ along the horizontal direction *x*, calculated by normalizing the mean heat transfer with the panel $\overline{h_{t,with\ panels}}$ by the mean heat transfer coefficient of the empty domain $\overline{h_{t,empty\ domain}}$, referred as the flat plate, which is picked as reference case. This was done to better analyse the impact of the presence of the panels on the ground, resulting in the following formula:

Equation 56

$$\bar{h_t} = \frac{\overline{h_{t,with\ panels}}}{\overline{h_{t,empty\ domain}}}$$

This value is later multiplied by 100 to get a percentage value, to better figure out the discrepancy between reference case and the case with the panels on the ground. It will be noticed that for the simulations results, the trend will not follow a clean descendance till a convergence value as expected, similarly to a flat heated plate under turbulent flow, but oscillations will be present, due to the presence of the photovoltaic panels, that concentrate the turbulence and cause distortion in the fluid flow. To analyse the discrepancy between CFD simulations' results and experiments' results, it was considered the values of turbulent kinetic energy and longitudinal velocity, which governs the macroscopic transport of the fluid mass over the domain. In a forced convection regime, a rapid longitudinal airflow acts mechanically by sweeping away the warm air stagnating near the ground, thus restricting the growth and thickening of the thermal and velocity boundary layers, as discussed previously. This continuous replacement of fluid with cooler free-stream air reduces the thermal resistance, directly increasing the local Reynolds number (Equation 26) and, consequently, the convective heat transfer coefficient, according to the Nusselt number correlation expressed in Equation 27. Alongside the mean flow, the turbulent kinetic energy plays a crucial role by quantifying the chaotic energy and the intensity of the eddies. For two-dimensional velocity fields, assuming isotropic turbulence to compensate for the unmeasured third spatial component, the turbulent kinetic energy for the experiments is calculated from the longitudinal and vertical velocity standard deviation, as expressed in the following equation:

Equation 57

$$k = \frac{3}{2}\left(\frac{1}{2}(\sigma_u^2 + \sigma_v^2)\right)$$

where σ_u and σ_v are the standard deviations of longitudinal and vertical velocity components respectively, while the term $\frac{3}{2}$ is introduced to account for the unmeasured

third spatial dimension, which is the transversal *z*-direction, by applying the assumption of isotropic turbulence, implying that the velocity fluctuations are statistically equal in all directions. The physical correlation between these turbulent fluctuations and the heat exchange is governed by the Reynolds analogy, which states that momentum and thermal energy diffuse through the fluid with almost identical intensity. In an agrivoltaic system, the photovoltaic modules act as geometric obstacles that trigger flow separation, generate extensive recirculation zones, and create highly turbulent wakes as depicted in the previous chapter. The resulting is an intense macroscopic mixing where turbulent eddies actively draw cooler fluid from the free stream and violently force it against the heated ground and this cyclic recirculation repeatedly disrupts and shrinks the thermal boundary layer, breaking the thermal resistance and generating localized peaks in the convective heat transfer coefficient, which counteract its natural asymptotic decay. Finally, the intrinsic nature of these eddies and the overall turbulence tendency are investigated through the evaluation of the vorticity field, which highlights the local rotation of the fluid and the positions of flow separation and turbulence generation. In the two-dimensional domain of this study, the vorticity is mathematically evaluated with the formula analysed in the previous chapter (Equation 28).

3.5 Extraction of data

As previously mentioned, the objective of this study is to compare the convective heat transfer coefficient across three different agrivoltaic configurations, specifically a baseline system, a configuration with increased spacing between rows, and one with increased ground clearance. All values of convective heat transfer coefficient are normalized relative to a reference case, represented by a flat plate exposed to the wind. To analyse the differences between CFD simulations and experimental results for the normalized heat transfer coefficient, the study examines the profiles of turbulent kinetic energy and longitudinal velocity, in function of the height of the system, at various coordinates along the bidimensional domain. The convective heat transfer coefficients for both the experimental and CFD cases, including the reference flat plate, were

provided by the École Centrale de Lyon in Excel format, and have been processed using Python scripts to generate comparison graphs of the normalized convective heat transfer coefficient values for each of the three configurations. Specifically, regarding the experimental convective heat transfer coefficient, the raw data were originally acquired through a grid of heat flux meters distributed across the heated flat plate along both the longitudinal and transversal axes, as illustrated in Figure 31. For the purpose of this analysis, the experimental data were exclusively extracted from the linear array of sensors located at the transversal coordinate of 27 cm. This specific alignment was selected because it features the highest spatial density of flux meters along the *x*-axis, thereby providing the maximum longitudinal resolution for the experimental curve. Furthermore, due to the defined row spacing of the scaled agrivoltaic model utilized in the wind tunnel, the majority of these physical sensors were positioned in the open gaps between two consecutive rows of panels, and this specific arrangement is a fundamental aspect that must be carefully considered when comparing the discrete experimental data points with the continuous profiles generated by the CFD simulations, that consider all the domain. These sensors measured the total heat flux, from which the analytically estimated radiative component was subtracted to isolate the pure convective flux, as the conductive heat losses through the underlying substrate were considered negligible. The radiative heat flux was evaluated utilizing the Stefan-Boltzmann law, whose expression is:

Equation 58

$$q_{rad} = \varepsilon\sigma(T_w^4 - T_\infty^4)$$

Where ε represents the surface emissivity, which was assumed equal to 1 under the hypothesis of black body, σ is the Stefan-Boltzmann constant, whose value is $5.67 \cdot 10^{-8}\ \frac{W}{m^2K^4}$, T_w is the local wall temperature of the flat plate and T_∞ is the free-stream fluid temperature. The local convective heat transfer coefficient was then derived applying Newton's law of cooling, which was described in Equation 13, obtaining the following relationship:

Equation 59

$$h_{exp,x} = \frac{q_{conv}}{T_w - T_\infty}$$

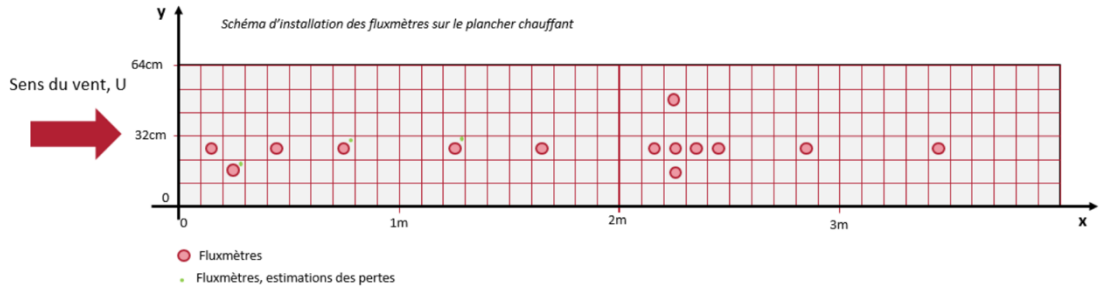

Figure 31: fluxmeters' position scheme within the heated flat plate

Regarding the turbulent kinetic energy, the experimental data were provided in Excel format, while the numerical data were extracted using Ansys Fluent, which is a software typically used for modelling fluid flow and heat transfer in different geometries, as a post-processing tool. Similarly, the longitudinal velocity values were extracted from provided Excel files for the experimental case, while Paraview, a software which permits to extract and visualize fluid dynamics parameters, was used to extract the corresponding CFD profiles. Subsequently, these different datasets were integrated using Python scripts to compare the CFD and experimental profiles within the same graphs. By plotting both the turbulent kinetic energy and the longitudinal velocity as a function of the height at strategic *x*-coordinates, which are the areas before the leading edge and after the trailing edge and the space between rows, it was possible to evaluate how accurately the numerical model replicates the physical phenomena observed experimentally in the wind tunnel. This comprehensive comparison at specific positions is fundamental to understand the impact of each configuration on the ground convective heat exchange and the precision of bidimensional CFD simulations. Finally, vorticity data were analysed by comparing distribution maps. These maps were generated using a Python script for the experimental data, which have been calculated by using the data provided in Excel format by École Centrale, while the numerical

simulations' maps were obtained by post-processing the simulations' results in Ansys Fluent. Comparing these maps provides a broader perspective on vorticity phenomena and helps clarify the discrepancies between experimental results and numerical models.

4 Results

The present chapter is dedicated to the presentation and analysis of the results obtained from the dual investigative approach adopted for this study. Before analysing the performance of the three agrivoltaics system configurations, it is fundamental to ensure the reliability of the reference data. Therefore, the first step involves the validation of the experimental reference case, which is the flat plate. This is achieved by comparing the experimental profiles of the Nusselt number and the convective heat transfer coefficient with the theoretical values expected for a flat plate in a turbulent flow. Furthermore, a direct comparison is performed between the experimental and CFD results for the reference heat transfer coefficient profiles. Since the entire study relies on the normalization of data relative to this baseline, verifying its consistency with theory is essential to guarantee the accuracy of all subsequent comparisons. Once the reference case is validated, the analysis focuses on the normalized convective heat transfer coefficient along the longitudinal x-axis for the three studied configurations. The experimental trends are directly compared with the CFD results to evaluate the numerical model's performance in predicting ground heat exchange. To further investigate and validate the differences observed between the experimental and numerical convective heat transfer coefficient values, the study examines the profiles of longitudinal velocity and turbulent kinetic energy. By overlaying the experimental and CFD data for longitudinal velocity and turbulent kinetic energy at specific locations, it is possible to verify if the discrepancies in the thermal results are linked to how the numerical model replicates the aerodynamic wake and the turbulence intensity generated by the panels. This cross-validation between thermal and fluid-dynamic parameters provides a comprehensive understanding of the physical phenomena governing the system.

4.1 Reference case validation and comparison

Before evaluating the thermal and fluid-dynamic impact of the agrivoltaic system's modules, it is mandatory to validate the reference case, which is represented by the unobstructed heated flat plate which, as previously detailed in the methodology, serves as the fundamental baseline used to normalize the local convective heat transfer coefficients in all subsequent configurations featuring the photovoltaic arrays. To ensure the absolute reliability of this baseline, first, the experimental wind tunnel data are validated against theoretical fluid-dynamic correlations and, subsequently, these validated experimental results are employed to benchmark the 2D Computational Fluid Dynamics model.

4.1.1 Theoretical validation of the experimental data

The experimental data acquired in the wind tunnel are initially compared to classical theoretical correlations for forced convection over a flat plate in a turbulent regime. To ensure a rigorous validation, the analysis is conducted in two sequential steps by, firstly, evaluating the dimensionless Nusselt number to verify the fluid-dynamic accuracy, and subsequently, assessing the dimensional convective heat transfer coefficient to validate the consistency of the reference case. In fact, the local Nusselt number physically represents the ratio of convective to conductive heat transfer across the fluid boundary layer that forms along the smooth flat plate, and in conditions of uniform turbulent flow, the theoretical Nusselt number is governed by the Reynolds analogy, which establishes a strict physical equivalence between momentum transport and heat transfer. According to this analogy, the Nusselt number is expected to follow the empirical correlation defined in Equation 25, growing proportionally to $Re_x^{\frac{4}{5}}$, where Re_x is the local Reynolds number, which linearly increases along the longitudinal coordinate.

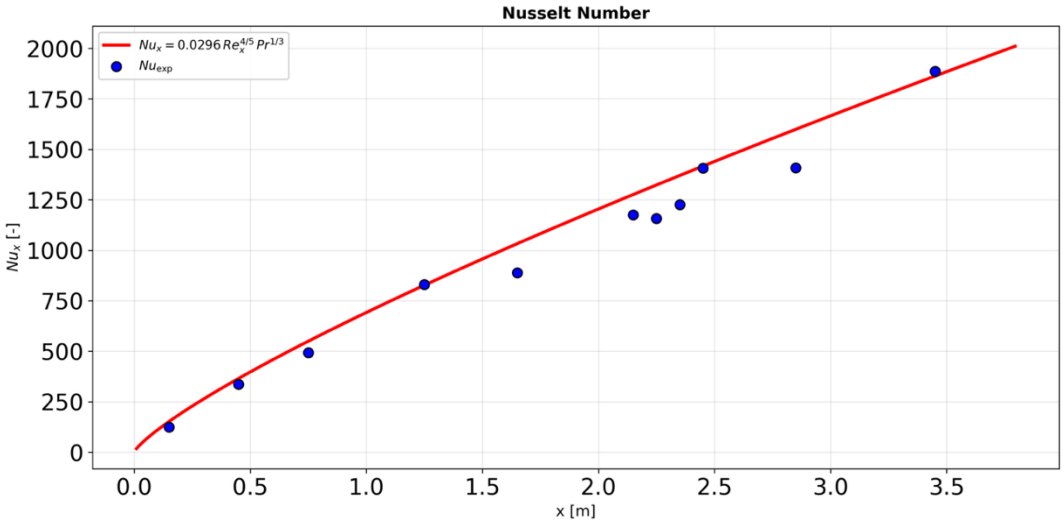

Figure 32: comparison between theoretical Nusselt number and experimental Nusselt number for the reference case

As depicted in Figure 32, the experimental Nusselt number accurately replicates the theoretical trend, confirming that the boundary layer development over the heated rotating panel in the wind tunnel correctly follows the physics of a fully developed turbulent flow. Following the validation of the dimensionless parameters, the second step focuses on the local convective heat transfer coefficient, which is mathematically derived from the Nusselt number. As demonstrated previously, the Nusselt number increases proportionally to $x^{0.8}$ along the plate and, consequently, as the convective heat transfer coefficient is obtained by dividing the Nusselt number characteristic length, as seen in Equation 27, it results in being proportional to $x^{-0.2}$, thus exhibiting a natural asymptotic decay along the longitudinal coordinate, which is driven by the progressive thickening of both the thermal and velocity boundary layers along the flow direction. As these layers shrink, they act as an increasing insulating barrier, raising the thermal and viscous resistance between the heated solid surface and the cooler free-stream fluid.

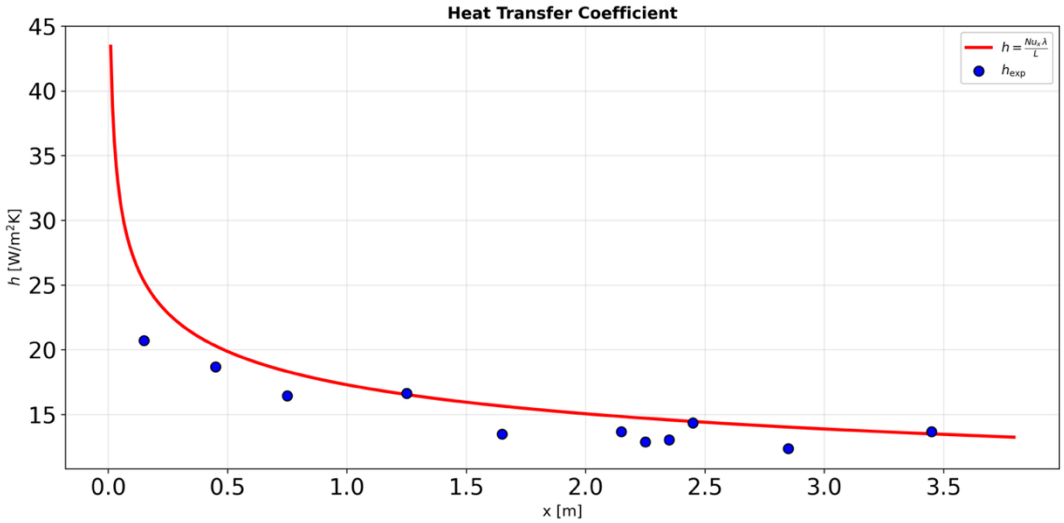

Figure 33: comparison between theoretical heat transfer coefficient and the heat transfer coefficient for the reference case

As shown in Figure 33, the experimental measurements capture this characteristic asymptotic decay perfectly, aligning with the theoretical analytical curve and thus confirming the reliability of the reference case.

4.1.2 Experimental validation of the CFD reference case

Following the theoretical validation of the experimental setup, the empirical results are utilized as the benchmark to validate the bidimensional CFD numerical model of the empty domain, which serve as reference case for the simulations' data. For the numerical simulations, to be considered valid, it must accurately reproduce the spatial distribution of the convective heat transfer coefficient observed in the wind tunnel.

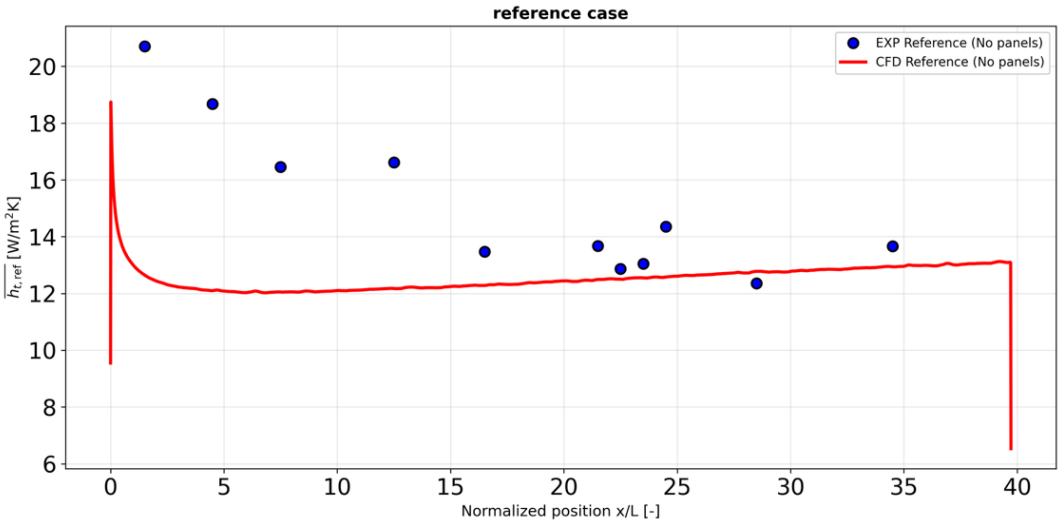

Figure 34: reference case comparison for experimental case and numerical simulations case

As shown in Figure 34, the CFD reference case successfully captures the macroscopic physical behaviour of the flow over the flat plate, as its curve exhibits the same behaviour and similar values compared to the experimental reference case. In fact, a peak is present exactly at the leading edge, which is physically consistent as at that point the free stream impacts the plate, thus the thickness of the boundary layers is theoretically zero, resulting in zero thermal resistance and maximum heat transfer. And downstream, the CFD model correctly replicates the asymptotic decay of the coefficient, aligning with the experimental values, as the boundary layer shrinks. While a slight underestimation of the absolute values can be noticed in the central region of the domain, the overall trend and the stabilization value are correctly simulated, thus considering validated the theoretical decay and the numerical baseline, this CFD reference case can be reliably used as the normalization denominator to isolate and quantify the aerodynamic perturbations introduced by the solar panels in the subsequent analyses.

4.2 Heat transfer coefficient

To evaluate the thermal impact of the agrivoltaic arrays, the local convective heat transfer coefficient between the air beneath the panels and the ground is normalized against the validated reference case of the flat plate. This ratio, expressed as a percentage, is plotted along the longitudinal coordinate normalized by the row spacing of the baseline configuration, which is *10 cm* and *7.3 m* for the wind tunnel experiments and for the numerical models respectively. This choice was made to visually maintain a directly comparable spatial scale across all graphs, regardless of the geometric variations of the specific configuration being analysed. Specifically, a value of the normalized convective heat transfer coefficient greater than 100% indicates that the presence of the panels enhances the local heat transfer compared to a flat plate, while a value below 100% indicates a thermal shielding effect produced by the panels and, consequently, a reduction in the heat exchange. The analysis is structured in two phases where, firstly, an evaluation of the physical behaviour dictated by the experimental measurements across the three configurations is conducted and, subsequently, an assessment of the accuracy of the 2D CFD numerical models in replicating these phenomena is explored.

4.2.1 Experimental evaluation of the convective heat transfer coefficient

The experimental data immediately reveal that the presence of the photovoltaic modules fundamentally alters the boundary layer development and instead of a continuous asymptotic decay, the normalized heat transfer coefficient stabilizes at distinct values depending on the specific array geometry.

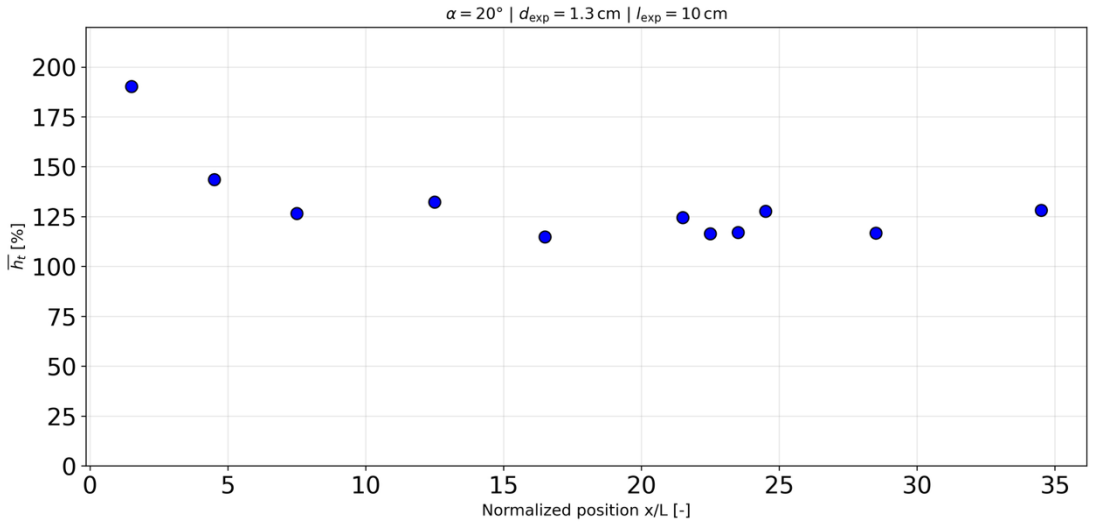

Figure 35: Normalized convective heat transfer along the normalized longitudinal position, Configuration 1

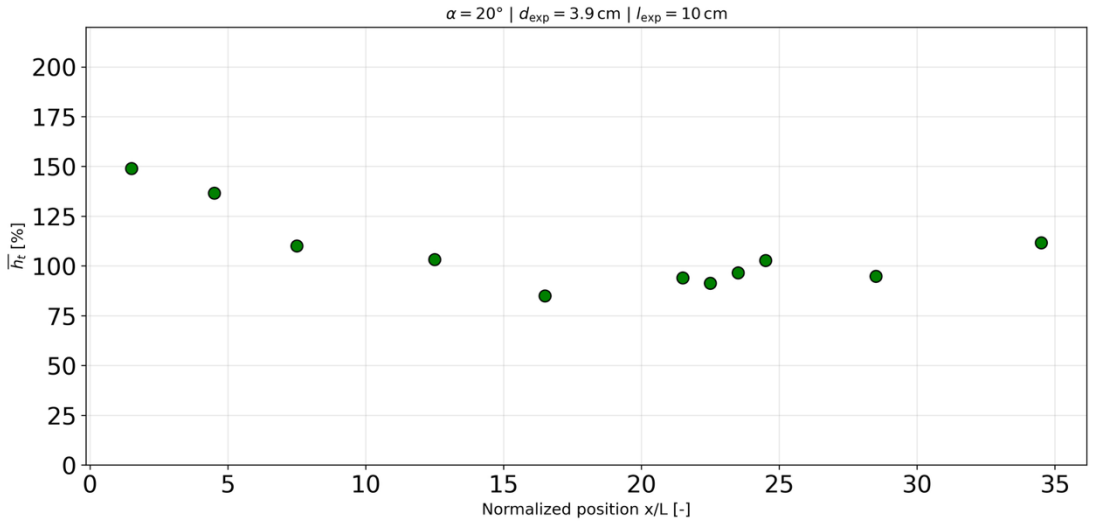

Figure 36: Normalized convective heat transfer along the normalized longitudinal position, Configuration 2

Comparing the experimental base line configuration (blue scattered values), which is the first one, with a ground clearance of *1.3 cm* and a row spacing of *10 cm*, with Configuration 2 (green scattered values), which is the one with an increment in the ground clearance, that was tripled, serves to highlight the effect of the enhancement of the height of the panel. In particular, the first configuration, which has the lowest ground clearance, presents an expected descendant trend, with experimental values stabilizing around 125%, thus showing an enhancement of 25% circa of the local convective heat transfer value in the stabilized part of the curve. In fact, the narrow gap between the

tilted panel and the ground acts as an aerodynamic nozzle, locally accelerating the flow and channelling air directly against the surface, thereby maximizing convective cooling. Conversely, in the second configuration, when the height is tripled, the experimental values drop slightly, stabilizing around 90% up to 110%, showing that increased clearance reduces this localized forced acceleration, allowing the flow to expand and slow down beneath the panels and, consequently, reducing the convective heat transfer, which physically translates into a limitation of soil evapotranspiration and better moisture conservation.

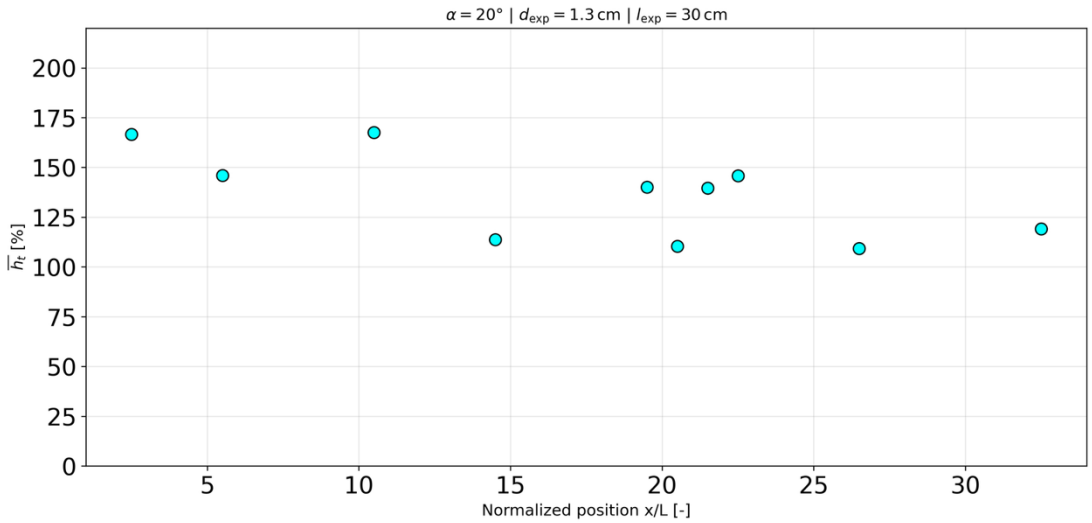

Figure 37: Normalized convective heat transfer along the normalized longitudinal position, Configuration 3

The impact of the row spacing is studied by comparing Configuration 1 with Configuration 3 (cyan scattered values), which has triple distance between the rows, with a value of *30 cm*. The convective heat transfer coefficient, for the third configuration, experiences a drastic increase, with localized experimental values highly scattered but reaching values around 120% up to 150% in the stabilized part of the curve. In fact, the wider gap prevents the panels from acting as a continuous aerodynamic canopy shielding the flow, allowing the turbulent wake to fully develop and letting the free-stream air to penetrate between the rows, thus increasing the convective heat transfer and the cooling of the ground, as higher normalized convective heat transfer coefficient corresponds to higher temperature between the ground and

the air above, as expressed in Equation 59. To visually synthesize what has been discussed so far, Figure 38 encompasses the direct comparison of the trend of the normalized convective heat transfer coefficient for the three experimental configurations tested in the wind tunnel. The graph clearly shows how the variation of geometric parameters modulates the thermo-fluid dynamic environment at ground level in different ways, defining the trade-off between the system's electrical and agricultural performance. The analysis highlights that Configuration 3, characterized by a greater row spacing, exhibits the highest values of the heat transfer coefficient. In this scenario, the deep penetration of free air favours intense turbulent mixing, resulting in maximum convective cooling, which is an optimal condition for lowering the operating temperatures of the photovoltaic modules. In contrast, Configuration 2, while maintaining standard spacing, increases the ground clearance, shifting the turbulence genesis to higher altitudes and slowing down the airflow in contact with the ground, leading to a marked overall decrease. Due to the Chilton-Colburn analogy, this reduction in heat exchange limits the air's ability to remove moisture, favouring lower evapotranspiration and subsequent water savings compared to the other configurations. Configuration 1 occupies an intermediate position, representing a more compact arrangement where the combined effect of wind and turbulence is less pronounced than in the wide spacing but more incisive than in the raised configuration.

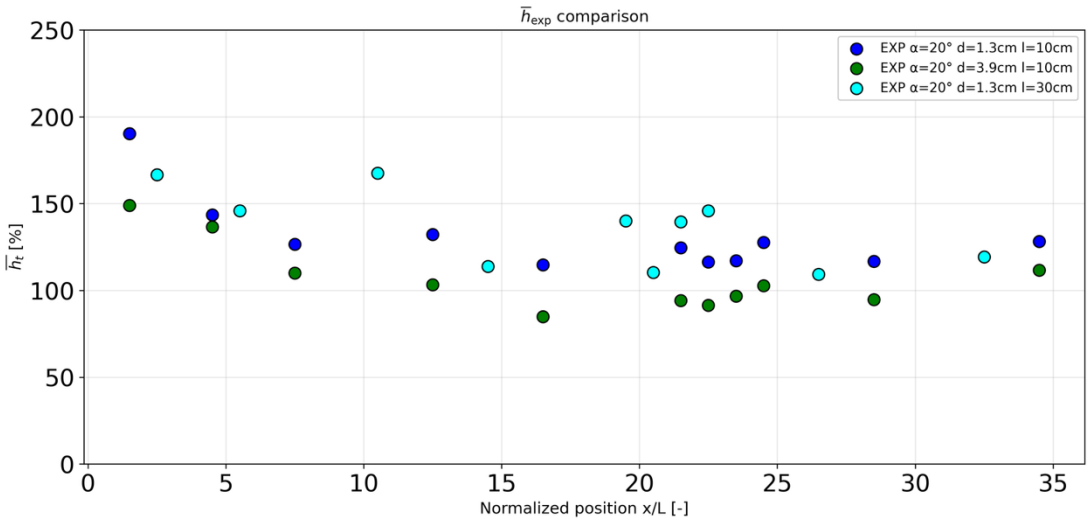

Figure 38: normalized convective heat transfer coefficient comparison for experimental data

4.2.2 CFD results comparison

To evaluate the performance of the 2D CFD simulations in replicating the heat transfer phenomena, the experimental data points (the scattered values), are directly overlaid with the continuous numerical results (the continuous lines) for each configuration.

4.2.2.1 Comparison for Configuration 1

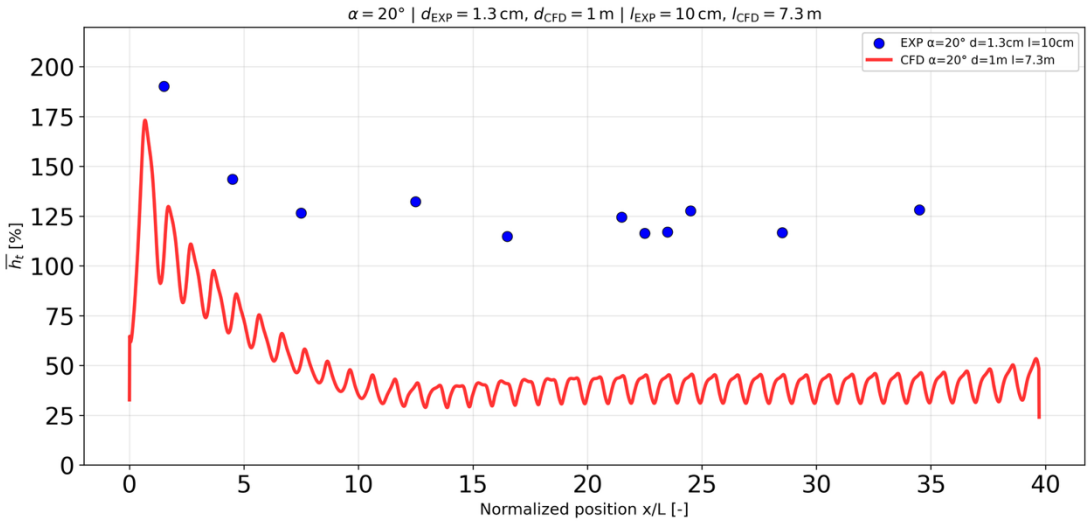

Figure 39: Direct comparison of the normalized convective heat transfer coefficient for Configuration 1. The red continuous line represents the 2D CFD numerical simulation, while the blue dots represent the wind tunnel experimental data

As shown in Figure 39, the numerical curve for Configuration 1 exhibits a oscillating pattern and this cyclic behaviour is the result of two opposing phenomena. Firstly, the gap between the tilted panel and the ground acts as a converging narrow channel, accelerating the flow and causing a positive peak in the convective heat transfer coefficient. But, immediately after, the panel acts as an obstacle, generating an extensive recirculation wake that drastically decelerates the velocity field, increasing thermal resistance and forming the descendent peaks of the curve. While the CFD simulation predicts a severe shielding effect, with the normalized convective heat transfer coefficient dropping and stabilizing in the range of 30% up to 50%, thus reducing compared to the reference case of the flat plate, the experimental blue dots completely contradict this numerical drop, showing enhanced values of $\overline{h_t}$ that reach peaks of 130%.

4.2.2.2 Comparison for Configuration 2

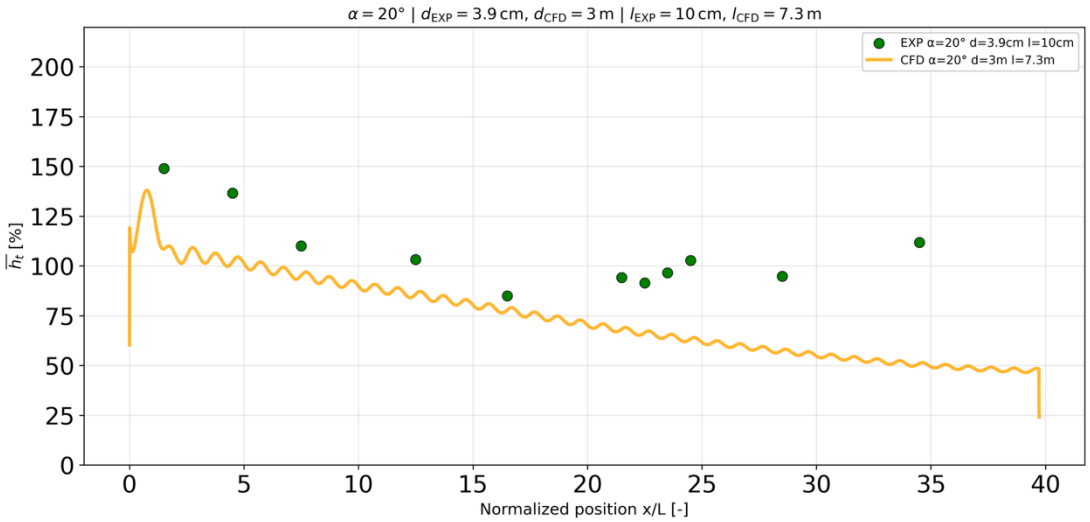

Figure 40: Direct comparison of the normalized convective heat transfer coefficient for Configuration 2. The yellow continuous line represents the 2D CFD numerical simulation, while the green dots represent the wind tunnel experimental data

Figure 40 illustrates the direct comparison for Configuration 2, highlighting the effect of the increased ground clearance. The CFD curve for the highest spatial development results in lower convective heat transfer peaks beneath the panels. But it induces a substantial delay in the onset of a stable periodic regime and, consequently, the curve fails to reach convergence within the simulated domain length, exhibiting a continuous downward trend. The experimental green dots, as previously discussed, accurately capture a slight reduction in heat transfer compared to Configuration 1 but, once again, they stand massively higher than the numerical prediction, which seems to reach values below 50%. This CFD behaviour highlights an additional discrepancy regarding the thermodynamic role of the ground clearance. In fact, in the 2D numerical case, the panel height has a marginal effect on the $\overline{h_t}$ at steady state, as it is not reached, acting almost exclusively on the spatial delay of the transient region. However, the experimental data physically contradict this numerical assumption. In the experimental case, increasing the ground clearance reduces the aerodynamic nozzle effect near the ground, allowing the boundary layer to thicken, resulting in a reduction of the local convective heat transfer. By exploiting the heat and mass transfer analogy, this drop in convective cooling

physically translates into a direct limitation of the soil evapotranspiration rate, ultimately favouring moisture retention at the ground level. This discrepancy demonstrates that the 2D steady RANS approach struggles to resolve the fully developed turbulent mixing and capturing the near-ground behaviour, not being able to appreciate the impact on the soil moisture of the agrivoltaic panel's elevation.

4.2.2.3 Comparison for Configuration 3

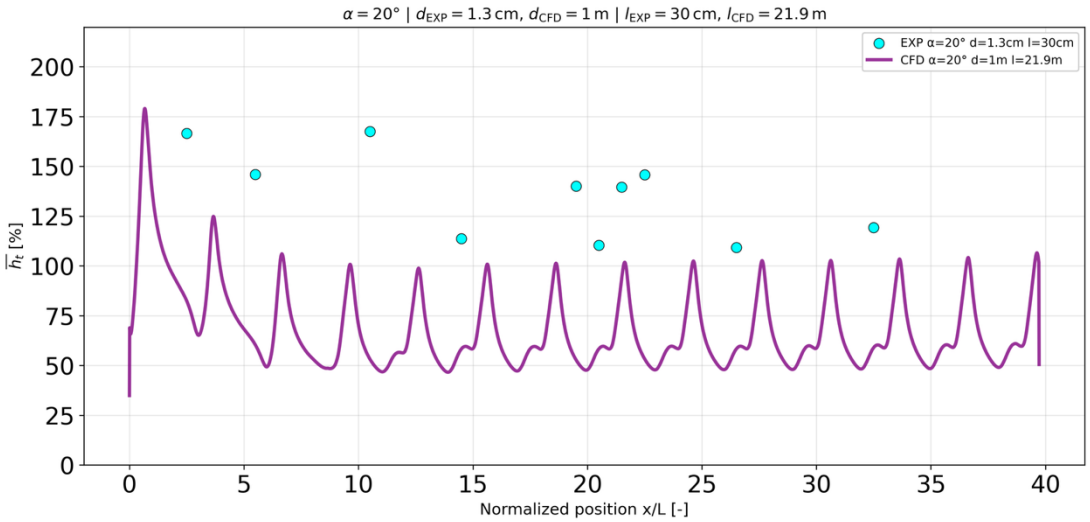

Figure 41: Direct comparison of the normalized convective heat transfer coefficient for Configuration 3. The yellow continuous line represents the 2D CFD numerical simulation, while the cyan dots represent the wind tunnel experimental data

The impact of a wider spacing between the agrivoltaic systems' rows of panels is directly compared in Figure 41. Regarding this third configuration, the elevated distance between the rows induces an enormous fluctuation in the numerical values of the convective heat transfer coefficient showing that row spacing combined with low ground clearance triggers the highest oscillation amplitude. From a fluid-dynamic perspective, the wider row spacing provides sufficient spatial length for the aerodynamic wake to fully develop and for the flow to recover its free-stream velocity before encountering the subsequent row. This velocity recovery leads to a thinning of the boundary layer, inducing a reduction in the thermal resistance, and allowing cooler air to reach the ground. The continuous replacement of stagnant air with fresh free-

stream flow significantly reduces the local temperature differential between the ground and the fluid, and this effect translates to an enhanced normalized convective heat transfer coefficient. Consequently, the configuration presents a higher overall convective heat transfer compared to the baseline system, a trend that is perfectly in line with the enhanced cooling behaviour observed in the experimental wind tunnel tests. But, as shown in the previous comparison, the numerical 2D simulation underestimate the heat transfer respect to experimental case, resulting in a lower $\overline{h_t}$. Furthermore, when comparing numerical values with experimental values, specific methodology used for data acquisition must be considered. As detailed in the methodology, the experimental values were obtained from fluxmeters that measured the total average heat flux, from which the radiative component was subtracted to isolate the convective flux and calculate the convective heat transfer coefficient. Due to the geometric constraints of the scaled agrivoltaic model, and by choosing the transversal coordinate with the highest density of fluxmeters, these sensors were predominantly located in the open spaces between two consecutive rows of panels. From a thermo-fluid dynamic perspective, these inter-row gaps correspond, because the panels act as wind shields and the velocity boundary layer gets thicker, to the region with the maximum local temperature differential between the ground and the air. According to Newton's law of cooling, a higher temperature differential causes a lower local convective heat transfer coefficient (as described in Equation 59). Therefore, the experimental scattered points logically capture the physical minimums of the real thermal field, which in the CFD curves correspond to the vertexes of the negative spikes. In summary, the experimental cases predominantly capture the physical minimums of the convective heat transfer coefficient within the inter-row gaps. While, the CFD cases exhibit a characteristic oscillating trend, as the physical presence of the panels locally concentrates the turbulence, thereby enhancing the heat transfer directly underneath the modules. However, evident discrepancies exist between the two datasets, with the CFD simulations underestimating the overall magnitude of the heat exchange in all the configurations compared to the experiments. This mismatch could be explained considering that the 2D numerical simulations attempt to replicate a three-dimensional

wind tunnel experiment, assuming an idealized geometry that could underestimate the aerodynamic effects of the real physical structure, which is significantly more complex. Elements such as support frames, electrical cables, and the measurement instrumentation itself are inevitably present in the wind tunnel but absent in the CFD domain. In a real scenario, these physical elements act as additional obstacles that could generate localized 3D turbulence, flow separation, and lateral mixing, all of which might contribute to enhancing the actual convective heat transfer. To investigate this difference, the next step is to examine the variations occurring across different aerodynamic parameters

4.3 Velocity of the wind evaluation

To comprehensively understand the thermal behaviour of the agrivoltaic system, the first step is to investigate the aerodynamic field by analysing the mean velocity components. In fact, the convective heat transfer is strictly dependent on the fluid velocity, a relationship mathematically governed by the Reynolds number, which is directly dependent on the longitudinal velocity component as shown in Equation 26. Thus, the evaluation of $\vec{u}$ is essential to verify the consistency of the normalized convective heat transfer coefficient and to assess the coherence between the experimental data and the CFD results. Furthermore, both the longitudinal and vertical mean velocity components must be evaluated to map the macroscopic transport of the air masses and identifying the regions characterized by the most intense advection, which is fundamental to comprehend how the fluid is channelled or deflected by the panels. Finally, the analysis of the mean velocity profiles serves as a necessary preliminary step to introduce the turbulent kinetic energy, which is experimentally defined by the standard deviation of the velocity around these mean values, as described previously with Equation 57. The dimensionless velocity profiles are extracted in the region where the normalized heat transfer coefficient is stable, which means around the 15th panel for the configurations with minor row spacing (Configurations 1 and 2) and around the 5th panel for the configuration with major row spacing

(Configuration 3) and, as described in the methodology, the profiles are evaluated at the same strategic longitudinal locations to track the flow evolution around the module, which are the upstream of the inter-row gap position, just before the leading edge, and immediately after the trailing edge. To ensure a coherent comparison between the PIV experimental measurements and the 2D CFD simulations, both the spatial coordinates and the velocity components have been normalized. The *y*-coordinate is normalized by the ground clearance of the baseline configuration (Configuration 1), while the longitudinal and vertical velocities are normalized by the magnitude of the undisturbed free-stream velocity, which is $5\ \frac{m}{s}$. The analysis proceeds by comparing the dimensionless velocity profiles for both experiments and CFD simulations across the three configurations, analysing the discrepancies.

4.3.1 Analysis of the experimental velocity field

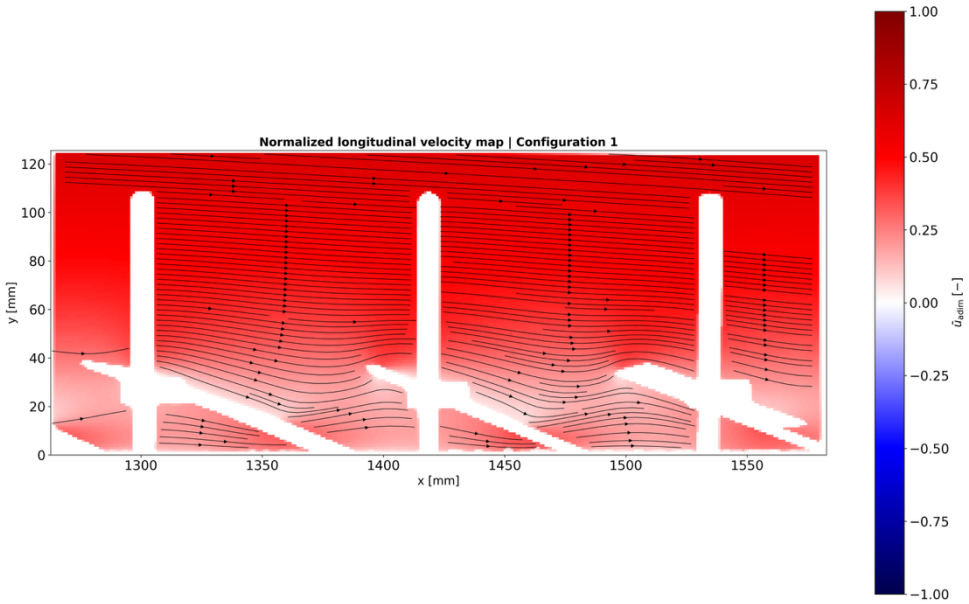

Figure 42: Normalized u distribution around the panel with stable $\bar{h}_t$, Configuration 1

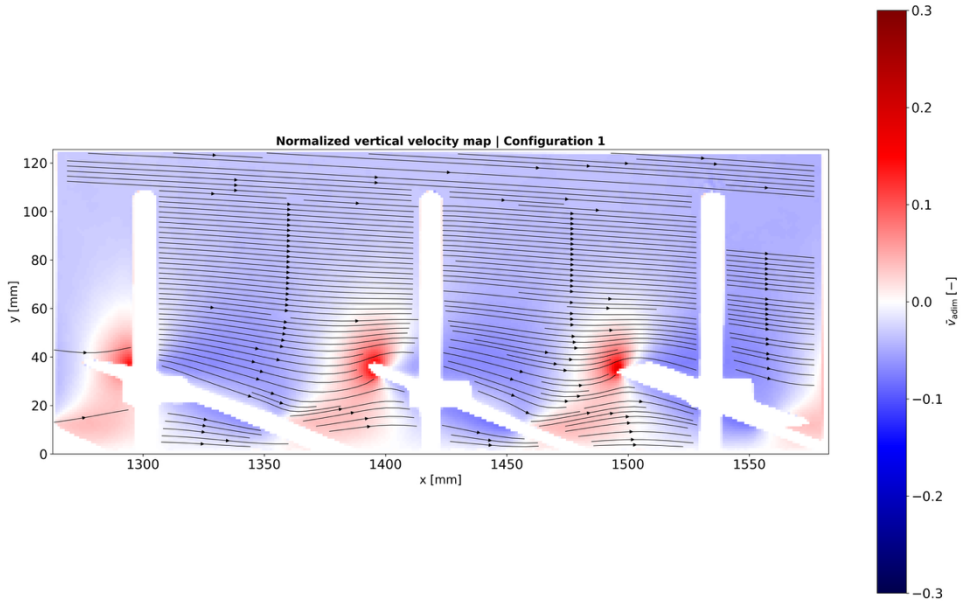

Figure 43: Normalized v distribution around the panel with stable $\overline{h_t}$, Configuration 1

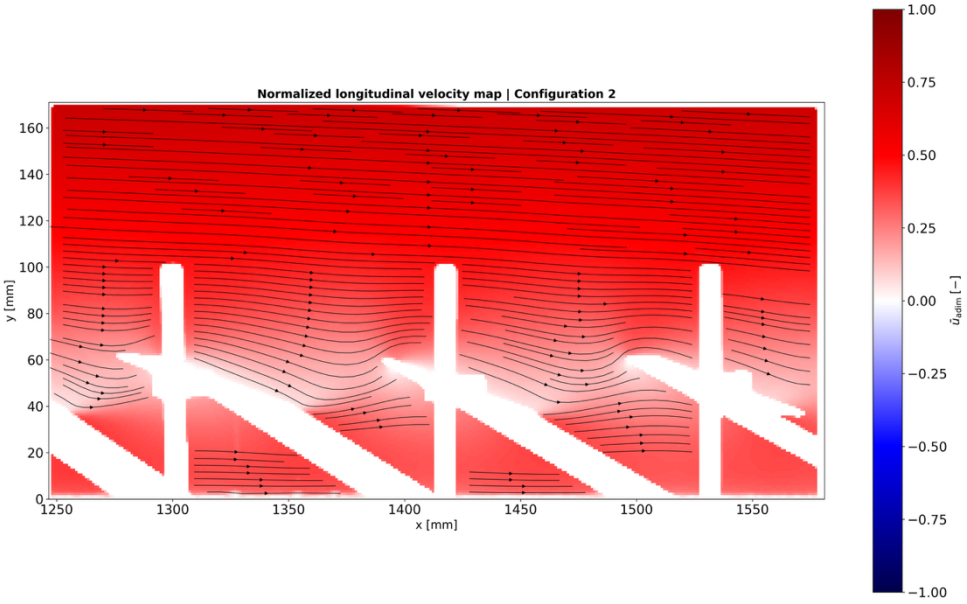

Figure 44: Normalized u distribution around the panel with stable $\overline{h_t}$, Configuration 2

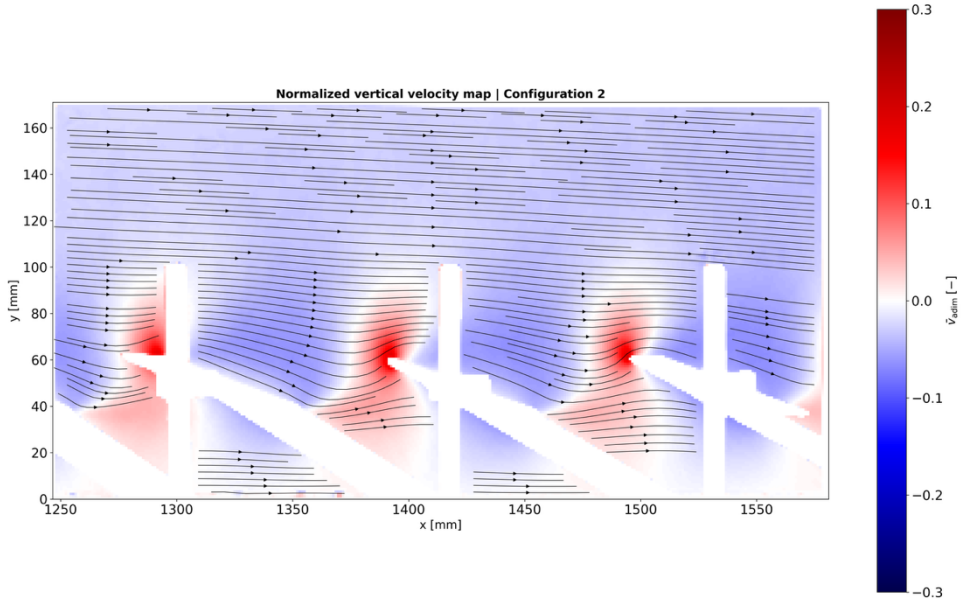

Figure 45: Normalized v distribution around the panel with stable $\overline{h_t}$, Configuration 2

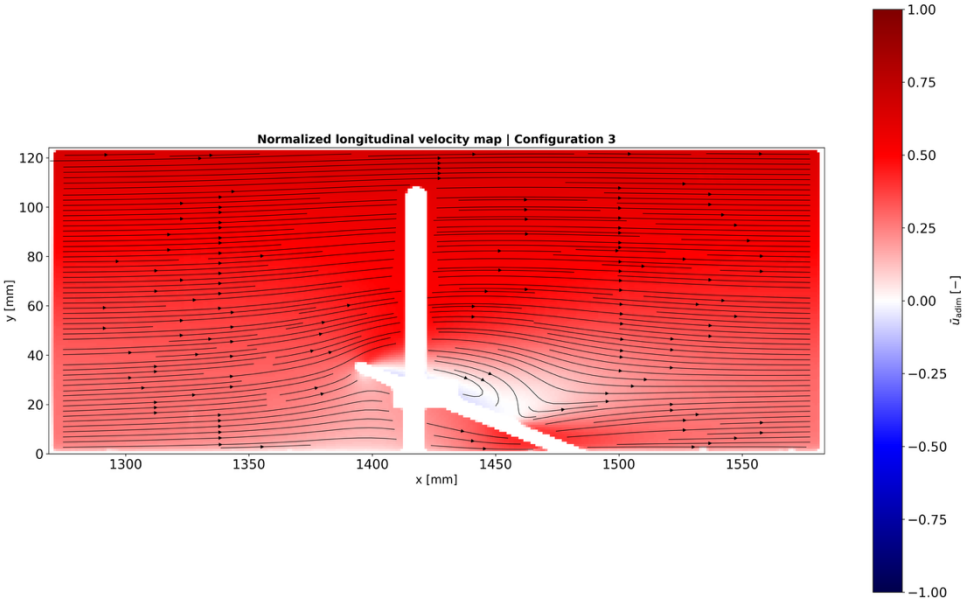

Figure 46: Normalized u distribution around the panel with stable $\overline{h_t}$, Configuration 3

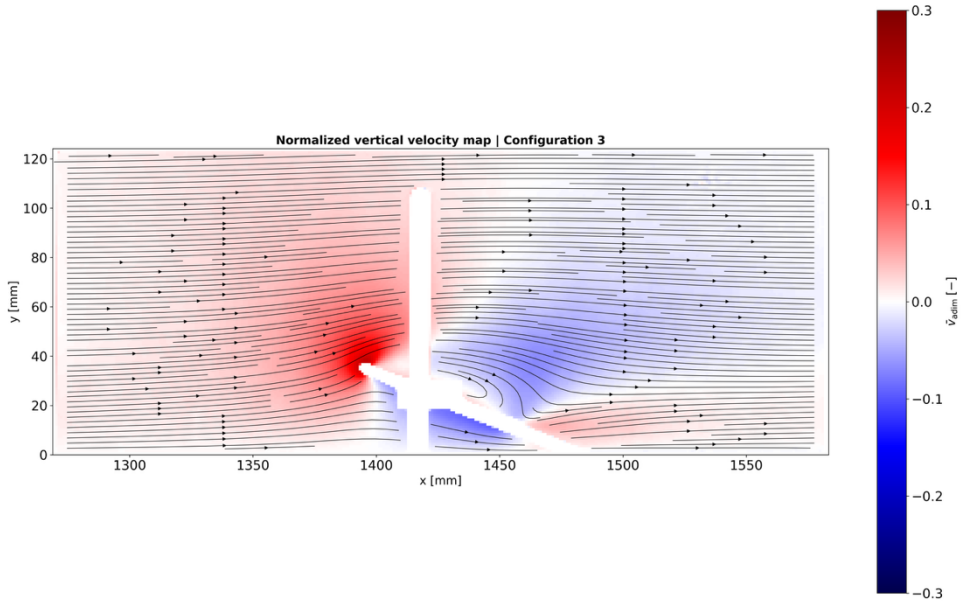

Figure 47: Normalized v distribution around the panel with stable $\overline{h_t}$, Configuration 3

These maps are a useful tool to visualize the concentration of the velocity components in each region of the agrivoltaic panel analysed. Furthermore, the streamlines, provide an idea of the motion of the fluid, by detecting the eddies formation and the fluid deflection caused by the agrivoltaic system presence. Regarding the baseline layout (Configuration 1), the normalized longitudinal velocity map shows slightly lower values compared to the others, as the proximity to the ground doesn't let the mean velocity, whose trend is logarithmic, to reach higher values. Furthermore, due to the short distance between rows, the velocity gets influenced by the triggering each row of panels exerts on the successive one, while the free-stream fluid has no space to deeply penetrate in the gap region. In the map (Figure 42), a distinct region of high-velocity fluid is visible at the leading and trailing edges of the panels, visually confirming the localized aerodynamic nozzle effect. Meanwhile, a deep low-velocity wake plume is generated downstream of the module, and, due to the compact row spacing, this region with low momentum extends uninterrupted towards the successive panel, demonstrating how the normalized u suffers a continuous deceleration after the leading edge and acceleration at the successive panel's leading edge. The normalized vertical velocity map further clarifies the flow deflection, with a sharp, localized updraft visible exactly at the

leading edge and at the trailing edge, while a broader downdraft region dominates the area just above the panels, meaning that the cold free-stream fluid try to flow towards the gap, while the heated fluid in gap tries to go upwards to be substituted. The superimposed streamlines help detect the formation of recirculation vortices trapped within the narrow inter-row gaps, as they get deflected mirroring the behaviour of the fluid velocity components. When evaluating the elevated layout (Configuration 2), the map highlights higher values of normalized *u*, due to the higher ground clearance which allows the mean velocity to reach higher values. Furthermore, in the normalized longitudinal velocity distribution, the faster sub-panel stream can vertically expand, reducing the aerodynamic nozzle effect at the ground level and thickening the boundary layer. Again, the low-velocity wake plume is still present and structurally comparable to the baseline case, although is obviously shifted to a higher position. Similarly, the normalized vertical velocity map displays the characteristic leading-edge updraft and the subsequent free-stream fluid downdraft, but these localized vertical motions develop much further away from the terrain. This visual evidence, and the fact that the channelling effect are located farer from the ground, corroborates the normalized convective heat transfer coefficient behaviour observed previously. In fact, as the macroscopic turbulent mixing is elevated, it leaves the fluid layers at ground level calmer and thus allows the thermal boundary layer to stay thick. Finally, the maps for the increased row spacing layout (Configuration 3) reveal that, for the normalized longitudinal velocity, the wider gap facilitate the penetration of the free-stream air, and in fact, even if the ground clearance is the same compared to the ground, slightly higher values of mean velocity are recorded. In fact, the low-velocity wake plume is allowed to dissipate and progressively regain momentum before encountering the subsequent row, weakening the continuous shielding effect observed in the compact configurations. Thus, the flow expansion is even more evident in the normalized vertical velocity distribution as the extended longitudinal space allows a deeper penetration of the free-stream downdraft into the inter-row gap. Without the close subsequent panel, the superimposed streamlines trace an evident behaviour shifted towards eddies formation directly behind the trailing edge, promoting the fluid mixing and enhancing the

convective heat transfer. And, in fact, the third configuration has the higher normalized convective heat transfer between the studied agrivoltaic system configurations, as previously discussed.

4.3.2 Analysis of the experimental and CFD profiles of the velocity

As visually depicted in the maps, the negative values of normalized longitudinal velocity identify the flow reversal phenomenon occurring within the recirculation area directly behind the panels. Similarly, negative values of normalized vertical velocity indicate a downward fluid motion, meaning that the free-stream fluid, which has higher momentum, is flowing towards the ground. The discrepancy that occurs between CFD values and experimental points is a necessary starting point to explain the divergency shown previously regarding the normalized convective heat transfer coefficient, as the values of $\vec{u}$ and $\vec{v}$ are strictly correlated to heat transfer phenomena.

4.3.2.1 Normalized velocity components for Configuration 1

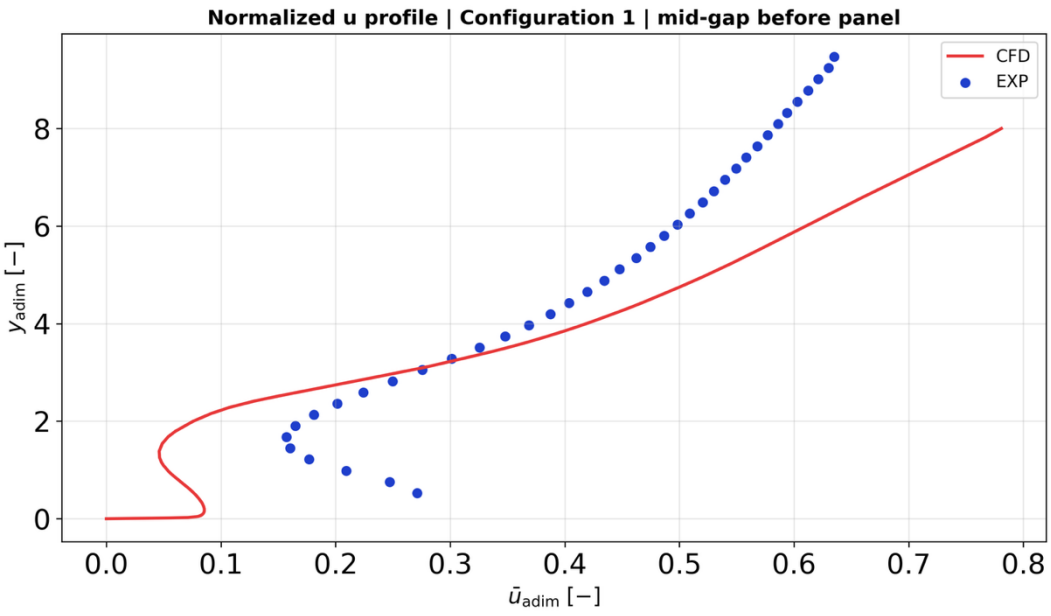

Figure 48: Profile of normalized longitudinal velocity for CFD simulations and experiments in the upstream gap between rows position, Configuration 1

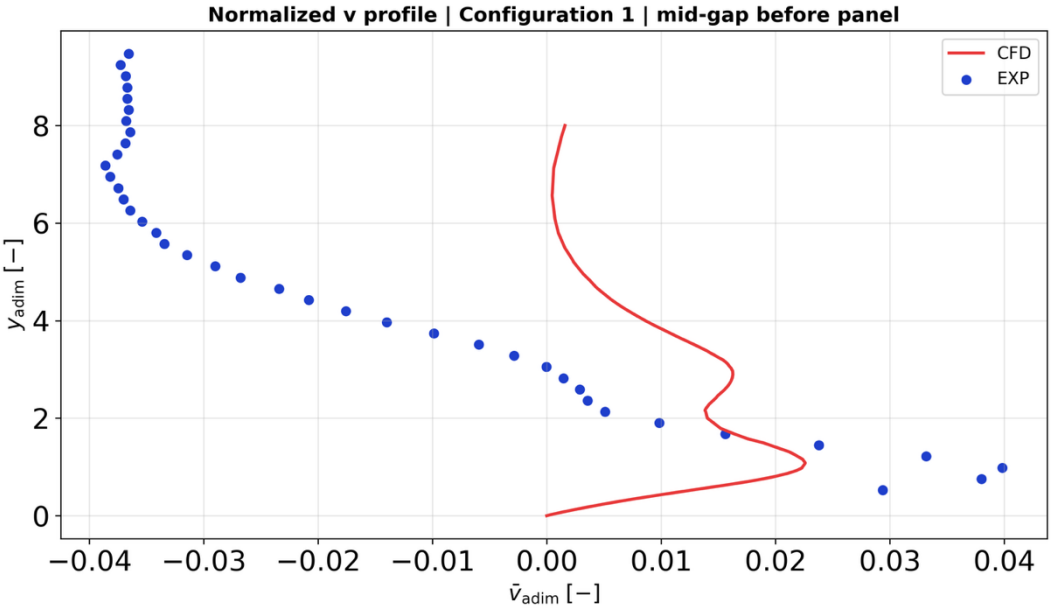

Figure 49: Profile of normalized vertical velocity for CFD simulations and experiments in the upstream gap between rows position, Configuration 1

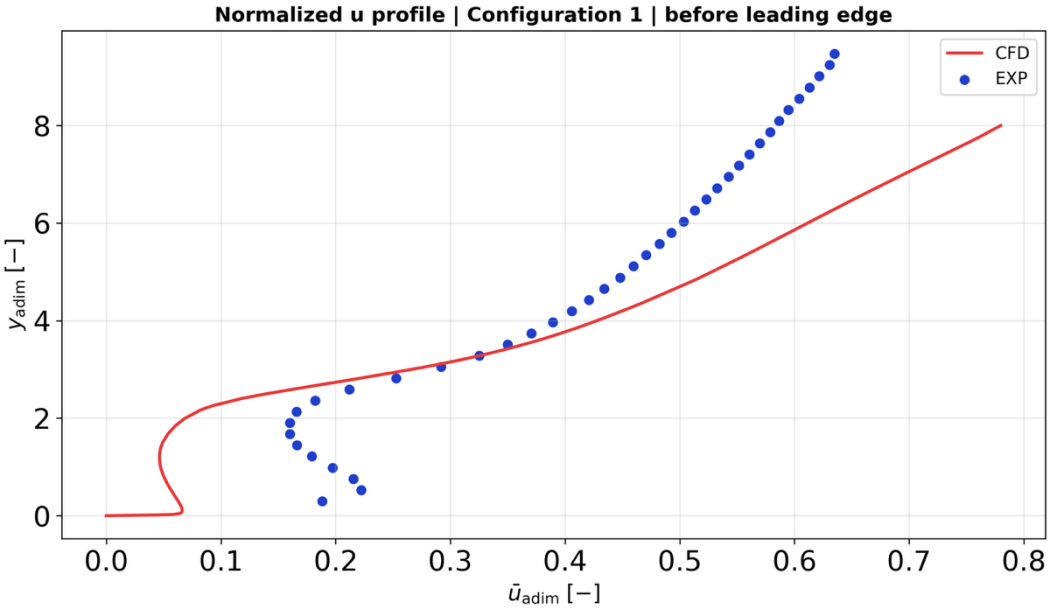

Figure 50: Profile of normalized longitudinal velocity for CFD simulations and experiments in the position before the leading edge, Configuration 1

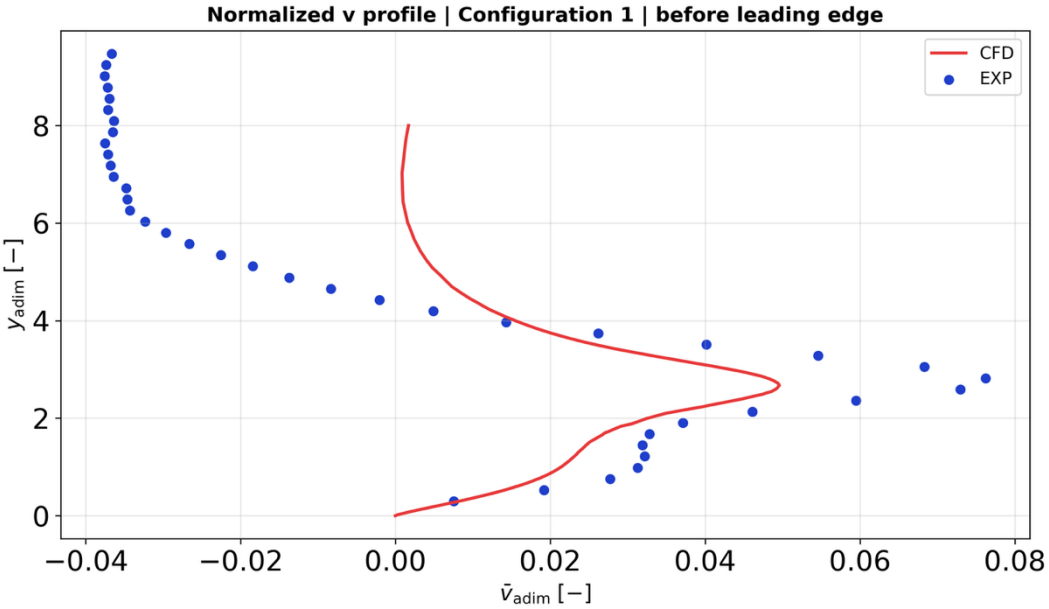

Figure 51: Profile of normalized vertical velocity for CFD simulations and experiments in the position before the leading edge, Configuration 1

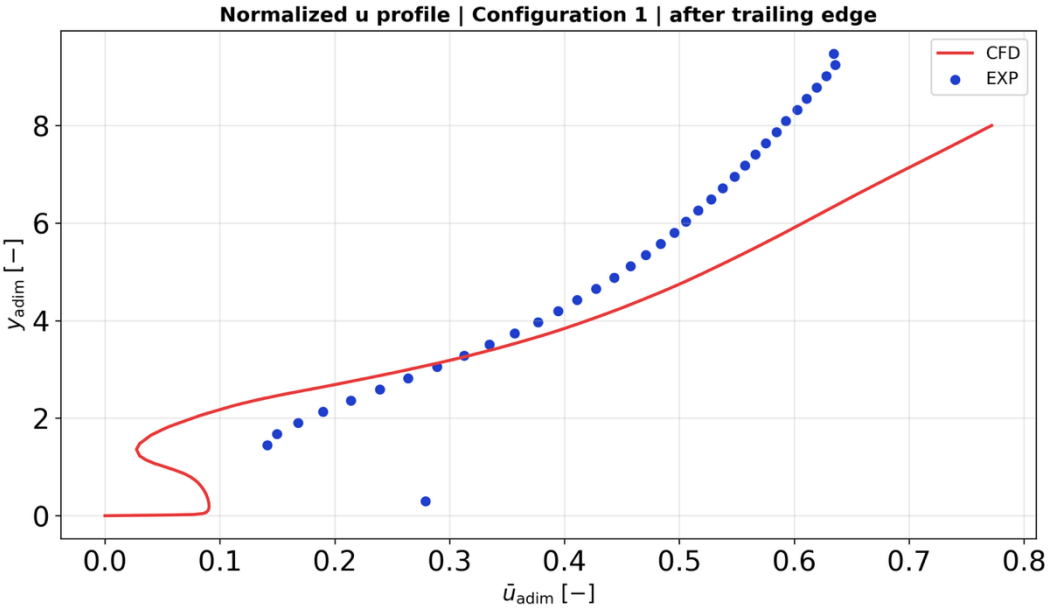

Figure 52: Profile of normalized longitudinal velocity for CFD simulations and experiments in the position after the trailing edge, Configuration 1

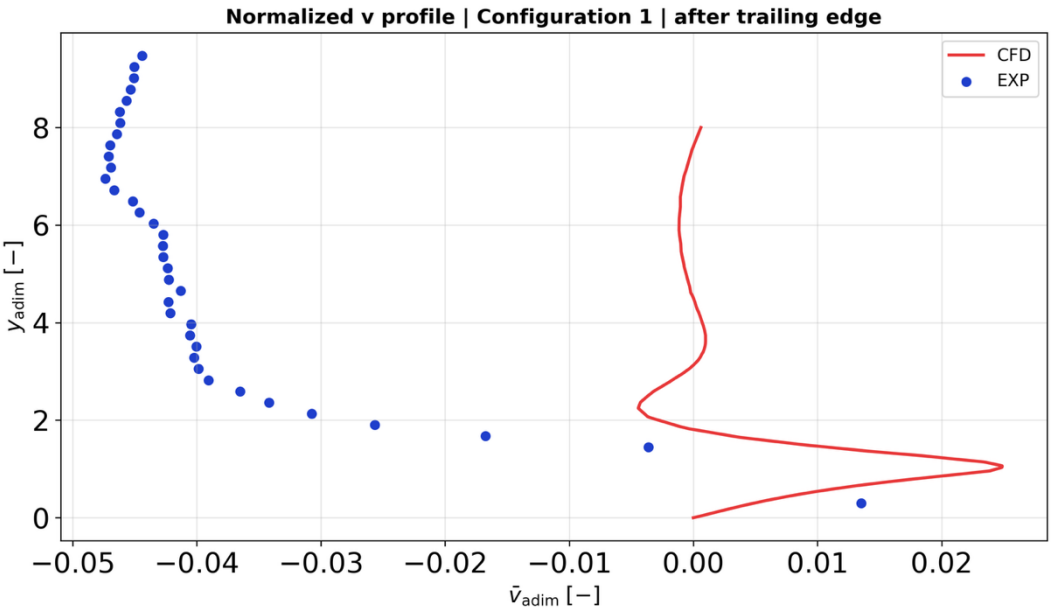

Figure 53: Profile of normalized vertical velocity for CFD simulations and experiments in the position after the trailing edge, Configuration 1

The baseline layout (Configuration 1) is characterized by compact row spacing, which induces an inevitable aerodynamic interaction between consecutive modules. Observing the experimental normalized longitudinal velocity profiles from the ground upwards, a characteristic bell-shaped trend is consistently detected across the investigated locations. This shape features a localized velocity peak near the trailing edge elevation, a pronounced velocity deficit in the region just below the leading edge, and a subsequent flow acceleration at the leading edge height that progressively homogenizes with the higher-velocity freestream fluid above. This behaviour is thoroughly corroborated by the previously analysed normalized longitudinal velocity distribution map (Figure 42). The leading edge effectively acts as an aerodynamic breakwater, accelerating the impacting fluid upwards. Conversely, the velocity deficit area is physically explained by the low-momentum wake plume generated behind the panel. Because of the compact row spacing, this plume acts as a continuous aerodynamic shield, persisting across all longitudinal positions as the consecutive modules strongly interfere with each other. Furthermore, the lower velocity peak recorded near the ground is driven by the warmer air sweeping the terrain, which accelerates and deflects upwards to be replaced by the cooler, high-momentum

freestream fluid, a dynamic clearly traced by the spatial streamlines observed in the distribution map (Figure 42). The analysis of the experimental normalized vertical velocity profiles provides further evidence of this complex mixing mechanism. At the trailing edge elevation, a distinct upward acceleration peak is recorded, as the rising air is continuously replaced by descending cooler freestream fluid. Driven by the narrow row distance, this flow directly impacts the leading edge of the subsequent panel, causing the vertical velocity peak at the leading edge to be extremely marked both in the mid-gap (Figure 49) and after the trailing edge locations (Figure 53). At the leading edge position itself (Figure 51), a strong concentration of vertical velocity is observed as the sharp edge abruptly deflects the fluid upwards, locally accelerating it and triggering a highly turbulent behaviour prone to eddy formation. However, the narrow row spacing mechanically squeezes these vortical structures, preventing the turbulent eddies from fully developing along the *x*-direction. When comparing these physical dynamics with the numerical simulations, it is evident that the shielding effect of the panel is severely exaggerated in the CFD cases. Regarding the normalized longitudinal velocity profiles, while the solver qualitatively replicates the bell-shaped curve, it computes lower velocity values within the wake plume, overestimating the flow stagnation. This shielding effect becomes even more critical when evaluating the normalized vertical velocity profiles, where the CFD model completely fails to capture the strongly negative vertical velocities recorded experimentally above the leading edge. Physically, these negative values represent the cooler freestream fluid descending to replace the rising air, generating the macroscopic turbulent mixing that promotes the convective heat transfer. Instead, the numerical model predicts basically null vertical velocities at that elevation, demonstrating a severe underestimation of the leading edge turbulence concentration and the associated downdraft. Moreover, the upward acceleration peaks at the trailing edge are similarly underestimated. In summary, the CFD simulations fail to recognize the physical tendency of the fluid to generate eddies at leading edge and enhance the turbulent mixing behind the panel. This underestimation perfectly validates the convective heat transfer coefficient comparison, providing a physical reason why the numerical curve yields significantly lower values of $\overline{h_t}$ (Figure 39).

4.3.2.2 Normalized velocity components for Configuration 2

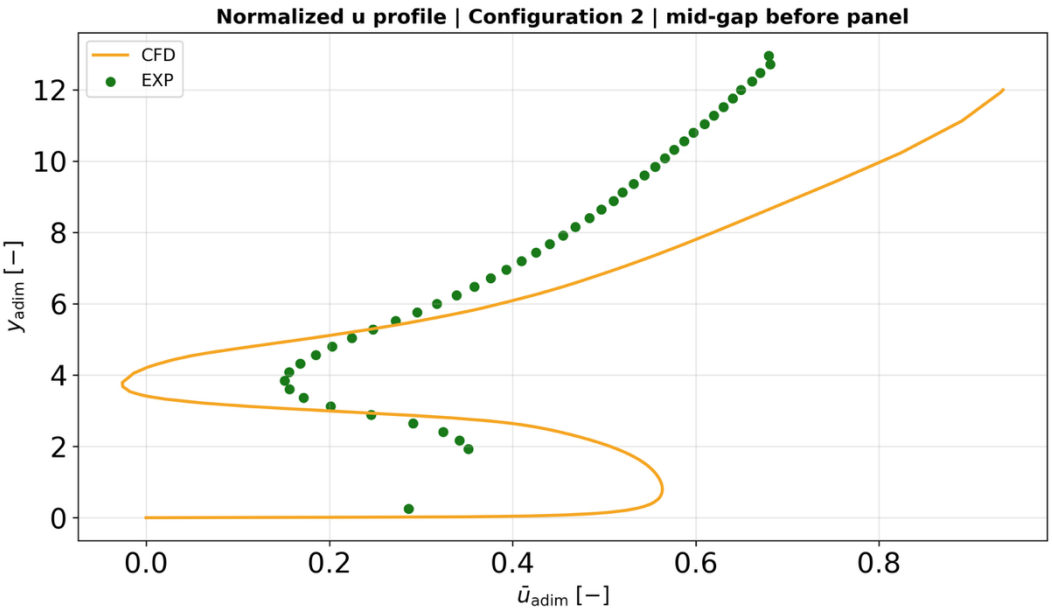

Figure 54: Profile of normalized longitudinal velocity for CFD simulations and experiments in the upstream gap between rows position, Configuration 2

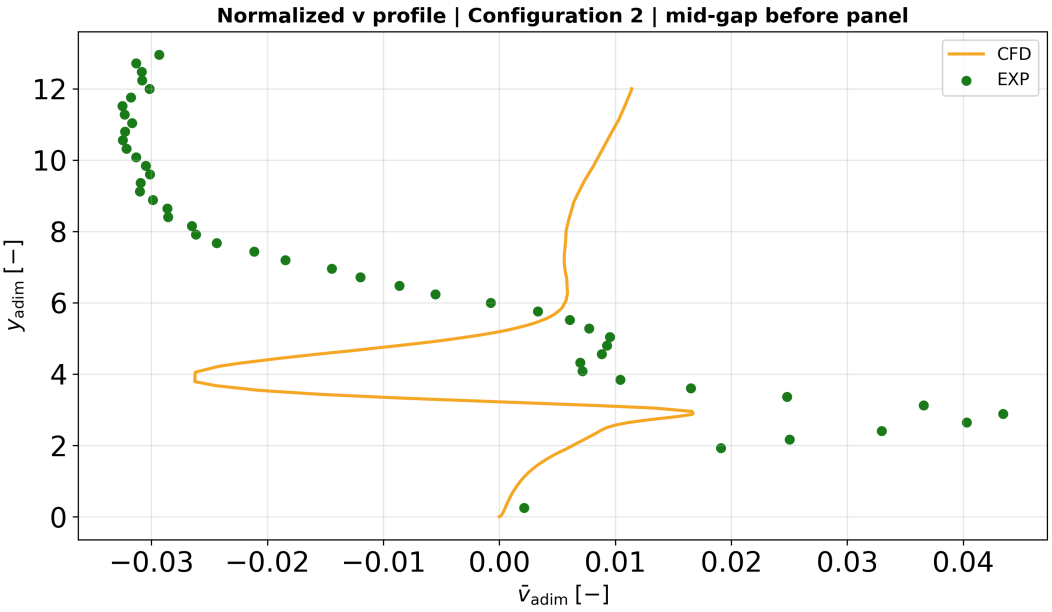

Figure 55: Profile of normalized vertical velocity for CFD simulations and experiments in the upstream gap between rows position, Configuration 2

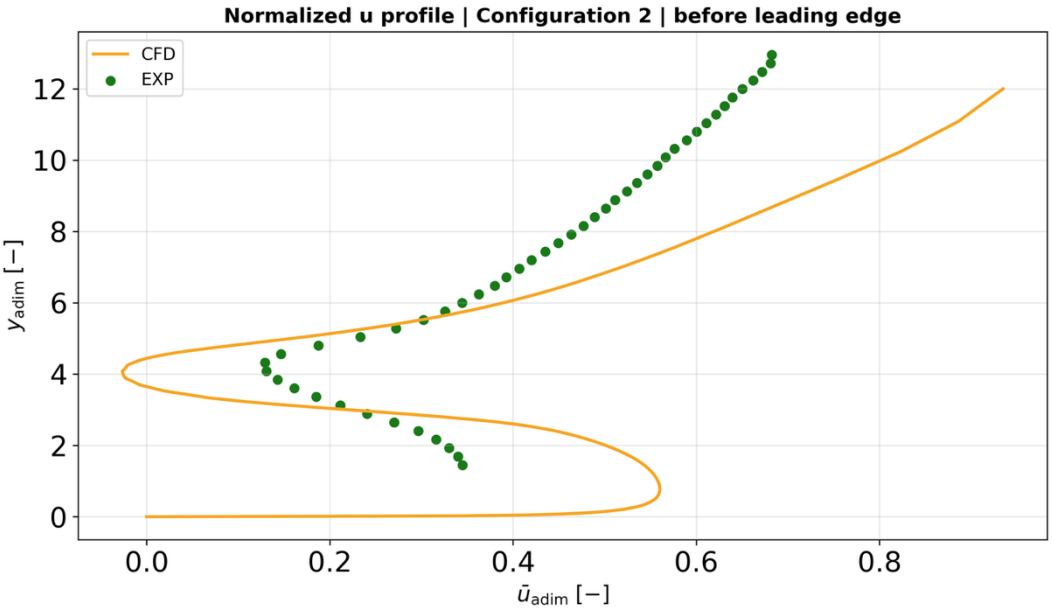

Figure 56: Profile of normalized longitudinal velocity for CFD simulations and experiments in the position before the leading edge, Configuration 2

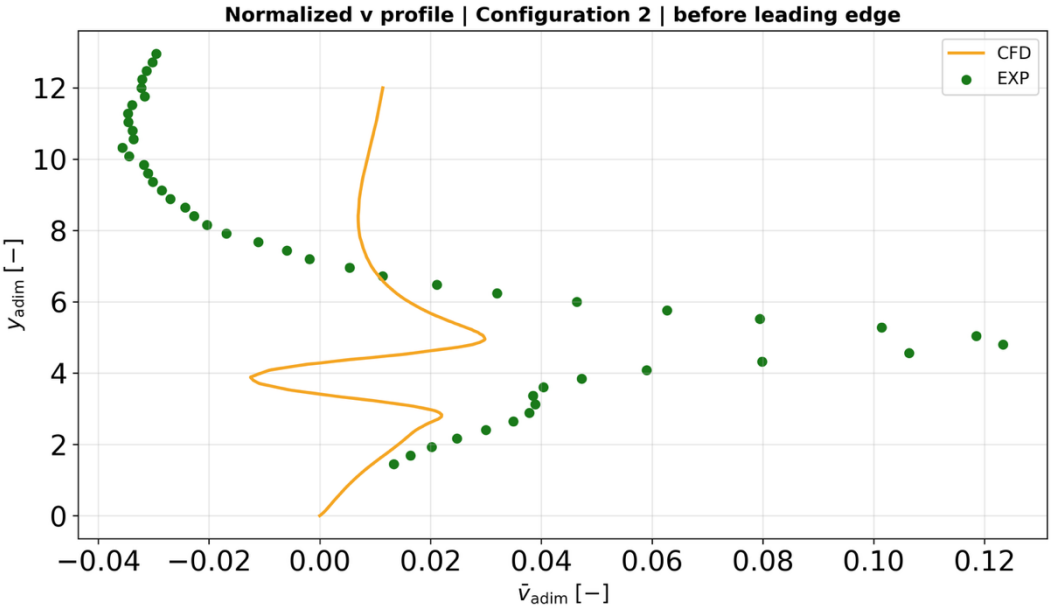

Figure 57: Profile of normalized vertical velocity for CFD simulations and experiments in the position before the leading edge, Configuration 2

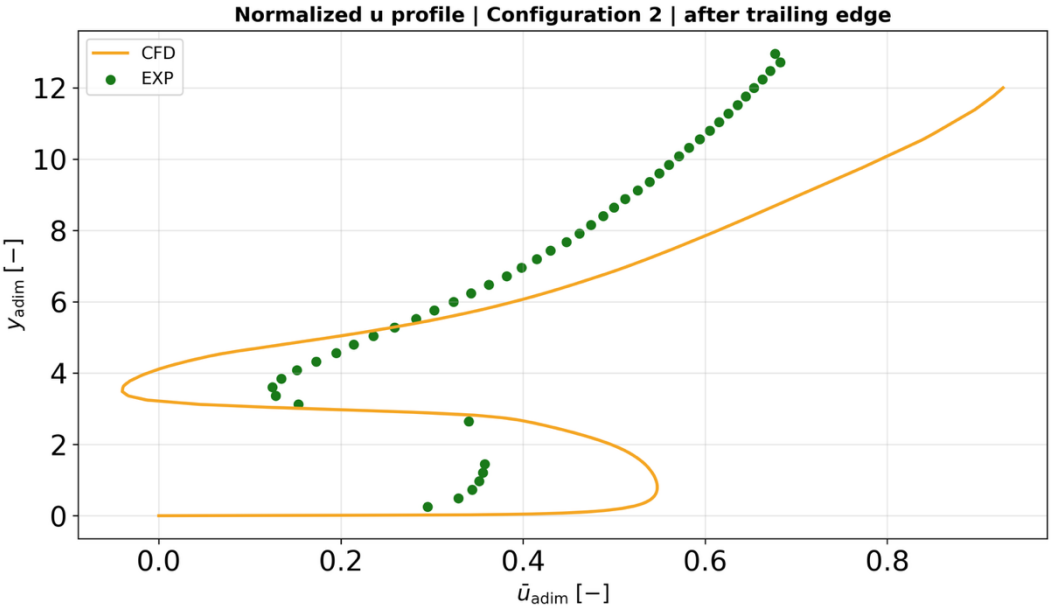

Figure 58: Profile of normalized longitudinal velocity for CFD simulations and experiments in the position after the trailing edge, Configuration 2

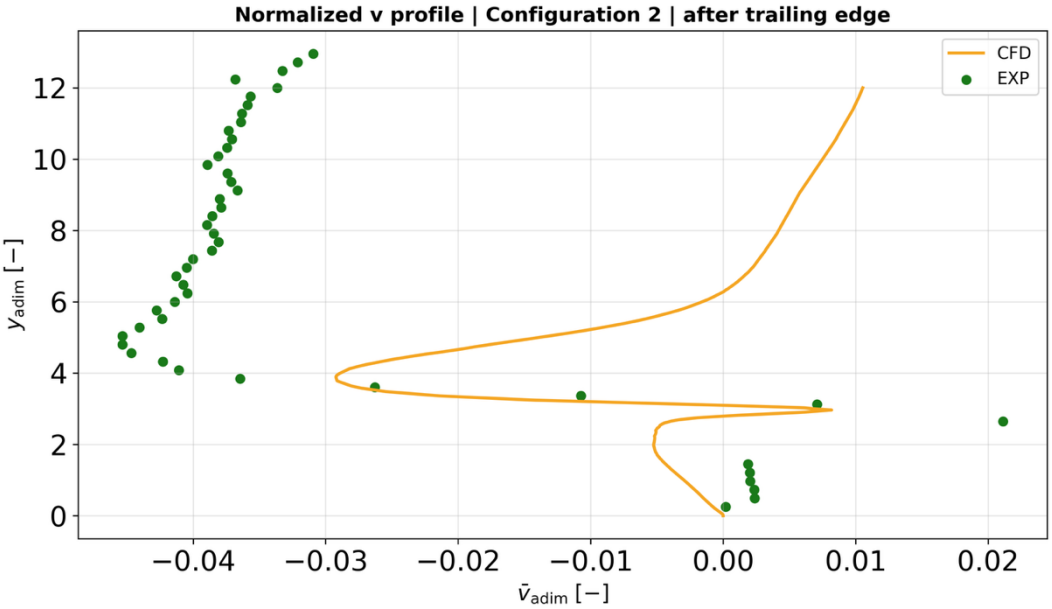

Figure 59: Profile of normalized vertical velocity for CFD simulations and experiments in the position after the trailing edge, Configuration 3

Moving to the elevated layout (Configuration 2), the system features a tripled ground clearance compared to the baseline, as explained in the methodology. Observing the experimental normalized longitudinal velocity profiles, the most prominent difference

from Configuration 1 is the broader and more energetic sub-panel flow. The increased gap effectively reduces the flow constriction near the ground, allowing a larger volume of freestream air to channel beneath the modules. Consequently, the near-ground acceleration peak is wider, and the low-velocity wake plume is geometrically shifted to higher vertical coordinates, allowing the profiles to structurally maintain the characteristic bell-shaped trend, as depicted in Figure 54, Figure 56, and Figure 58. Furthermore, the experimental normalized vertical velocity profiles confirm the persistence of the macroscopic mixing mechanism, exhibiting high values of positive vertical velocity at the leading edge elevation, as clearly seen in the leading edge profile (Figure 55). However, while the overall sub-panel flow is more voluminous, the physical distance of these aerodynamic phenomena from the ground plays a critical role in the thermal exchange. By tripling the ground clearance, the localized aerodynamic nozzle effect, which in Configuration 1 helped accelerating the flow towards the ground, is weaker. Although the velocity and vertical motion peaks are higher in magnitude, as expected given the naturally faster wind at higher elevations within the atmospheric logarithmic boundary layer (Figure 16), these turbulent structures develop farer from the soil. Consequently, the intense macroscopic mixing and the turbulent eddies fail to thin the velocity and thermal boundary layers, which are allowed to thicken along the terrain. As discussed previously, this thickened boundary layer increases the thermal resistance between the ground and the freestream fluid, providing a further explanation for why the elevated layout registers a lower ground convective heat transfer coefficient compared to the compact baseline. When comparing these dynamics with the numerical predictions, the 2D CFD simulations exhibit the exact same limitations observed for the baseline case. The numerical model continues to exaggerate the aerodynamic shielding effect of the agrivoltaic structure, computing slower longitudinal velocity values in the wake plume region and, conversely, in the lower sub-panel region, the computed values are slightly higher compared to the experimental ones. Most importantly, the solver completely fails to capture the strongly negative vertical velocities above the panels, predicting essentially near-zero values of vertical motion from the leading edge height upwards, thus neglecting the freestream fluid moving downwards. This confirms that,

despite the increased ground clearance, the CFD simulations still struggle to detect the eddy formation and the resulting downward descendance of cooler fluid mixing with the higher-temperature air above the ground. This underestimation of the macroscopic turbulent mixing provides a physical justification, as discussed for Configuration 1, for the underestimated normalized convective heat transfer coefficient computed by the software (Figure 40).

4.3.2.3 Normalized velocity components for Configuration 3

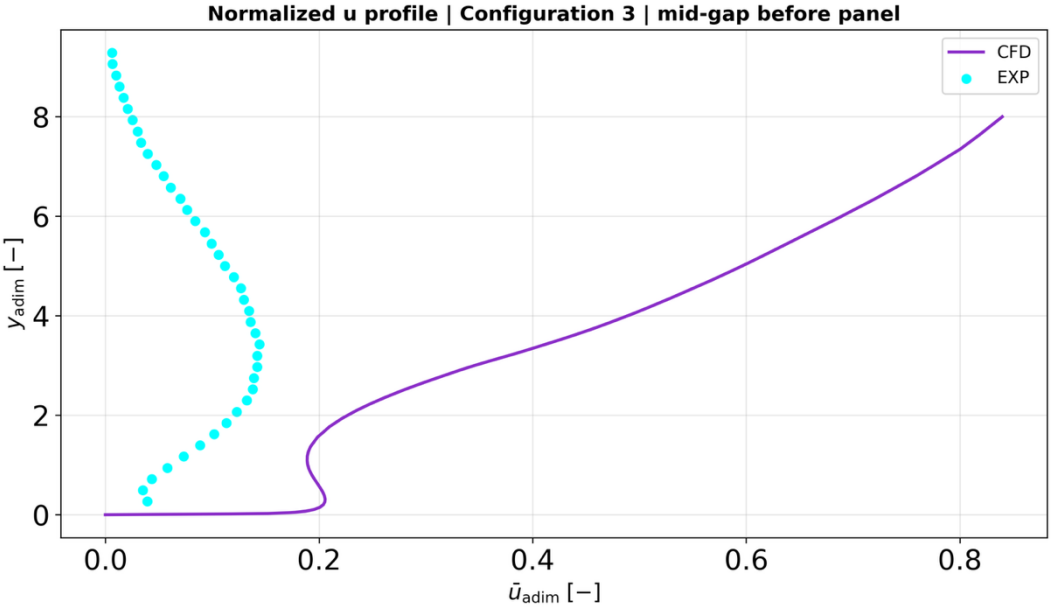

Figure 60: Profile of normalized longitudinal velocity for CFD simulations and experiments in the upstream gap between rows position, Configuration 3

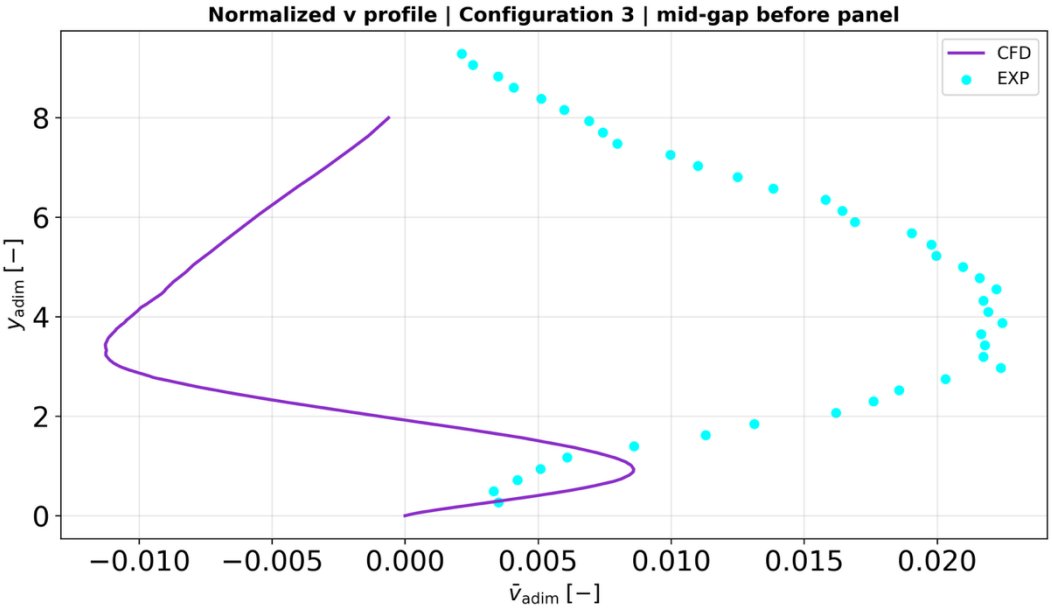

Figure 61: Profile of normalized vertical velocity for CFD simulations and experiments in the upstream gap between rows position, Configuration 3

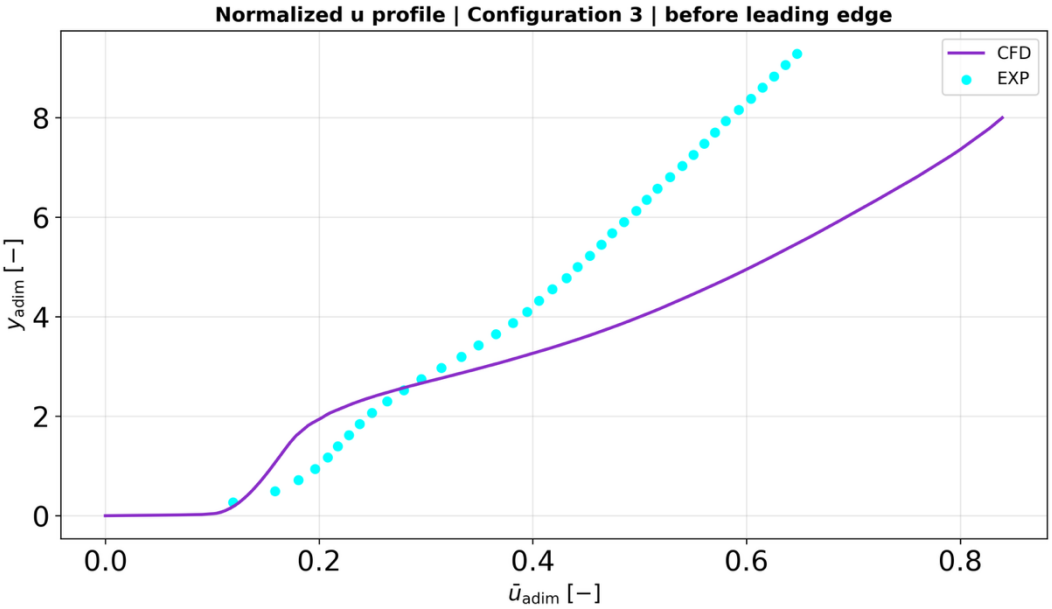

Figure 62: Profile of normalized longitudinal velocity for CFD simulations and experiments in the position before the leading edge, Configuration 3

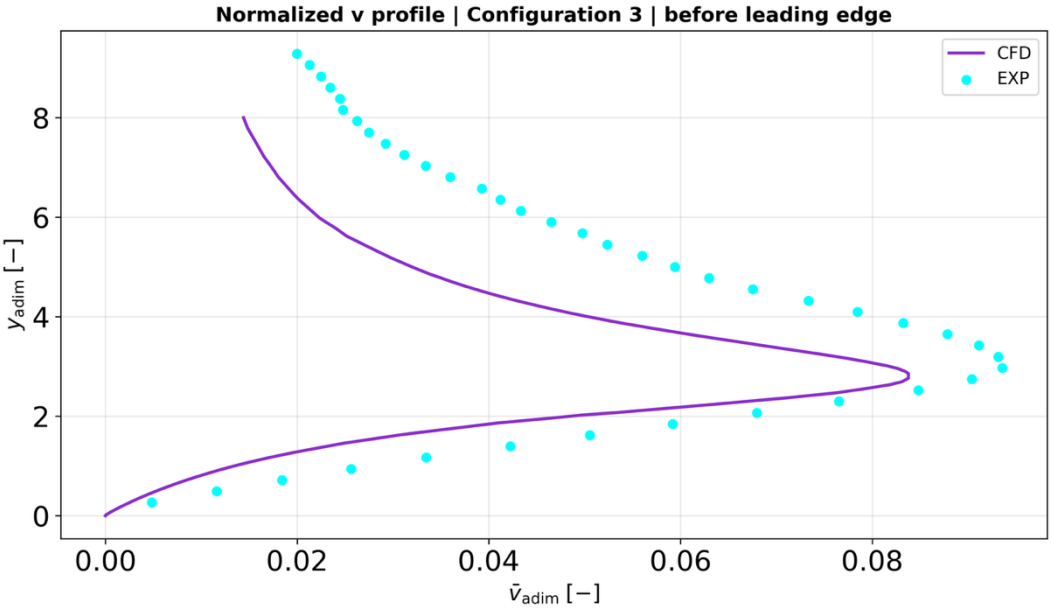

Figure 63: Profile of normalized vertical velocity for CFD simulations and experiments in the position before the leading edge, Configuration 3

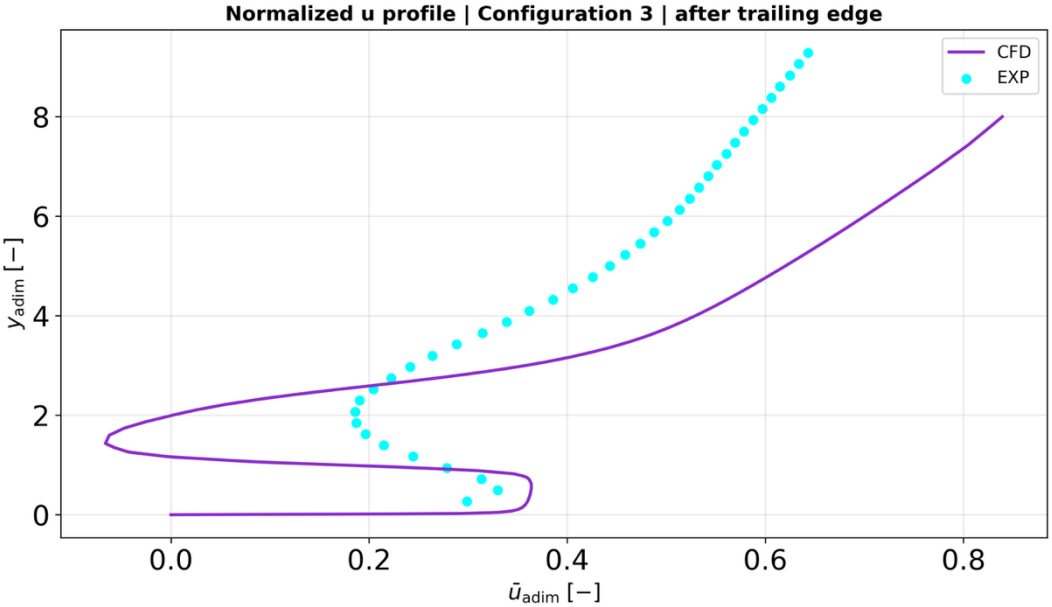

Figure 64: Profile of normalized longitudinal velocity for CFD simulations and experiments in the position after the trailing edge, Configuration 3

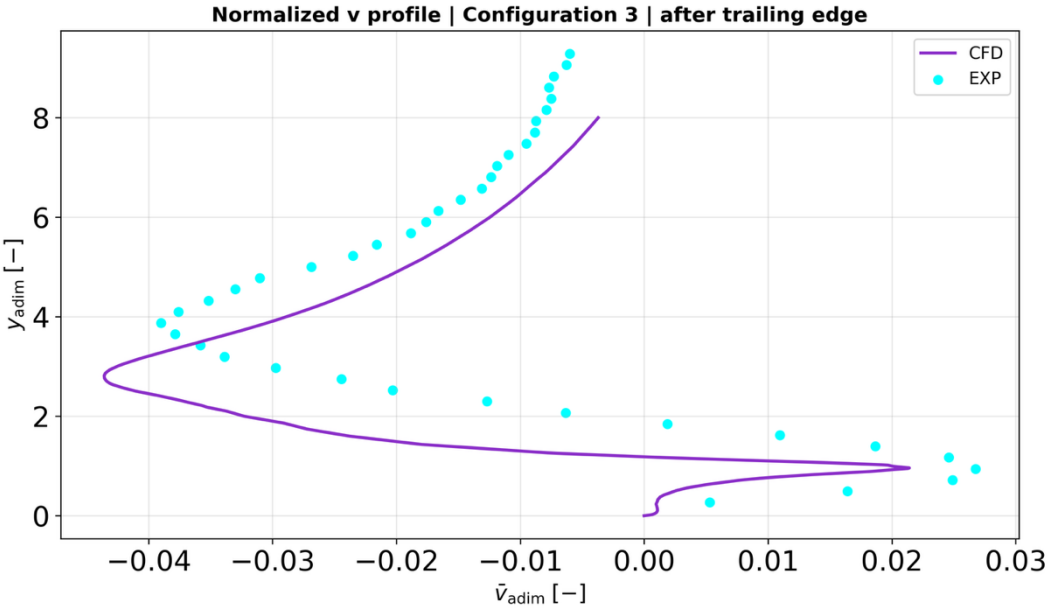

Figure 65: Profile of normalized vertical velocity for CFD simulations and experiments in the position after the trailing edge, Configuration 3

Finally, the analysis of Configuration 3 explores the impact of an increased row spacing on the velocity field. By tripling the distance between the rows, the system is free from the interference each row exerts on the subsequent one, effect occurring in the compact layouts. This wider inter-row gap allows the low-velocity wake plume to gradually dissipate and progressively regain momentum before encountering the subsequent module, in fact in the upstream gap longitudinal position (Figure 60), the curve of normalized *u* show a different behaviour respect to the previous configurations (Figure 48 and Figure 54), as the wider distance allows the fluid to regain velocity, thus is not influenced by the slow velocity plum of the previous panel, assuming a different bell-shape shape with the pick moved towards higher values respect to the bottom and highest part (the contrary compared to Configuration 1 and 2, where the vertex of the parabola has a lower value compared to the highest and lowest *y*-coordinate). This phenomenon is captured by the experimental *v* profile in the gap (Figure 61), which highlight a rising of the fluid in the region, as it has regained momentum. Furthermore, as seen in the *v* distribution map (Figure 47), the flow is able to develop its turbulent behaviour and the streamlines path draw developed eddies behind the panel, explaining the negative values of *v* at the longitudinal position after the trail, at the height of the leading edge. Conversely, the bidimensional numerical solver was not able to predict

the behaviour of the fluid completely, especially in the gap region, assuming negative values of *v* (Figure 61), meaning that for the simulations the free-stream fluid is still descending, while the experimental values highlight a contrary trend. Furthermore, behind the panel it assumes a longer slow plume, with lower values of *u* (Figure 64). In summary, the CFD is not really able to capture the fluid motion, which further explains the $\overline{h_t}$ divergencies.

4.4 Turbulent kinetic energy evaluation

As previously hypothesized, the systematic underestimation of the convective heat transfer coefficient by the numerical model is strictly linked to its inability to correctly depict the turbulent flow field. For this reason, in this work it is worth evaluating the turbulent kinetic energy. As seen in the methodology, for the CFD simulations the *k* is treated as an independent variable and is intrinsically calculated by the software through a dedicated transport equation, balancing turbulence production and dissipation. Conversely, the experimental data were acquired though particle image velocimeter and, to calculate the total experimental turbulent kinetic energy, the assumption of isotropic turbulence was applied to estimate the missing third spatial component, leading to Equation 57. To ensure that the analysis is conducted in a region where the normalized heat transfer coefficient is stable, the *k* profiles are evaluated around the 15th panel for the configurations with minor row spacing (Configuration 1 and 2) and around the 5th panel for the configuration with major row spacing (Configuration 3). The dimensionless profiles are then extracted at different longitudinal positions to evaluate the correct evolution of *k* around the panel and, in particular, the profiles extracted are the ones upstream the inter-row gap, just before the leading edge and immediately after the trailing edge. To compare the CFD profiles with the experimental ones, both turbulent kinetic energy and vertical coordinate have been normalized. The *y*-coordinate is normalized by the ground clearance of the baseline configuration (Configuration 1), while the *k* is normalized by the square of the undisturbed free-stream velocity. Firstly, it is useful to visualize the experimental *k*

spatial distribution around the panel where the normalized convective heat transfer coefficient is stable and then proceed by comparing the *k* profiles for both experiments and CFD simulations across the three configurations, so that the $\overline{h_t}$ behaviour can be better comprehended.

4.4.1 Analysis of the experimental turbulent kinetic energy

Turbulent kinetic energy represents the mean kinetic energy per unit mass associated with the eddies in a turbulent flow, quantifiably measuring the turbulence intensity which is responsible for the transport of momentum and heat through the boundary layer. Turbulent mixing acts as the primary driver for convective cooling in photovoltaic arrays and a high level of turbulent kinetic energy indicates intense macroscopic mixing of the fluid, thinning the boundary layer developing over the ground and promoting a continuous interaction between the air near the surface and the cooler, high-momentum flow from the free-stream. Consequently, an increase in local turbulence near the wall intrinsically leads to an enhancement of the convective heat transfer coefficient.

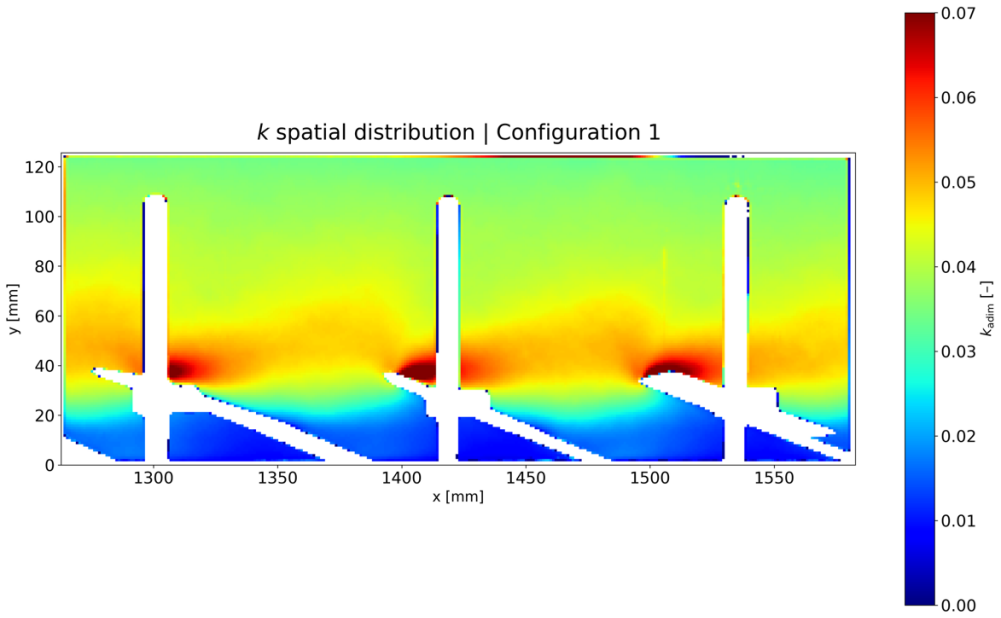

Figure 66: Turbulence kinetic energy distribution around the panel with stable $\overline{h_t}$, Configuration 1

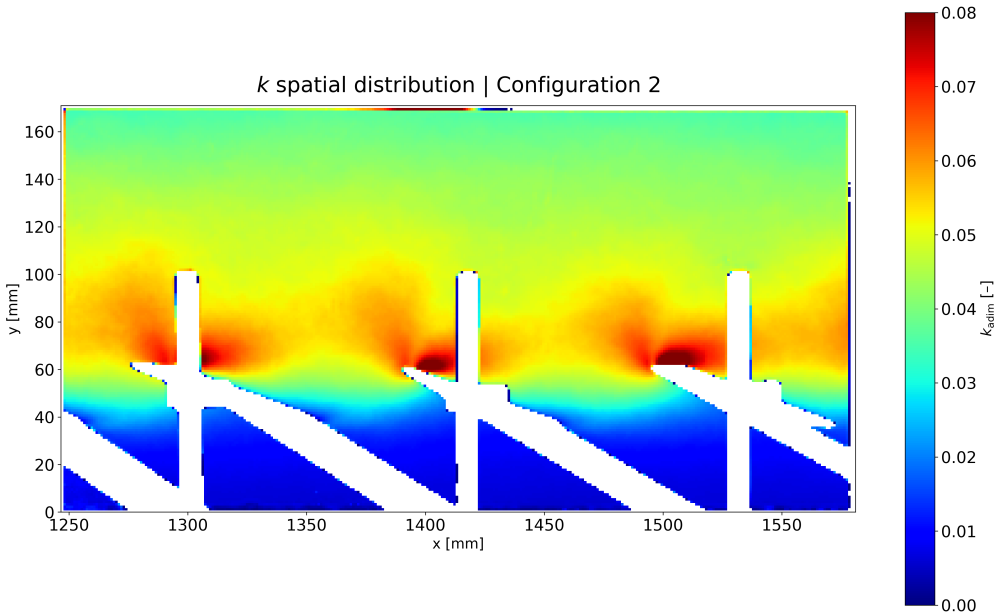

Figure 67: Turbulence kinetic energy distribution around the panel with stable $\overline{h_t}$, Configuration 2

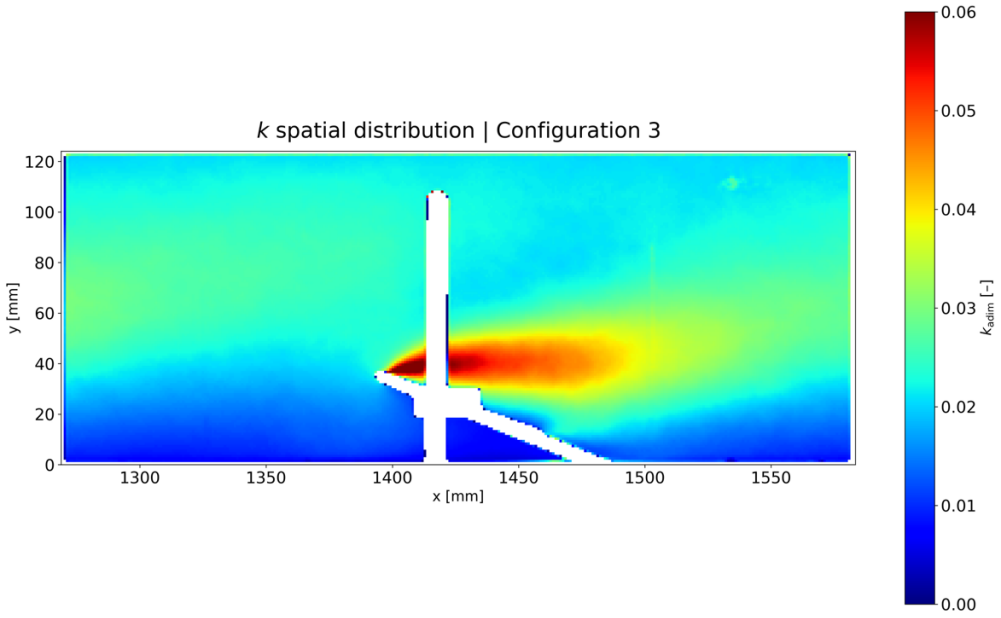

Figure 68: Turbulence kinetic energy distribution around the panel with stable $\overline{h_t}$, Configuration 3

The experimental distribution of *k* clearly highlights how the array geometric parameters drastically alter the turbulent wake trajectory and its interaction with the ground surface. In the baseline compact layout (Configuration 1), the contour map shows that the highly energetic wake generated at the trailing edge bypasses the narrow inter-row gap, maintaining a predominantly horizontal trajectory over the panels.

Consequently, the near-wall region remains characterized by low turbulence intensity, keeping the macroscopic mixing at the ground level relatively weak. When the ground clearance is increased (Configuration 2), the core of the turbulent mixing is shifted to a much higher vertical coordinate, preventing the energetic eddies from meeting the ground, and the energetic wake slightly shrinks as it crosses the inter-row gap, before thickening again upon encountering the leading edge of the subsequent panel. The value of *k* gets slightly higher at the panel level respect to Configuration 1, as the eddies have more vertical space. As shown in Figure 67, this elevated trajectory consistently leaves a vast calm region with negligible *k* underneath the modules and, indeed, this *k* behaviour justifies the overall reduction in the normalized convective heat transfer coefficient in Configuration 2 (Figure 36) compared to Configuration 1 (Figure 35), as it reflects a lower mixing and a thickening of the boundary layer. Furthermore, tripling the row spacing (Configuration 3) reveals a distinct spatial evolution of the turbulent wake. While a high concentration of normalized turbulent kinetic energy is still observed near the leading edge of the panels, similar to the previous layouts, the significantly larger inter-row distance allows for a higher dilution and redistribution of *k* between consecutive panels. As clearly visible in the contour map in Figure 68, the highly energetic wake tends to stretch further downwards into the sub-panel region. Consequently, this downward expansion induces a much stronger macroscopic mixing near the ground surface, justifying the higher normalized convective heat transfer coefficient observed in Configuration 3 (Figure 37) when compared to Configuration 1 (Figure 35).

4.4.2 Analysis of the experimental and CFD profiles of the turbulent kinetic energy

While the contour maps provide a clear qualitative understanding of the *k* behaviour for experimental cases, extracting the dimensionless TKE profiles at specific longitudinal locations is essential to highlight the localized limits of the 2D CFD simulations in depicting the turbulent field.

4.4.2.1 Normalized k for Configuration 1

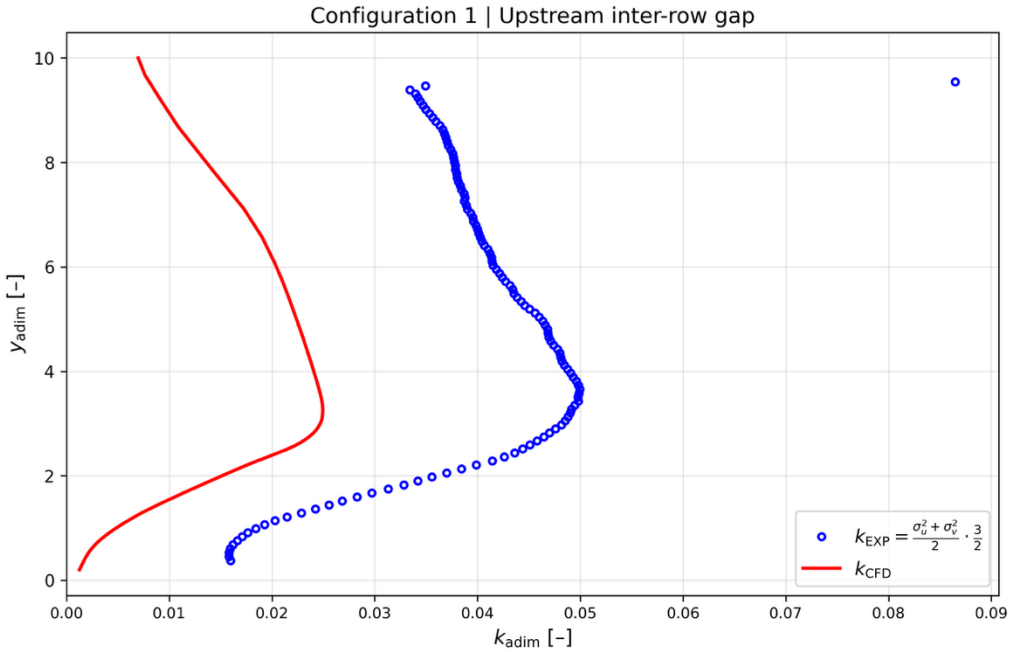

Figure 69: Comparison of k_{adim} profiles between experiments and 2D CFD simulations in the upstream inter-row gap, Configuration 1

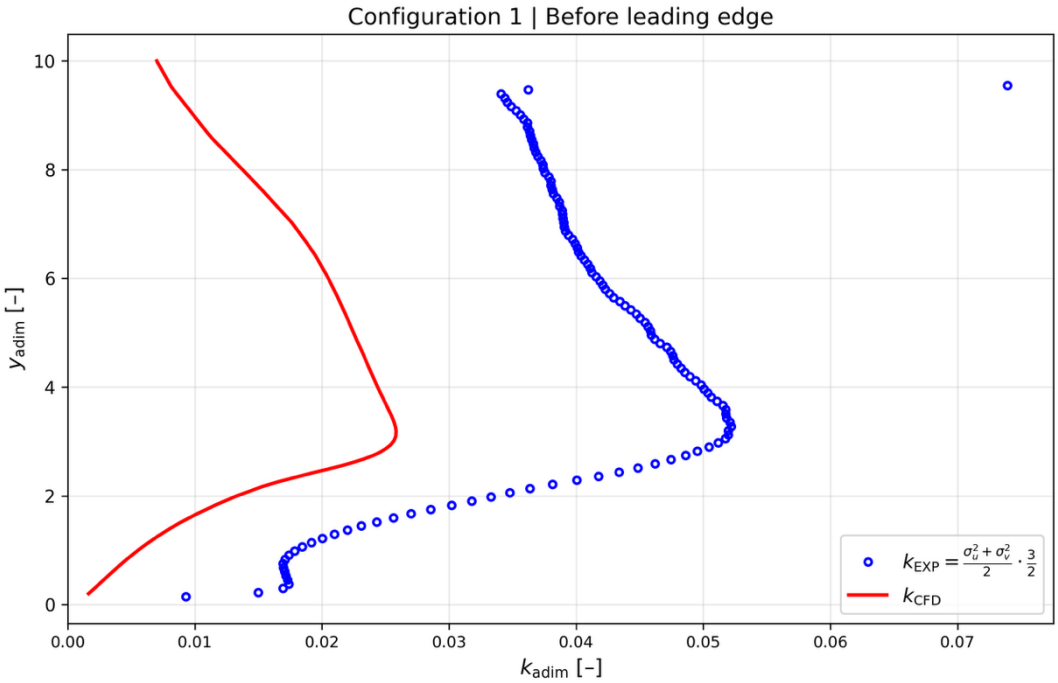

Figure 70: Comparison of k_{adim} profiles between experiments and 2D CFD simulations just before the leading edge, Configuration 1

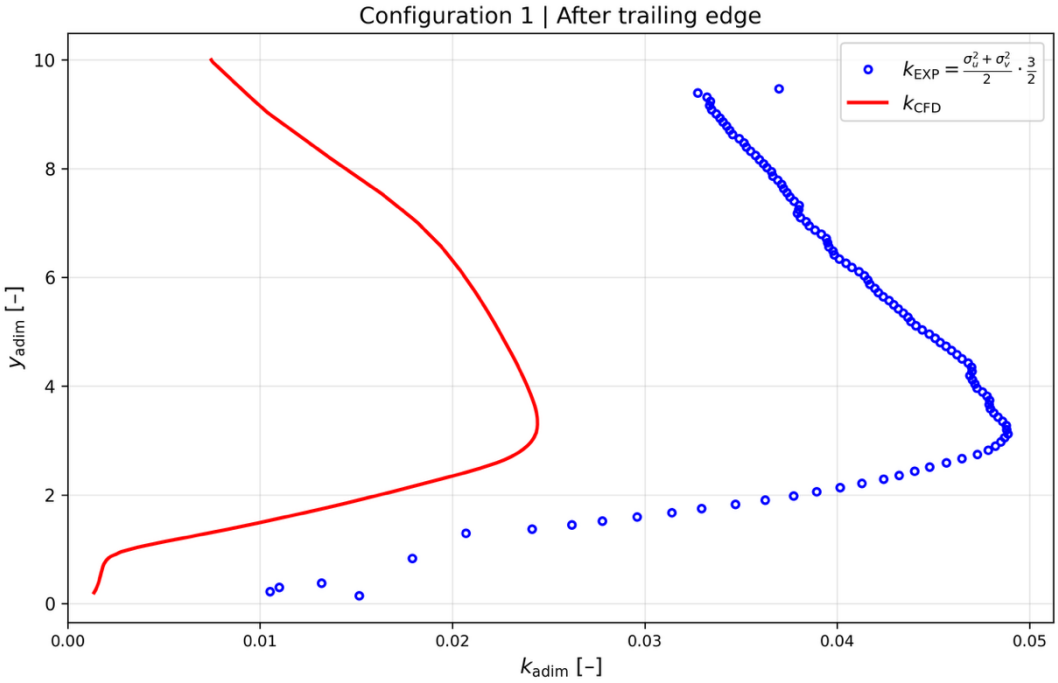

Figure 71: Comparison of k_{adim} profiles between the scattered experimental values and the 2D CFD simulations just after the trailing edge, Configuration 1

Regarding the baseline layout, the proximity of the rows significantly limits the deep turbulence penetration into the inter-row gaps. Observing the extracted experimental profiles (blue points), it is evident that the maximum generation of turbulent kinetic energy occurs exactly at the height of the leading edge, perfectly matching the visual behaviour illustrated in the *k* spatial distribution map (Figure 66). From this specific height, the turbulence progressively fades out as it moves downwards, reaching a negligible magnitude near the ground. Conversely, moving upwards above the leading edge height, the turbulent kinetic energy decreases with a gentler slope, as the curve approaches the undisturbed free-stream region. This characteristic bell-shaped distribution is consistently replicated across the other investigated longitudinal locations. Immediately after the trailing edge, the profile maintains a similar shape, exhibiting a localized peak at the panel's elevation, although slightly reduced in magnitude compared to the profile near the leading edge, followed by the same progressive decay towards the free-stream above and a sharp drop towards the floor. The same occurs in the upstream inter-row gap, where the profile depicts an identical bell-shaped curve, but with lower peak values. In summary, the highest value of

normalized turbulent kinetic energy remains confined at height of the leading edge, while a steep descent in values is recorded when moving downwards, reaching basically negligible values as the flow approaches the terrain, and a gentler decay is observed reaching the upstream undisturbed fluid. When comparing the experimental points with the 2D CFD results (continuous red line), a widespread underestimation is evident across all the investigated longitudinal positions. Although the numerical model qualitatively reproduces the expected bell-shaped profile along the *y*-coordinate, the simulation values fail to capture the correct magnitude of the dimensionless *k* across all regions. This behaviour highlights the limitations of the bidimensional RANS approach in capturing the correct behaviour of the fluid, underestimating the turbulence and, consequently, the normalized convective heat transfer coefficient, as observed previously for this baseline configuration (Figure 39).

4.4.2.2 Normalized k for Configuration 2

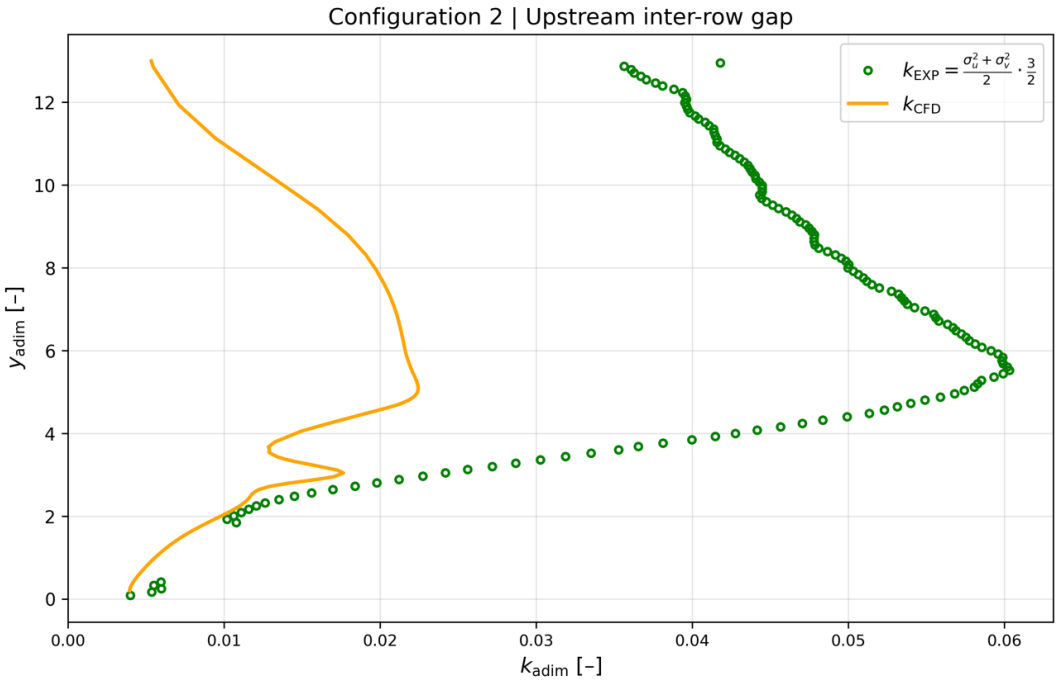

Figure 72: Comparison of k_{adim} profiles between the scattered experimental values and the 2D CFD simulations in the upstream inter-row gap, Configuration 2

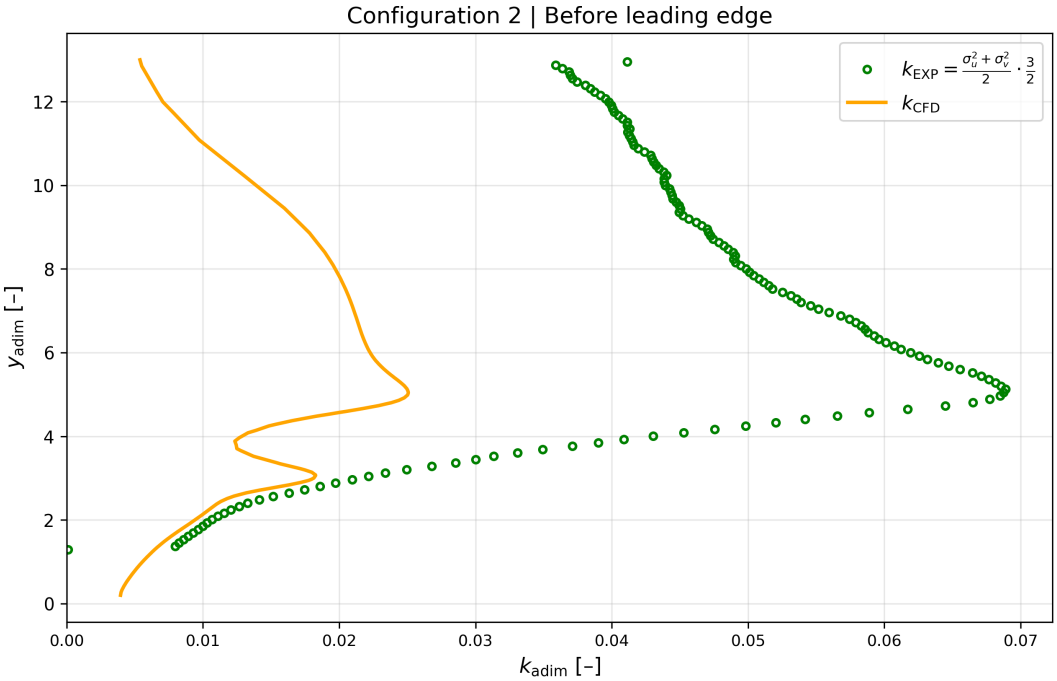

Figure 73: Comparison of k_{adim} profiles between the scattered experimental values and the 2D CFD simulations just before the leading edge, Configuration 2

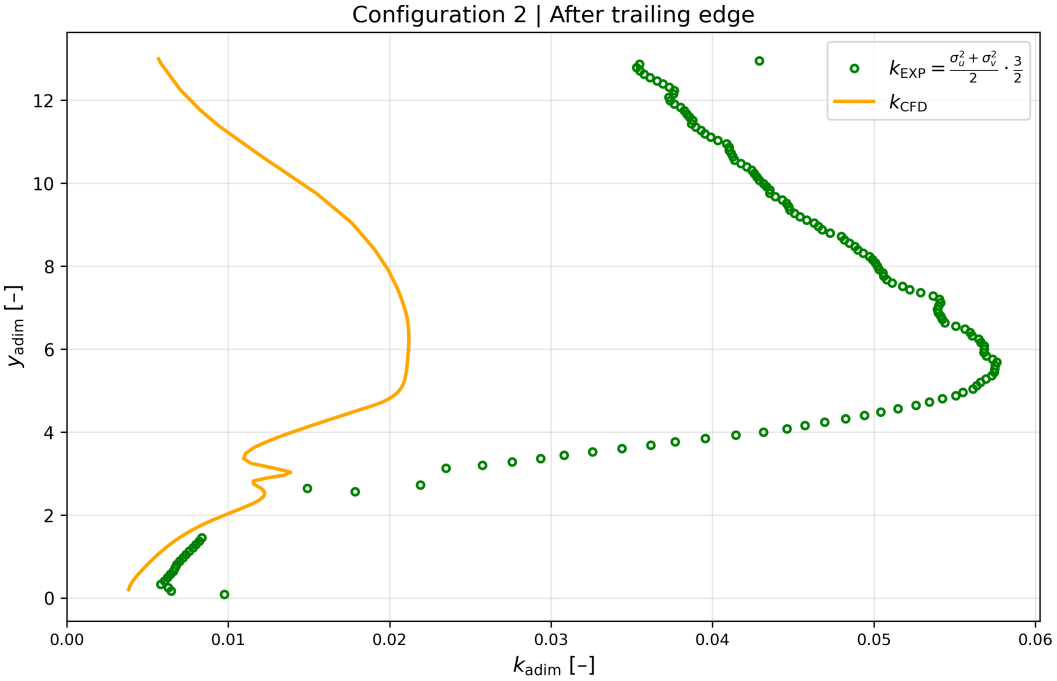

Figure 74: Comparison of k_{adim} profiles between the scattered experimental values and the 2D CFD simulations just after the trailing edge, Configuration 2

To analyse the effect of the increased ground clearance, the elevated layout (Configuration 2) is considered, where the turbulence generation is shifted to higher vertical coordinates. Since the vertical axis is normalized using the same reference length across all configurations, which is the ground clearance of the baseline agrivoltaic system, the higher physical position of the modules directly translates into the peak of turbulent kinetic energy occurring at a higher y-coordinate compared to the baseline case (and to Configuration 3). Observing the experimental points (green markers), it is evident that the maximum generation of turbulent kinetic energy occurs exactly at this elevated height of the leading edge, perfectly matching the visual behaviour illustrated in the spatial distribution map (Figure 67). As the bell-shaped curve suggests, from this specific height, the turbulence progressively fades out as it moves downwards, covering a wide sub-panel empty region with a steeper curve with respect to Configuration 1, before reaching a negligible magnitude near the ground. Again, moving upwards above the leading edge height, the turbulent kinetic energy decreases with a gentler slope as the curve approaches the undisturbed free-stream region, exactly as observed in Configuration 1. This characteristic elevated bell-shaped distribution is consistently replicated across the other investigated longitudinal locations. Immediately after the trailing edge and in the upstream inter-row gap, the profiles maintain the same shape and progressive decay described for Configuration 1, but are characterized by the upward shift and generally by higher peak values. In summary, the overall behaviour mirrors the baseline layout, with the highest value of normalized turbulent kinetic energy confined at the elevated height of the leading edge and a slow increase of *k* in the free-stream region, but with steeper descent in values when moving downwards, which justify the lower mixing and $\overline{h_t}$ (Figure 40), as the turbulence effect is confined in the upper region. Again, as seen in Configuration 1, when comparing the experimental points with the 2D CFD results (continuous purple line), it is evident that the turbulence behaviour of the fluid is underestimated, explaining the divergence in $\overline{h_t}$ values. Hower, in this case, the CFD simulations seem to reproduce correctly the value of *k* just above the ground, which are basically superimposed on the experimental scattered points. But

in the region just beyond it, the CFD curves start to assume an irregular trend, far from the smooth bell-shape of Configuration 1.

4.4.2.3 Normalized k for Configuration 3

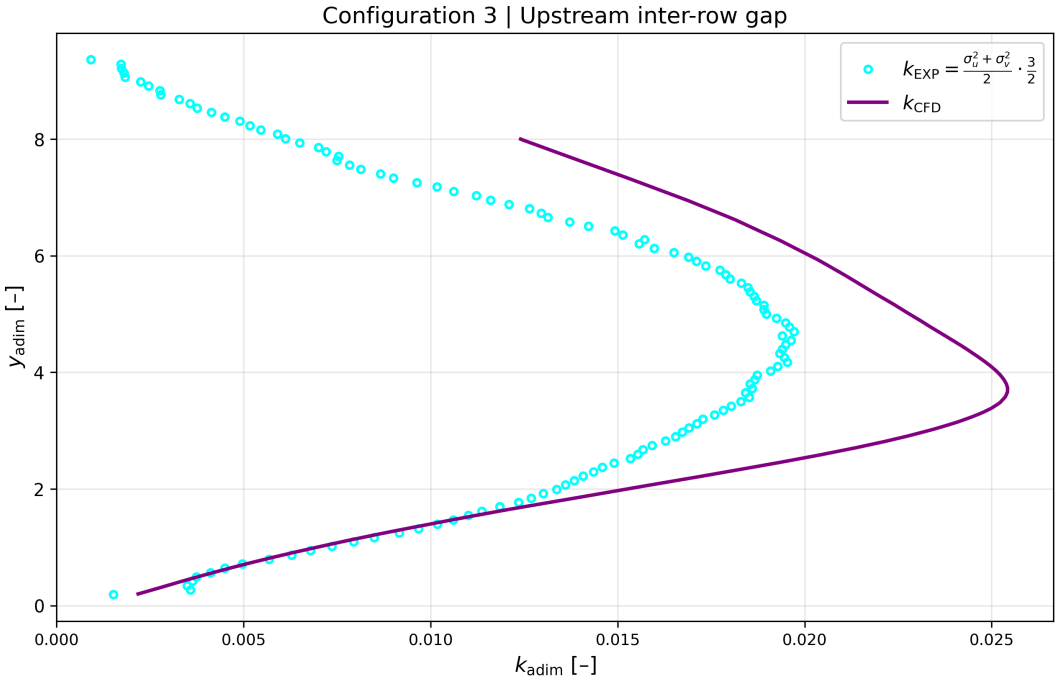

Figure 75: Comparison of k_{adim} profiles between the scattered experimental values and the 2D CFD simulations in the upstream inter-row gap, Configuration 3

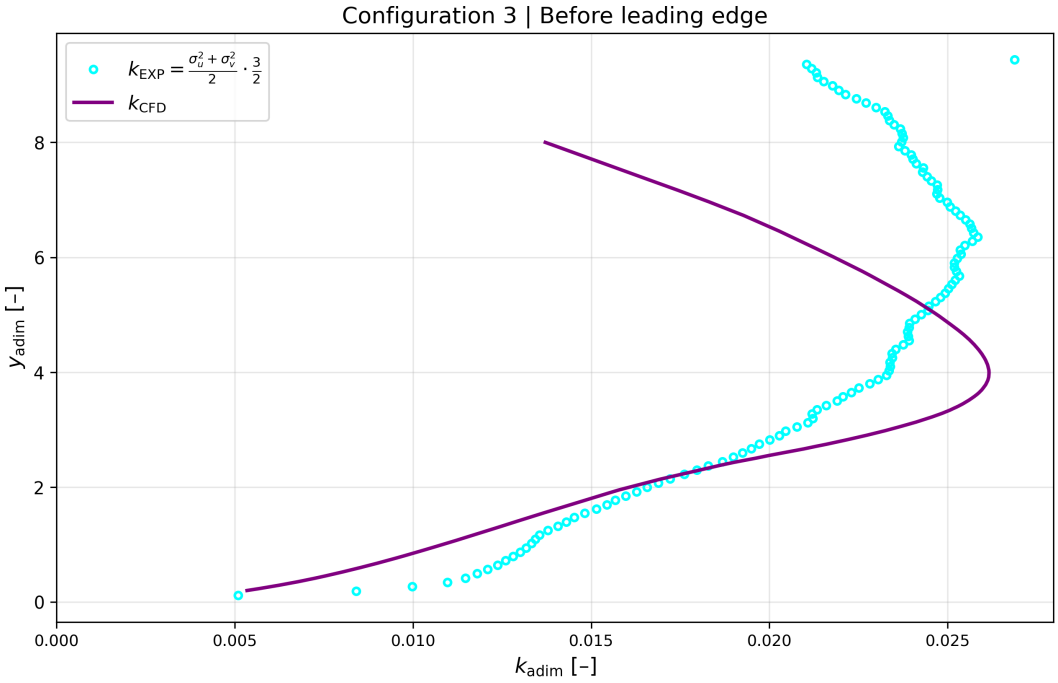

Figure 76: Comparison of k_{adim} profiles between the scattered experimental values and the 2D CFD simulations just before the leading edge, Configuration 3

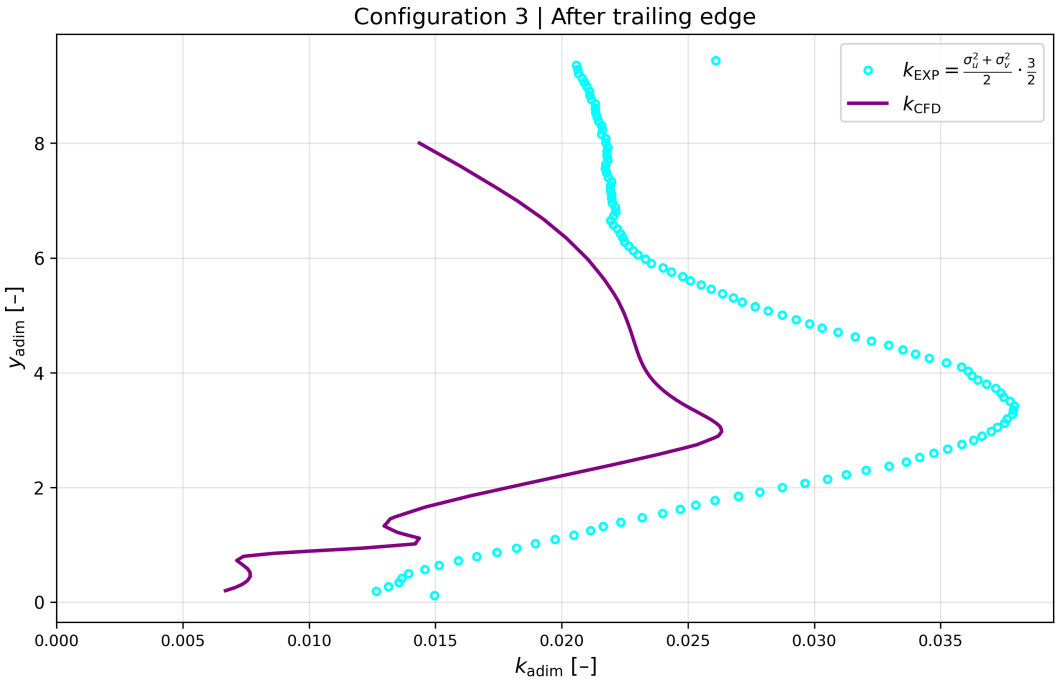

Figure 77: Comparison of k_{adim} profiles between the scattered experimental values and the 2D CFD simulations just after the trailing edge, Configuration 3

Finally, the effect of the increased row spacing, represented by the third agrivoltaic system's configuration, is considered, with a wider inter-row gap that enhance turbulence penetration into the region between the rows. Observing the extracted experimental profiles (cyan points), it is evident that, similar to the previous configurations, the distribution exhibits a bell-shaped curve with the peak of turbulent kinetic energy occurring at the height of the trailing edge. However, unlike the other configurations, an upward shift of the peak is observed in the position before the leading edge and the values of k at this longitudinal position and the one in the upstream gap between rows, are lower compared to the profile just after the trailing edge. And this is visible in the *k* spatial distribution map of Configuration 3 (Figure 68) where, just behind the panel, a longer wake of concentrated normalized *k* is present, indicating that high values are maintained horizontally for a longer distance, promoted by the wider row spacing. Furthermore, precisely because there is more space between the panel rows, the turbulent kinetic energy has the space to develop along the panel, assuming higher values along its descent towards the ground. This effect is visible in the spatial map (Figure 68), which reveals a downward development of the turbulence that was absent in the other configurations. This protracted turbulence leads to enhanced mixing in the lower levels, causing a thinning of the boundary layer. This physically explains, as discussed in the previous chapter, why higher values of the normalized convective heat transfer coefficient are recorded in Configuration 3. When comparing the experimental points with the 2D CFD results (continuous orange line), the peak values of the dimensionless *k* are more similar between the CFD and the experiments in the inter-row space and after the trailing edge. Again, there is an underestimation of the turbulence, which is localized in the longitudinal position after the trailing edge, with a lower leak, due to the *k* development just mentioned because of the wide space between the rows. While in the other two longitudinal position the CFD simulations manage to recover the gap that was created in the other configurations with a smaller row spacing, representing the values of *k* more accurately, especially in the lower height position.

4.5 Vorticity evaluation

To conclude the aerodynamic analysis, the last step is the introduction of the vorticity parameter, whose field is useful to link the mean velocity gradients and the generation of turbulent kinetic energy. As discussed in the methodology, the vorticity provides a measure of the local rotation of the fluid, which is strictly driven by the wind velocity field (as seen in Equation 28) and turbulence generation. Following the standard convention, a positive value of vorticity denotes a counterclockwise rotation of the fluid, whereas a negative value indicates a clockwise rotation. In the context of agrivoltaic arrays, mapping these rotational structures allows to locate the exact position of violent flow separation at the module's edges. These concentrated regions of intense vorticity physically represent the shear layers where extreme velocity gradients break down into chaotic eddies, as visually depicted in Figure 14. Therefore, the vorticity acts as the direct source feeding the turbulent kinetic energy and physically justifies the macroscopic flow deflections, such as updrafts and downdrafts, previously observed in the velocity profiles. Furthermore, to ensure an objective comparison between experimental data and the numerical simulations, the vorticity values are normalized by multiplying them by the baseline agrivoltaic system ground clearance and dividing by the undisturbed freestream velocity of $5\frac{m}{s}$. This standard scaling provides a dimensionless vorticity parameter that is completely independent of the absolute wind speed and the physical scale of the model, isolating the impact of the varying geometric layouts.

4.5.1 Experimental vorticity

The experimental spatial distribution maps of vorticity provide the definitive visual confirmation of the aerodynamic phenomena deduced from the velocity and turbulent kinetic energy profiles. By visually translating the local rotation of the fluid elements, these maps highlight the exact locations of flow separation and the subsequent evolution of the turbulent structures across the different geometric arrangements.

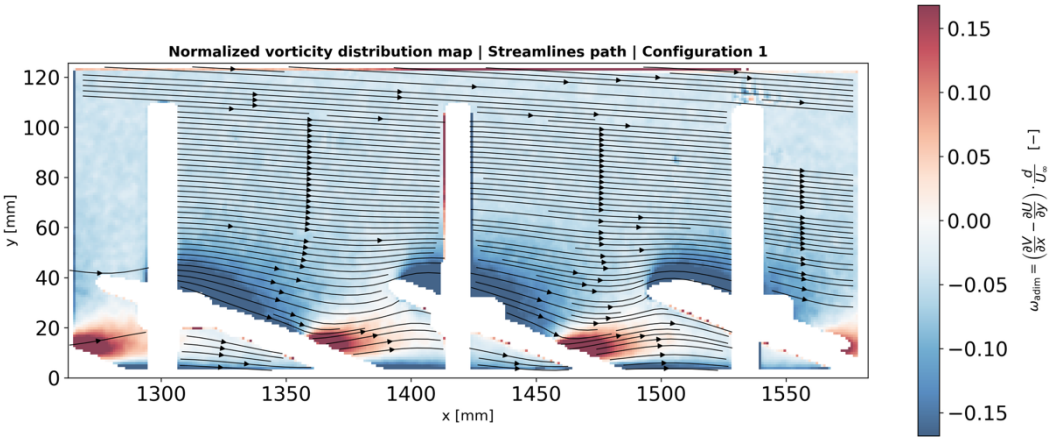

Figure 78: Normalized velocity distribution, Configuration 1

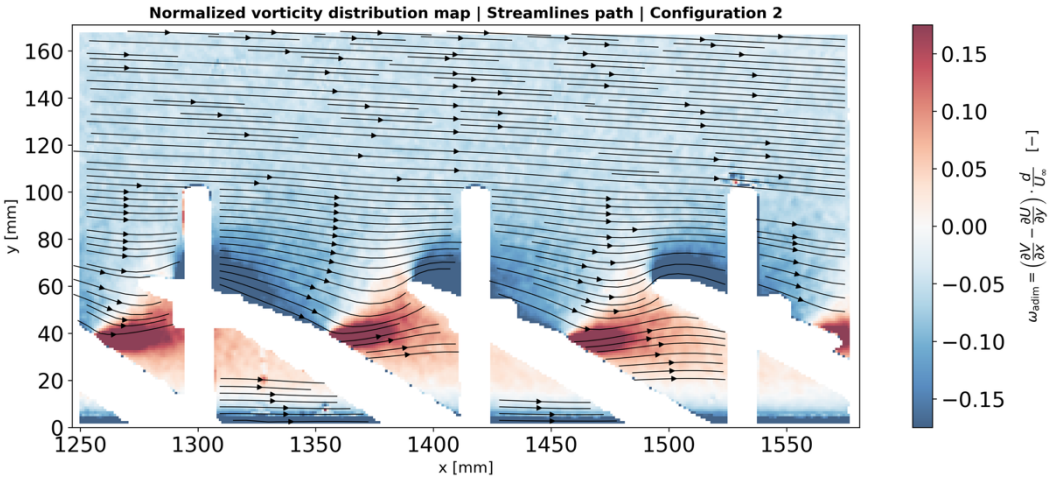

Figure 79: Normalized velocity distribution, Configuration 2

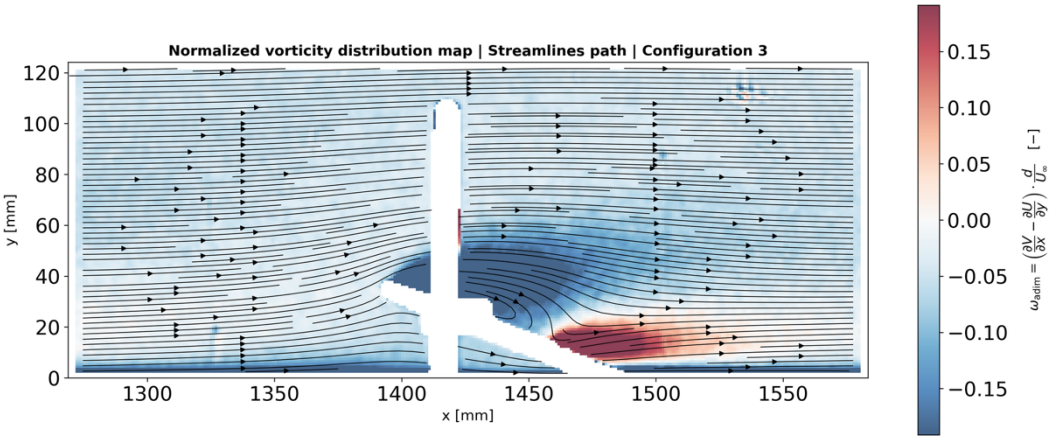

Figure 80: Normalized velocity distribution, Configuration 1

Observing the baseline layout (Configuration 1), the maps display intense regions of concentrated normalized vorticity localized at the leading edges, with negative values of vorticity as the free-stream air is forced towards the ground, and at the trailing edges, with positive values of vorticity because the hot fluid near the ground is rising to be substituted. The consecutive panels act as an aerodynamic shield, preventing the vortices from fully expanding along the longitudinal direction, but due to the close distance from the ground, this turbulent mixing has the effect of thinning the boundary layer, resulting in a high convective heat transfer coefficient. Moving to the elevated layout (Configuration 2), the behaviour of the vorticity is similar, with positive values at trailing edges and positive values at leading edges, but the higher ground clearance allows the air to mix more in the region between two panel, even because the mean velocity, due to its logarithmic trend, has slightly higher and more spread values in this configuration at the modules' level. In fact it is visible a red cloud that start from the trailing edge and reach the leading edge of the successive panel, and it is clear looking at the previous analysed normalized turbulent kinetic energy, where the higher experimental values recorded were exactly the ones for Configuration 2 (Figure 67, Figure 72, Figure 73 and Figure 74), meaning a higher mixing is occurring in this agrivoltaic system configuration. But due to the higher ground clearance, the near-ground region appears incredibly calm and devoid of macroscopic vorticity. This visual evidence perfectly links to the turbulent kinetic energy maps where, without the fully developed rotating eddies sweeping the lower surface, the turbulent kinetic energy at the ground level drastically drops. The lack of near-surface rotation and turbulent mixing confirms that the elevated layout allows the boundary layer to grow undisturbed, physically acting as an insulating shield for the soil. Finally, the scattered layout (Configuration 3) reveals the fluid-dynamic impact of an increased row spacing. In fact, it exhibits the same trend of Configuration 1 and Configuration 2 (positive values at the trailing edge and negative values at the leading edge), but the immediate blockage imposed by a closely positioned subsequent panel is no longer present, thus the intense vorticity generated at the trailing edge is no longer mechanically squeezed. The maps clearly display fully developed, large-scale rotational eddies that detach from the panel

and expand deeply into the wide inter-row gap, and in fact higher values of vorticity are recorded. This unhindered rotational motion provides the exact physical origin for the macroscopic downdraft of freestream fluid previously observed in the vertical velocity profiles, which allowed the correct penetration and mixing. By drawing high-momentum air downwards, these large-scale rotating eddies generate a massive turbulent kinetic energy plume that actively scrubs the ground, maximizing the macroscopic mixing and ultimately driving the highest convective heat transfer rates observed in the study.

4.5.2 CFD simulations vorticity

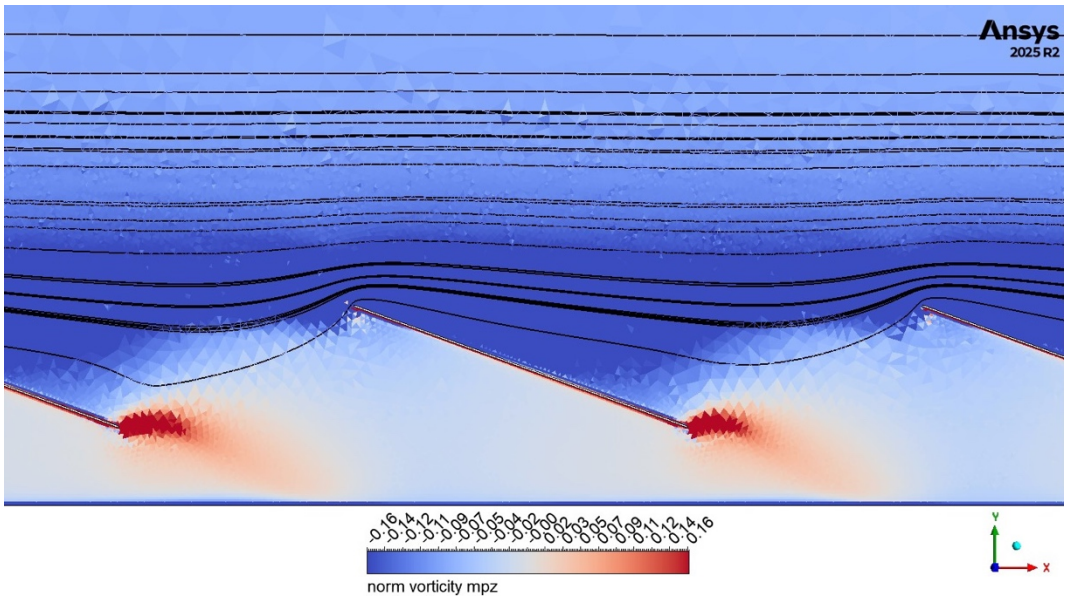

Figure 81: Normalized vorticity distribution map for CFD simulations, Configuration 1

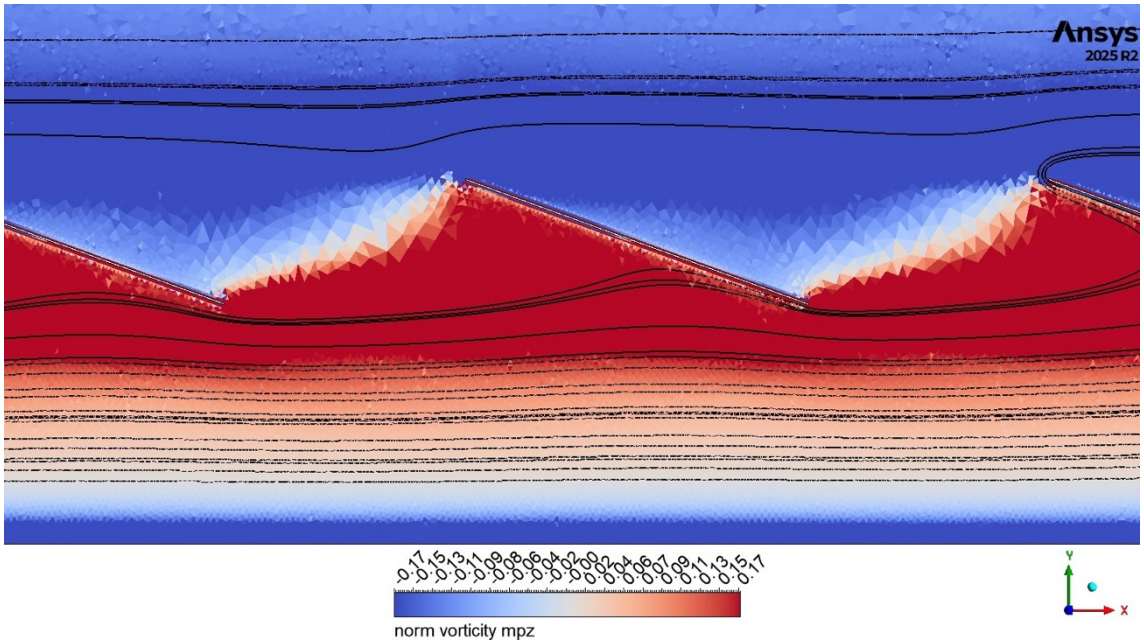

Figure 82: Normalized vorticity distribution map for CFD simulations, Configuration 2

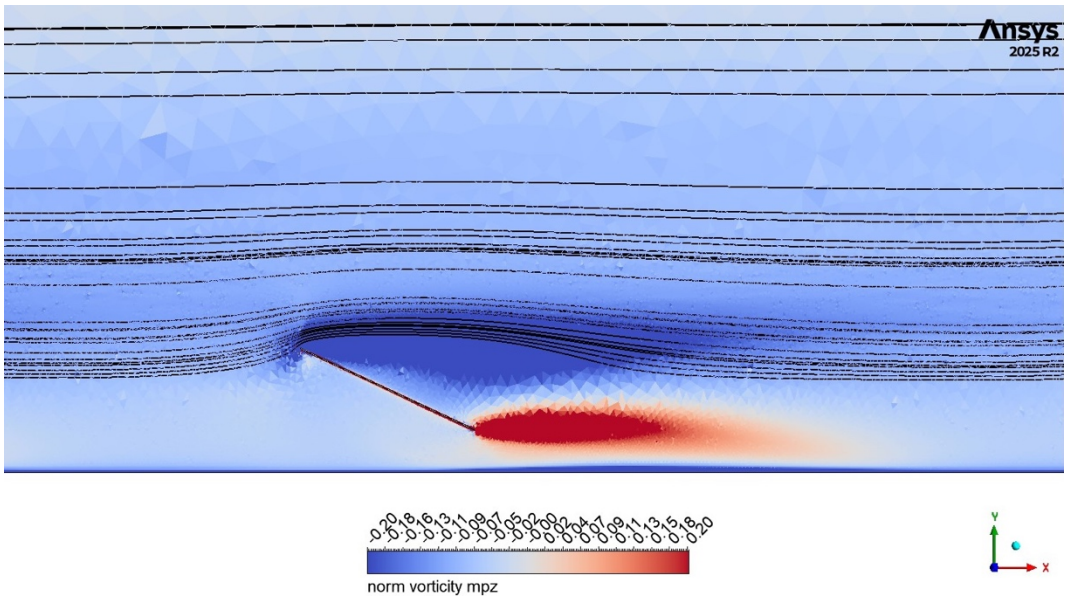

Figure 83: Normalized vorticity distribution map for CFD simulations, Configuration 3

The comparison of the experimental normalized vorticity maps with the 2D simulations further highlights the limitations of the numerical solver in reproducing the correct turbulent dynamics. Observing the compact baseline layout of Configuration 1, the numerical trend observed is similar to the experimental one, with positive values of

normalized vorticity concentrated in the trailing edge area, and negative ones in the upper part of the module. However, the discrepancy lies in the spread of the vorticity and, in fact, while the experimental case exhibits a negative cloud confined to the area behind the panel, in the CFD simulations, compared using the same vorticity scale limits, the negative cloud spreads to the following panel, involving the gap area. Instead, when examining the elevated layout of Configuration 2, even though the negative and positive values are correctly located along the module, the negative values do not really spread along the panel starting from the leading edge, but form a wake with a horizontal behaviour, that gets connected to the following panel, thus overestimating the shield effect of the agrivoltaic system as the flow is slower and, to recover, the free-stream try to penetrate for a longer way along the longitudinal axis. While the positive values of normalized vorticity, even if they spread correctly in the gap, reconnecting from the trailing edge with the following panel's leading edge, try to spread more beneath the panel, showing a different stratification compared to the experimental values. Finally, when evaluating the scattered layout of Configuration 3, while the experimental vorticity distribution shows the cloud of values concentrated in the module area, the CFD vorticity map shows a more relaxed behaviour, with the vorticity forming a plume at the leading and trailing edges. In summary, it appears that the CFD simulations tend to underestimate the vorticity concentration, assuming an excessive shield effect of the agrivoltaic system with a correlated more stretched behaviour of normalized vorticity.

5 Conclusions and future developments

5.1 Conclusions

This thesis work aimed to investigate the fluid dynamic impact of different agrivoltaic system geometries in a turbulent regime on the convective heat transfer from the air to the ground. This parameter is fundamental for determining the microclimate generated beneath the system, particularly the phenomenon of evapotranspiration. The latter, being directly correlated to convective exchange through the Chilton-Colburn analogy, provides a direct estimate of moisture retention and the resulting water savings of the system, thus demonstrating how specific array configurations dictate the fundamental trade-off between panel cooling and agricultural water saving. Specifically, the convective heat transfer coefficient normalized against a reference case, which is a flat plate without panels, was analysed to isolate the impact of each layout type. Three configurations were examined: Configuration 1 with baseline values, Configuration 2 with a higher ground clearance, and Configuration 3 with a greater row spacing. The analysis was based on the comparison between experimental results obtained in a wind tunnel and 2D CFD numerical simulations, based on the k-ω SST turbulence model. Notably, a geometric scale difference exists between the two approaches as the wind tunnel experiments were conducted on a 1:75 scaled model of the agrivoltaic system, whereas the numerical CFD simulations were developed at full scale. The data were provided by the École Centrale de Lyon and have been studied and developed through different tools. Specifically, the CFD data have been studied and visualized by using both ANSYS FLUENT, to post-process the results of the simulations and extract the profiles of vorticity and turbulent kinetic energy, and Paraview, to extract the velocity profiles. Meanwhile, the experimental data and PIV images have been manipulated by Python scripts to analyse all the various parameters, and plot the comparison graphs of the experimental and numerical results. In fact, by comparing the experimental results with the CFD post-processed results, it was possible to evaluate the reliability of the two-

dimensional numerical approach through a cross-examination of exchanged heat, velocity fields, turbulent kinetic energy, and vorticity. Regarding the normalized convective coefficient, the maximum value was experimentally recorded in Configuration 3 because, under turbulent conditions, the wide spacing between rows allowed for greater mixing between the air at ground level and the high-energy air of the free-stream. While this phenomenon promotes significant cooling of the area and the modules, improving electrical production since high temperatures strongly affect the panel efficiency, it also maximizes water loss. Conversely, Configuration 2 showed the lowest normalized coefficient value, meaning that the high ground clearance kept the turbulence phenomena generated by the modules away from the lower layers, thereby limiting the evapotranspiration rate and favouring water savings. To comprehend the physical mechanisms driving these thermal and hydrological performances, the aerodynamic field was investigated. The analysis of mean velocity profiles, turbulent kinetic energy, and vorticity maps provided the fundamental fluid-dynamic explanation for the observed experimental behaviours, illustrating exactly how the airflow and turbulence are modulated by the different array geometries. Specifically, the analysis highlighted that Configurations 1 and 2 share very similar aerodynamic trends: their longitudinal velocity profiles exhibit a persistent low-velocity wake plume squeezed by the narrow row spacing, their turbulent kinetic energy peaks at the leading edge elevation but rapidly decays without scrubbing the ground, and their vorticity is mechanically confined between the closely packed panels. Conversely, Configuration 3 displays a markedly different behaviour: the wider spacing allows the flow to regain momentum, causing the velocity profiles to reshape as the wake dissipates. Furthermore, the turbulent kinetic energy and the fully developed vorticity eddies can freely expand downwards into the wide inter-row gap, physically scrubbing the ground and drawing high-momentum freestream air downwards, which provides the aerodynamic reason for the maximized convective heat transfer. Furthermore, these same aerodynamic parameters were crucial to investigate why these experimental results differed from those obtained in the 2D CFD simulations, which systematically underestimated the heat exchange. By examining the mean velocity field, a global

tendency of the CFD to overestimate the shield effect of the agrivoltaic system was noted, with vertical and horizontal velocity profiles that failed to reproduce the actual mixing of the experimental case. Subsequently, the turbulent kinetic energy parameter was analysed, noting how it strongly concentrates at the panel edges following flow separation. Nevertheless, the CFD exhibits a severe inability to calculate the correct expansion of this turbulence along the domain. Finally, vorticity maps confirmed that the CFD does not correctly recognize the nature of the vortices, creating rigid and horizontal wakes that highlight the panel's shielding phenomenon and confirm this underestimation of turbulence, definitively explaining the 2D numerical model's trend in underestimating ground heat transfer. This probably happens because the 2D model proposes a simplified geometry of the agrivoltaic system. In fact, it does not consider geometric elements such as supports, the various layers of the panels, or the cables. Furthermore, the computational domain is significantly different from the actual environment of the wind tunnel, where the presence of instrumentation, cables, and other disturbing elements inevitably affects the flow, introducing 3D turbulence that cannot be correctly represented in a 2D CFD model

5.2 Future developments

The results of this thesis highlight the differences between a 2D CFD numerical model and experimental data, as faithfully reproducing the complexity of a real case, especially in an agrivoltaic system, proves to be extremely complicated. In fact, there are numerous elements that could be integrated both in experimental campaigns and in numerical simulations to increase the degree of realism. A fundamental example is the presence of the plants themselves, which introduce an element of localized roughness and which, depending on their position and shape, can further alter the aerodynamic behaviour of the agrivoltaic system. Furthermore, to obtain a more complete overall view, numerical analyses could be extended to 3D simulations, but considering a higher computational cost to 2D CFD. A further development concerns the fact that in the wind tunnel, a reduced-scale model was studied compared to the real scale implemented in the CFD simulations, so other physical parameters present in the system, which

inevitably influence the results, could also be scaled. The literature ([61][62][63]) describes the condition of the *Complete Scaling*, which asserts that in the presence of thermal and gravitational effects, the velocity ratio scales as a function of the square root of the geometric ratio. Consequently, for scale reductions typical of a wind tunnel, such as those addressed and seen in this thesis, *Complete Scaling* would require lower wind speeds compared to the real case, making it very difficult to maintain the flow in a fully turbulent regime, or even to achieve it. However, in the interaction of wind with geometries with sharp edges, such as photovoltaic panels, rigid adherence to the equality of the Reynolds number is not strictly necessary because, in a strongly turbulent regime, the principle of Reynolds number independence gets applied. Secondly, the simulation of the buoyancy phenomenon, dictated by the heating of the panels and evapotranspiration, introduces the need to balance inertial and gravitational forces through the Froude relationship, which allows for the use of more realistic test velocities, by distorting in a controlled way the density ratio between the model and the real-scale prototype. In practice, this translates into the possibility of using different fluids or gases between the experiments and the simulation of reality to recreate the correct physics of thermal gradients. For example, by injecting mixtures of light gases, such as helium, to simulate high density gradients while bypassing the physical limits of the wind tunnel.

BIBLIOGRAPHY

[1] Our World in Data, “GHG emissions by sector,” Global Change Data Lab, 2025. https://ourworldindata.org/grapher/ghg-emissions-by-sector?time=earliest..2022

[2] Our World in Data, “Annual CO_2 emissions per country,” Global Change Data Lab, 2025. https://ourworldindata.org/grapher/annual-co2-emissions-per-country?tab=map&time=2024&country=USA~GBR~IND~CHN

[3] Our World in Data, “Electricity mix,” Global Change Data Lab, 2025. [Online]. Available: https://ourworldindata.org/electricity-mix

[4] International Energy Agency. (2025). *China – Countries & regions*. https://www.iea.org/countries/china

[5] International Energy Agency, “Renewables in Europe,” 2025. Available: https://www.iea.org/regions/europe/renewables

[6] Aldy, Joe. “Sudden Turns and Long-Lived Investments: Trump Administration Energy and Climate Policies.” Harvard Kennedy School, March 27, 2025. https://www.hks.harvard.edu/faculty-research/policy-topics/environment-energy/sudden-turns-and-long-lived-investments-trump

[7] IEA-PVPS, “Dual Land Use for Agriculture and Solar Power Production: Overview and Performance of Agrivoltaic Systems,” International Energy Agency Photovoltaic Power Systems Programme, Task 13, Report IEA-PVPS T13-29:2025, 2025

[8] A. Chatzipanagi, N. Taylor, and A. Jaeger-Waldau, "Overview of the Potential and Challenges for Agri-Photovoltaics in the European Union," Joint Research Centre (JRC), European Commission, Luxembourg, EUR 31482 EN, 2023. doi:10.2760/303437.

[9] Schletter Group, "48 MWp project in Italy," 2025. Available: https://www.schletter-group.com/news/48-mwp-project-in-italy/

[10] Abraham, John. "Despite Trump, American Companies Are Still Investing in Renewable Energy." *The Guardian*, October 11, 2017. https://www.theguardian.com/environment/climate-consensus-97-per-cent/2017/oct/11/despite-trump-american-companies-are-still-investing-in-renewable-energy

[11] International Energy Agency (IEA). *United States – Renewables.* Retrieved from https://www.iea.org/countries/united-states/renewables

[12] International Energy Agency. (2025). *Solar PV*. IEA. https://www.iea.org/energy-system/renewables/solar-pv

[13] AgriVoltaics World Conference. (n.d.). *AgriVoltaics World Conference*. https://www.agrivoltaics-conference.org/

[14] Birchall, M., Hussain, S. N., & Ghosh, A. (2025). *Review of agrivoltaic demonstration site studies with comparable configurations for a UK-based application*. Solar Compass.

[15] European Commission, Joint Research Centre. 2023. "Agrivoltaics Alone Could Surpass EU Photovoltaic 2030 Goals." *EU Science Hub*, October 12. https://joint-research-centre.ec.europa.eu/jrc-news-and-updates/agrivoltaics-alone-could-surpass-eu-photovoltaic-2030-goals-2023-10-12_en

[16] European Climate, Infrastructure and Environment Executive Agency, "Agrivoltaic Canopy: crops and solar panels sharing sunlight," *European Commission*, 27 set. 2023. [Online]. Disponibile: https://cinea.ec.europa.eu/featured-projects/agrivoltaic-canopy-crops-and-solar-panels-sharing-sunlight_en

[17] Ministero dell'Ambiente e della Sicurezza Energetica. (2025). *Investimento 1.1 - Sviluppo agro-voltaico*. https://www.mase.gov.it/portale/web/guest/-/investimento-1.1-sviluppo-agro-voltaico.

[18] Trommsdorff, Max, et al. *Agrivoltaics: Opportunities for Agriculture and the Energy Transition: A Guideline for Germany*. 3rd ed., Fraunhofer Institute for Solar Energy Systems ISE, Feb. 2024

[19] Zahrawi, A. A., & Aly, A. M. (2024). *A review of agrivoltaic systems: Addressing challenges and enhancing sustainability*. *Sustainability, 16*(18), 8271.

[20] Dawnbreaker. (2022, Agosto). *DOE Agrivoltaics: Market Research Study*. U.S. Department of Energy, Solar Energy Technologies Office (SETO)

[21] Sekiyama, T., & Nagashima, A. (2019). Solar Sharing for Both Food and Clean Energy Production: Performance of Agrivoltaic Systems for Corn, A Typical Shade-Intolerant Crop. *Environments*, *6*(6), 65. https://doi.org/10.3390/environments6060065.

[22] Pirtaj Hamedani, H., Gorjian, S., & Ghobadian, B. (2025). *Development of a small aquavoltaic system for co-production of microalgae and electricity*. *AgriVoltaics World Conference 2024: Optimization and Economic Modeling*. https://doi.org/10.52825/agripv.v3i.1341

[23] Ahemd, R., Banna Izaz, M. H., Manik, K. H., Khatun, H., Nath, A., Mim, J. J., & Hossain, N. (2025). Advancements in agrivoltaic systems for enhanced sustainable energy utilization—A review. *Environmental Challenges*, *20*, 101299. https://doi.org/10.1016/j.envc.2025.101299

[24] Harshavardhan Dinesh, Joshua M. Pearce,The potential of agrivoltaic systems,Renewable and Sustainable Energy Reviews,Volume 54, 2016, Pages 299-308.

[25] Hrabanski, M., Verdeil, S., & Ducastel, A. (2024). *Agrivoltaics in France: the multi-level and uncertain regulation of an energy decarbonisation policy*. *Review of Agricultural, Food and Environmental Studies, 105*(1). https://doi.org/10.1007/s41130-024-00204-1

[26] Trommsdorff, M., Vollprecht, J., & Sterzenbach, T. (2025). *Legislation on Agrivoltaics in Germany: Changes and Complements Towards a Comprehensive Legal Framework*. *AgriVoltaics Conference Proceedings*

[27] Trommsdorff, Max, et al. "Dual Land Use for Agriculture and Solar Power Production: Overview and Performance of Agrivoltaic Systems." *IEA-PVPS Task 13 Report T13-29*, 2025, https://doi.org/10.52825/agripv.v3i.2539

[28] Ministero dell'Ambiente e della Sicurezza Energetica (MASE), CREA, ENEA, GSE, & RSE. (2022). *Linee guida in materia di impianti agrivoltaici*. Ministero dell'Ambiente e della Sicurezza Energetica. https://www.mase.gov.it/portale/documents/d/guest/linee_guida_impianti_agrivoltaici-pdf

[29] Ministry of Economy, Trade and Industry (METI). (2025, 30 luglio). *Renewable Energy in Japan*. https://www.meti.go.jp/english/policy/energy_environment/renewable/index.html

[30] National Energy Administration of China & China Photovoltaic Industry Association. (2024). *China Agrivoltaic Development Report 2024: Integrating Renewable Energy and Agricultural Productivity*. Beijing: China PVIA Publications.

[31] Zainali, S., Ma Lu, S., Fernández-Solas, Á., Cruz-Escabias, A., Fernández, E. F., Khalil Zidane, T. E., Honningdalsnesd, E. H., Nygård, M. M., Leloux, J., Berwind, M., Trommsdorff, M., Amaducci, S., Gorjian, S., & Campana, P. E. (2025). Modelling, simulation, and optimisation of agrivoltaic systems: a comprehensive review. *Applied Energy*, 386, 125558.

[32] Jung, D., Schönberger, F., & Spera, F. (2024). *Effects of Agrivoltaics on the Microclimate in Horticulture: Enhancing Resilience of Agriculture in Semi-Arid Zones*. Pubblicato in *AgriVoltaics World Conference 2023*. https://doi.org/10.52825/agripv.v2i.1033

[33] Gomez-Casanovas, N., Mwebaze, P., Khanna, M., et al. (2023). *Knowns, uncertainties, and challenges in agrivoltaics to sustainably intensify energy and food production*. Cell Reports Physical Science, *4*, 101518.

[34] Di Sabatino, M., Randle-Boggis, R. J., Ravi Kumar, R. R., Malhi, H., Lobaccaro, G., Bonesmo, H., Sharma, A., Völler, S., & Stokkan, G. (2025). Agrivoltaics in Norway: Microclimate Modelling and Grass Yields from the Highest Latitude Agrivoltaics System. *AgriVoltaics World Conference 2024 Proceedings*.

[35] Li, Y., Armstrong, A., Simmons, C., Krasner, N. Z., & Hernandez, R. R. (2025). *Ecological impacts of single-axis photovoltaic solar energy with periodic mowing on microclimate and vegetation*. Frontiers in Sustainability, *6*:1497256.

[36] A. Glick *et al.*, "Influence of flow direction and turbulence intensity on heat transfer of utility-scale photovoltaic solar farms," *Solar Energy*, vol. 207, pp. 173-182, 2020

[37] Kannenberg, S. A., Sturchio, M. A., Venturas, M. D., & Knapp, A. K. (2023). Grassland carbon-water cycling is minimally impacted by a photovoltaic array. *Communications Earth & Environment*, 4(1).

[38] Keck, Aries C. 2021. "Evapotranspiration: Watching Over Water Use." *NASA*, August 19, 2021. https://www.nasa.gov/missions/landsat/evapotranspiration-watching-over-water-use/

[39] Stull, R. B. (2009). *An introduction to boundary layer meteorology*. Springer.

[40] Holton, J. R., & Hakim, G. J. (2013). *An introduction to dynamic meteorology*. Elsevier, 2012.

[41] J. Opolka, "CFD Modelling of Vertical Agrivoltaic Systems: Assessing Wind and Radiation Impacts on Agricultural Environments in Scania," Master Thesis, LTH, Lund University, Sweden, June 16, 2025

[42] Suárez, J. L., Cadenas, D., Rubio, H., & Ouro, P. (2022). Vortex Shedding Dynamics Behind a Single Solar PV Panel Over a Range of Tilt Angles in Uniform Flow. *Fluids, 7*(10), 322.

[43] Dartevelle, J. (2024). *Modélisation numérique d'écoulement et de transport au sein de centrales agrivoltaïques d'inter-rang*. Gembloux Agro-Bio Tech (GxABT), LIÈGE université

[44] Bruhwyler, R., Brunet, P., Dabadie, G., Drahi, E., Souquet, P., Chapon, J., Boukouya, A., Delahaye, B., & Jennet, C. (2024). Could Windbreak Effect Significantly Decrease Evapotranspiration in Vertical Agrivoltaics? *AgriVoltaics World Conference 2022*.

[45] Kaimal, J. C., e J. J. Finnigan. *Atmospheric Boundary Layer Flows: Their Structure and Measurement*. Oxford: Oxford University Press, 1994.

[46] D. A. Staton and A. Cavagnino, "Convection Heat Transfer and Flow Calculations Suitable for Electric Machines Thermal Models," *IEEE Trans. Ind. Electron.*, vol. 55, no. 10, pp. 3509–3516, Oct. 2008.

[47] Thornthwaite, C. W. (1948). An Approach toward a Rational Classification of Climate. *Geographical Review*, *38*(1), 55–94. https://doi.org/10.2307/210739

[48] Vidali, C., Marro, M., Gostiaux, L., Houssin, D., Vyazmina, E., & Salizzoni, P. (2025). Wind-tunnel experiment of heavy gas and passive scalar emission in a turbulent boundary layer. *Boundary-Layer Meteorology*, *191*(18). https://doi.org/10.1007/s10546-025-00909-w

[49] R. G. Allen, L. S. Pereira, D. Raes, and M. Smith, *Crop Evapotranspiration: Guidelines for Computing Crop Water Requirements*. Rome, Italy: FAO, FAO Irrigation and Drainage Paper No. 56, c. 1998.

[50] Y. A. Çengel, Termodinamica e trasmissione del calore, a cura di E. Cirillo, 1a ed. Milano: McGraw-Hill Libri Italia, 1998.

[51] Glick, A., Ali, N., Bossuyt, J., Calaf, M., & Cal, R. B. (2020). Utility-scale solar PV performance enhancements through system-level modifications. *Scientific Reports*, *10*, 10505.

[52] Glick, A., Smith, S. E., Ali, N., Bossuyt, J., Recktenwald, G., Calaf, M., & Cal, R. B. (2020). Influence of flow direction and turbulence intensity on heat transfer of utility-scale photovoltaic solar farms. *Solar Energy*, *207*, 173–182.

[53] Glick, A., Ali, N., Bossuyt, J., Recktenwald, G., Calaf, M., & Cal, R. B. (2020). Infinite photovoltaic solar arrays: Considering flux of momentum and heat transfer. *Renewable Energy*, *156*, 791–803.

[54] Smith, S. E., Viggiano, B., Ali, N., Silverman, T. J., Obligado, M., Calaf, M., & Cal, R. B. (2022). Increased panel height enhances cooling for photovoltaic solar farms. *Applied Energy*, *325*, 119819.

[55] Warsido, W. P., Bitsuamlak, G. T., Barata, J., & Chowdhury, A. G. (2014). Influence of spacing parameters on the wind loading of solar array. *Journal of Fluids and Structures*, *48*, 295–315.

[56] Ma, W., Zhang, W., Zhang, X., Chen, W., & Tan, Q. (2023). Experimental investigations on the wind load interference effects of single-axis solar tracker arrays. *Renewable Energy*, *202*, 566–580.

[57] Xu, A., Ma, W., Yuan, H., & Lu, L. (2024). The effects of row spacing and ground clearance on the wind load of photovoltaic (PV) arrays. *Renewable Energy*, *220*, 119627.

[58] Browne, M. T. L., Taylor, Z. J., Li, S., & Gamble, S. (2020). A wind load design method for ground-mounted multi-row solar arrays based on a compilation of wind tunnel experiments. *Journal of Wind Engineering & Industrial Aerodynamics*, *205*, 104294.

[59] Strobel, K., & Banks, D. (2014). Effects of vortex shedding in arrays of long inclined flat plates and ramifications for ground-mounted photovoltaic arrays. *Journal of Wind Engineering and Industrial Aerodynamics*, *133*, 146–149.

[60] Shademan, M., Barron, R. M., Balachandar, R., & Hangan, H. (2014). Numerical simulation of wind loading on ground-mounted solar panels at different flow configurations. *Canadian Journal of Civil Engineering*, *41*(8), 728–738.

[61] E. D. Obasaju and A. G. Robins, "Simulation of pollution dispersion using small scale physical models - An assessment of scaling options," BMT Fluid Mechanics Ltd. and University of Surrey, UK, Tech. Rep., 1996

[62] W. H. Snyder, *Guideline for Fluid Modeling of Atmospheric Diffusion*, Research Triangle Park, NC: Environmental Protection Agency, Office of Air Quality Planning and Standards, 1981.

[63] N. Ali and I. Y. Hussain, "Two-dimensional natural convection heat transfer from a heated plate immersed in a thermally stratified medium: Numerical and experimental study," *Solar Energy*, vol. 136, pp. 244-258, Oct. 2016.